UNIVERSITÀ DEGLI STUDI DI SALERNO

Dipartimento di Ingegneria dell'Informazione ed Elettrica e Matematica Applicata

UNIVERSITÀ DEGLI STUDI DI TRIESTE

Department of Engineering and Architecture

PHD IN PHOTOVOLTAICS

Curriculum A: Solar cells technologies and lifecycle

DOTTORATO NAZIONALE "PHOTOVOLTAICS"

Multi-Scale Enhancement of Photovoltaic Performance; Nanophotonic Spectral Conversion and Intelligent Thermal Prediction

PhD Supervisor:

Prof. Vanni Lughi

Candidate Name:

Maoz Maoz

Co-Supervisor:

Prof. Amir Al Ahmad

Programme Coordinator:

Prof. Giovanni Spagnuolo

XXXVIII Cycle

2022 - 2025

Multi-Scale Enhancement of Photovoltaic Performance; Nanophotonic Spectral Conversion and Intelligent Thermal Prediction

Dedications….

To my beloved daughter, ***YASHFA KHAN,*** *whose presence gives new meaning to my journey and inspires me to work for a brighter future.*

To my dear mother, whose prayers, sacrifices, love, and unwavering support have been the foundation of my strength.

And to my late father, whose dreams for my success continue to guide me. Although he is no longer physically present, his love, values, and hopes remain with me in every achievement.

This thesis is dedicated to them with deepest love, gratitude, and respect.

Abstract

This thesis targets two unresolved performance bottlenecks in photovoltaics: the inefficient utilization of high-energy photons in crystalline silicon solar cells, and the difficulty of accurately predicting temperature-driven performance under real operating conditions. Although crystalline silicon remains the dominant photovoltaic technology, its response to ultraviolet and blue photons is limited by shallow absorption depth, front-surface recombination, parasitic absorption, and rapid thermalization losses. At the system level, photovoltaic performance is further constrained by module temperature, which directly affects voltage, efficiency, operating stability, and long-term degradation. Within this context, the thesis investigates both photon-level and system-level routes for improvement through three connected studies: $CsPbBr_3$ quantum-dot luminescent down-shifting coatings for silicon photovoltaics, plasmon-assisted enhancement of quantum-dot emission, and sequence-based prediction of photovoltaic module temperature. The central novelty of the thesis lies in bridging nanoscale optical engineering with predictive thermal intelligence within one coherent framework for photovoltaic enhancement.

The first part of the thesis develops a planar luminescent down-shifting architecture based on ligand-assisted reprecipitation synthesized $CsPbBr_3$ quantum dots, APTES-mediated surface treatment, and PMMA film integration for crystalline silicon mini-modules. This work addresses the practical gap between the excellent optical properties of perovskite quantum dots and their stable implementation in a device-relevant coating geometry. The results show that APTES-mediated treatment improves photoluminescence behaviour and recombination characteristics, while the PMMA-integrated coating produces measurable enhancement in current density and power conversion efficiency. These findings demonstrate the feasibility of surface-engineered perovskite quantum-dot coatings as external spectral-management layers for silicon photovoltaics, while also highlighting the need for further durability studies and more complete mechanistic separation of luminescent conversion from other front-optical effects.

The second part examines plasmon-assisted photoluminescence enhancement in CdSe/CdS core-shell quantum-dot films coupled with Au nanoparticles deposited by magnetron sputtering. The problem addressed here is the lack of a controlled and reproducible strategy for tuning plasmon-exciton coupling in hybrid quantum-dot-metal systems. The novelty of this work lies in using sputter-deposited Au nanoparticles together with a PMMA spacer layer to systematically study the relationship between nanoparticle morphology, separation distance, and emission response. The results show that spacer thickness is the critical parameter, with an intermediate separation of about 25 nm providing the most favourable balance between photoluminescence enhancement and

quenching. This establishes a more controlled nanophotonic route for improving the radiative performance of colloidal quantum-dot films relevant to photovoltaic light management.

The third part develops a high-resolution thermal forecasting framework for photovoltaic modules using long short-term memory networks. This work addresses the limitations of conventional physics-based and non-sequential machine-learning models in capturing thermal inertia, temporal dependence, and nonlinear environmental interactions under outdoor conditions. The proposed LSTM model achieved strong predictive performance on real-world data, with MAE of 0.621 °C, RMSE of 0.863 °C, and R^2 of 0.998, outperforming benchmark physics-based models. Uncertainty quantification through Monte Carlo dropout and interpretability analysis using SHAP further showed that the framework is both accurate and physically meaningful. Overall, the thesis demonstrates that photovoltaic improvement can be pursued through complementary advances in spectral management, plasmonic control of quantum-dot emission, and intelligent thermal prediction, thereby contributing a multi-scale strategy for more efficient and better understood photovoltaic systems.

Keywords: Photovoltaics; crystalline silicon solar cells; spectral mismatch; luminescent down-shifting; $CsPbBr_3$ quantum dots; surface passivation; plasmonic enhancement; gold nanoparticles; CdSe/CdS core-shell quantum dots; photoluminescence enhancement; photovoltaic module temperature; machine learning; long short-term memory networks; uncertainty quantification; SHAP explainability; thermal prediction

Abstract in Italian

Questa tesi affronta due criticità ancora aperte nel miglioramento delle prestazioni fotovoltaiche: l'utilizzo inefficiente dei fotoni ad alta energia nelle celle solari in silicio cristallino e la difficoltà di prevedere con accuratezza gli effetti della temperatura sulle prestazioni dei moduli fotovoltaici in condizioni operative reali. Sebbene il silicio cristallino rappresenti ancora la tecnologia dominante nel settore fotovoltaico, la sua risposta ai fotoni ultravioletti e blu è limitata dalla ridotta profondità di assorbimento, dalla ricombinazione alla superficie frontale, dall'assorbimento parassita e dalle rapide perdite per termalizzazione. A livello di sistema, le prestazioni fotovoltaiche sono ulteriormente condizionate dalla temperatura del modulo, che influenza direttamente la tensione, l'efficienza, la stabilità operativa e la degradazione a lungo termine.

In questo contesto, la tesi studia strategie di miglioramento sia a livello fotonico sia a livello di sistema attraverso tre studi collegati: rivestimenti luminescenti down-shifting basati su quantum dots di $CsPbBr_3$ per fotovoltaico in silicio, incremento dell'emissione di quantum dots assistito da plasmoni, e previsione sequenziale della temperatura dei moduli fotovoltaici. La novità centrale della tesi consiste nel collegare l'ingegneria ottica su scala nanometrica con l'intelligenza predittiva termica all'interno di un quadro coerente per il miglioramento delle prestazioni fotovoltaiche.

La prima parte della tesi sviluppa un'architettura planare di luminescent down-shifting basata su quantum dots di $CsPbBr_3$ sintetizzati mediante ligand-assisted reprecipitation, trattamento superficiale mediato da APTES e integrazione in film di PMMA per mini-moduli in silicio cristallino. Questo lavoro affronta il divario pratico tra le eccellenti proprietà ottiche dei quantum dots perovskitici e la loro implementazione stabile in una geometria di rivestimento rilevante per il dispositivo. I risultati mostrano che il trattamento mediato da APTES migliora il comportamento di fotoluminescenza e le caratteristiche di ricombinazione, mentre il rivestimento integrato in PMMA produce un miglioramento misurabile della densità di corrente e dell'efficienza di conversione di potenza. Questi risultati dimostrano la fattibilità di rivestimenti esterni per la gestione spettrale basati su quantum dots perovskitici ingegnerizzati superficialmente per il fotovoltaico in silicio, evidenziando al tempo stesso la necessità di ulteriori studi di durabilità e di una separazione meccanicistica più completa tra conversione luminescente e altri effetti ottici frontali.

La seconda parte esamina l'incremento della fotoluminescenza assistito da plasmoni in film di quantum dots core-shell CdSe/CdS accoppiati con nanoparticelle d'oro depositate mediante sputtering magnetronico. Il problema affrontato riguarda la mancanza di una strategia controllata e riproducibile per regolare l'accoppiamento plasmone-eccitone in sistemi ibridi quantum dot-metallo. La novità di questo lavoro consiste nell'utilizzo di nanoparticelle d'oro depositate mediante sputtering insieme a uno strato spaziatore di PMMA per studiare sistematicamente la relazione tra morfologia

delle nanoparticelle, distanza di separazione e risposta emissiva. I risultati mostrano che lo spessore dello spaziatore è il parametro critico, con una separazione intermedia di circa 25 nm che fornisce il miglior equilibrio tra incremento della fotoluminescenza e quenching. Questo studio stabilisce quindi una via nanofotonica più controllata per migliorare le prestazioni radiative di film colloidali di quantum dots, rilevanti per la gestione della luce nel fotovoltaico.

La terza parte sviluppa un framework ad alta risoluzione per la previsione termica dei moduli fotovoltaici mediante reti long short-term memory. Questo lavoro affronta i limiti dei modelli convenzionali basati sulla fisica e dei modelli di machine learning non sequenziali nel catturare inerzia termica, dipendenze temporali e interazioni ambientali non lineari in condizioni outdoor. Il modello LSTM proposto ha raggiunto elevate prestazioni predittive su dati reali, con MAE pari a 0,621 °C, RMSE pari a 0,863 °C e R^2 pari a 0,998, superando i modelli fisici di riferimento. La quantificazione dell'incertezza mediante Monte Carlo dropout e l'analisi di interpretabilità tramite SHAP hanno inoltre dimostrato che il framework è non solo accurato, ma anche fisicamente significativo.

Nel complesso, la tesi dimostra che il miglioramento del fotovoltaico può essere perseguito attraverso progressi complementari nella gestione spettrale, nel controllo plasmonico dell'emissione dei quantum dots e nella previsione termica intelligente. In questo modo, il lavoro contribuisce a una strategia multi-scala per sistemi fotovoltaici più efficienti e meglio compresi.

Acknowledgements

My deepest appreciation goes to my supervisor, **Prof. Vanni Lughi**, for his guidance and support throughout this PhD journey. His scientific advice, constructive feedback, and continuous motivation have been essential to the development and completion of this thesis.

I would also like to acknowledge my co-supervisor, **Dr. Amir Al Ahmad**, for his academic support, supervision, and guidance during my period abroad. This experience helped me advance my scientific skills and added an important international dimension to my PhD work.

I also thank the **University of Salerno** and the **National PhD Programme in Photovoltaics** for allowing me to undertake this doctoral research, and I sincerely acknowledge the Programme Coordinator, **Prof. Giovanni Spagnuolo**, for his academic coordination and support. Most of my experimental work was carried out in the laboratories of the **School of Nanotechnology**, and I am also grateful to the **Department of Engineering and Architecture, University of Trieste (UNITS)**. The research environment, facilities, and academic support provided by the department significantly contributed to this work.

I would also like to acknowledge the **Interdisciplinary Research Centre for Sustainable Energy Systems (IRC-SES)** and the **Chemistry Department at King Fahd University of Petroleum and Minerals**, where I carried out part of my research during my period abroad. I am grateful for their hospitality, research facilities, and scientific exchange, which contributed meaningfully to my doctoral journey.

I would also like to thank **FlySolar Tech** for the collaboration established during my PhD, as well as for its financial support. I am particularly grateful to **Luigi Marres** and **Piero Gabrez** for their constructive interactions, practical insights, and industrial perspective on this work.

I would also like to sincerely thank **Dr. Hamid Ali Khan, Dr. Syed Abdul Basit, Dr. Wahid Ullah, Rashid Ashraf, Hammad Khaliq, Rizwan Ullah, Salik Awan, and Dr. Haris** for their encouragement and support at different stages of my PhD work. Their assistance, discussions, and moral support are deeply appreciated.

Finally, I would like to thank my wife, **Aisha Khan**, for her love, patience, understanding, and emotional support throughout this journey. She has been a source of strength during both the most challenging and the most rewarding moments of my PhD.

Table of Contents

Contents

Abstract 4

Abstract in Italian 6

Acknowledgements 8

Table of Contents 9

List of Figures 15

List of Tables 17

List of Abbreviations 18

List of Papers 20

Executive Summary 21

Chapter.1 Introduction 23

1.1. Global Energy Context and Photovoltaics 23

1.2. Limits of Conventional Silicon Solar Cells 24

1.3. Spectral Mismatch and Ultraviolet Losses 25

1.4. Role of Nanomaterials in Photovoltaics 26

1.5. Quantum Dots for Spectral Conversion 26

1.6. Plasmonics for Optical Enhancement 27

1.7. Luminescent Down-Shifting (LDS) 27

1.8. Machine Learning in Photovoltaics 27

1.9. Research Motivation 29

1.10. Research Gap and Thesis Objectives 30

1.10.1 Research gap 30

1.10.2 Thesis objectives 32

1.11. Thesis Organization 32

Chapter.2 Literature Review 34

2.1. Fundamentals of photovoltaic devices 34

2.1.1 Silicon solar cell structures and where modern performance comes from 34

2.1.2 Efficiency parameters and device metrics used throughout this review 34
2.1.3 Temperature dependence of PV output 35
2.2. Optical losses and spectral mismatch in silicon solar cells 35
2.2.1 UV loss mechanisms specific to silicon modules and front stacks 36
2.2.2 Surface recombination and short-wavelength response 36
2.2.3 Parasitic absorption in non-active layers 36
2.2.4 Spectral response mismatch and spectral variability 36
2.3. Luminescent down-shifting for photovoltaics 37
2.3.1 Principle of LDS and why it targets silicon's weak spectral regions 37
2.3.2 Key requirements for effective LDS materials 37
2.3.3 Stokes shift, self-absorption, and why "spectral separation" dominates LDS scaling 37
2.3.4 PLQY as the governing efficiency metric, and why it is fragile in films 38
2.3.5 Host matrices and integration strategies 38
2.3.6 Prior work on LDS for silicon solar cells, from laboratory cells to module-like stacks 38
2.4. Quantum dots as spectral converters 39
2.4.1 QDs as attractive LDS emitters 39
2.4.2 Cadmium-based QDs (CdSe, CdTe, and core–shell variants) 39
2.4.3 Carbon dots 39
2.4.4 Lanthanides, including quantum cutting as a spectral conversion route 39
2.4.5 Perovskite QDs 40
2.5. $CsPbBr_3$ and related perovskite quantum dots 42
2.5.1 Structure and optical properties 42
2.5.2 Synthesis routes 42
2.5.3 Ligand chemistry as the stability and integration bottleneck 42
2.5.4 Instability issues relevant to PV deployment 42
2.5.5 Encapsulation strategies 43
2.5.6 Prior PV applications 43
2.6. Surface chemistry, polymer integration, and plasmonics in quantum dot layers 43

2.6.1 Role of ligands and interfacial control 43
2.6.2 APTES and organosilicon chemistry in perovskite nanocrystal protection 44
2.6.3 Silica-rich interfaces and shell thickness effects 44
2.6.4 PMMA as a host matrix 44
2.7. Plasmon-assisted photoluminescence enhancement for QDs and implications for LDS layers 45
2.8. PV module thermal behaviour and physics-based operating-temperature models 47
2.9. Data-driven thermal modelling and forecasting for PV modules 49
2.10. Integrated synthesis and research gaps 53
Chapter.3 Polymer-Integrated Surface-Passivated $CsPbBr_3$ Quantum Dots for Luminescent Down-Shifting in Crystalline Silicon Solar Cells 57
3.1. Background 57
3.2. Problem Statement 59
3.3. Experimental section 60
3.3.1 Materials used 60
3.3.2 Synthesis of $CsPbBr_3$ quantum dots 60
3.3.3 Synthesis of $CsPbBr_3@SiO_2$ quantum dots using 3-APTES 60
3.3.4 Preparation of PMMA-embedded LDS solutions 61
3.4. QDs concentration calculation section 62
3.4.1 Deposition of LDS layers on c-Si mini modules 64
3.5. Results and Discussion 64
3.5.1 Structural and phase analysis by XRD 64
3.6. TEM and size distribution, morphology 66
3.7. XPS chemical surface analysis 68
3.8. Absorption and PL 69
3.9. TRPL 70
3.10. Performance analysis as LDS layer on Si Solar cell. 74
3.10.1 PCE and Jsc of bare QDs and Si treated QDs 74
3.10.2 IV Curves 76

3.10.3 Relative PCE % Performance 77
3.11. Conclusion 78
Chapter.4 Plasmon-Assisted Photoluminescence Enhancement in CdSe/CdS Quantum-Dot Films Coupled with Gold Nanoparticles 80
4.1. Background 80
4.2. Problem Statement 81
4.3. Experimental Procedure 82
4.3.1 Materials 82
4.3.2 Synthesis of CdSe Quantum Dots 82
4.3.3 Growth of CdSe/CdS Core-Shell Quantum Dots 83
4.4. Fabrication of AuNPs/QD Coupling Structures 83
4.5. Optical Characterization 85
4.6. Results and Discussion 86
4.6.1 Morphology and size distribution of sputter-deposited Au nanoparticles 86
4.6.2 Optical characteristics of AuNPs and CdSe/CdS quantum dots 88
4.6.3 Preprocessing and normalization of PL spectra 91
4.6.4 Spacer-thickness-dependent PL response 94
4.7. Conclusion 97
Chapter.5 High-Resolution Prediction of Photovoltaic Module Temperature Using Sequence-Based Machine Learning 98
5.1. Background 98
5.2. Problem Statement 100
5.3. Methodology Section 100
5.3.1 Data Source and Collection 100
5.3.2 Key Attributes of the Dataset: 100
5.3.3 Feature Engineering 101
5.4. Model Architecture and Training 102
5.4.1 Physics based models 102
5.5. Data-driven models 104

5.5.1 Artificial Neural Networks (ANN) 104
5.5.2 Long Short-Term Memory Networks (LSTM) 104
5.5.3 Subset Scenario Testing 106
5.5.4 Model Evaluation 106
5.5.5 Uncertainty Estimation and Explainability 106
5.6. Results 107
5.6.1 Physics-based models 107
5.6.2 Data Driven Models 109
5.6.3 ANN-Based Models 109
5.6.4 LSTM-Based Models 110
5.6.5 Discussion and Scientific Insights 110
5.7. Comparison of overall best model 111
5.7.1 Overfitting and Generalization Assessment 112
5.7.2 R^2 Behaviour and Stability 113
5.7.3 Generalization vs. Complexity Trade-off 114
5.7.4 Average Time-Series Cross-Validation Performance 114
5.7.5 Monte Carlo Dropout Uncertainty Analysis 115
5.7.6 SHAP analysis 116
5.7.7 Feature Correlation Analysis 118
5.7.8 Condition-Specific Performance Evaluation 120
5.8. Conclusion 122
Chapter.6 Integrated Discussion of Optical and Thermal Strategies for Photovoltaic Performance Enhancement 124
6.1. Overview of the integrated research framework 124
6.2. Relationship between the optical studies 125
6.3. Interpretation of the LDS findings in a broader scientific context 125
6.4. Interpretation of the plasmonic photoluminescence findings in a broader scientific context 126
6.5. Comparison of the two optical strategies 127

6.6. Integration of the thermal prediction study with the optical performance study 128
6.7. Cross-cutting scientific contributions of the thesis 129
6.8. Main limitations across the thesis 130
6.9. Future directions emerging from the integrated work 130
6.10. Final integrated perspective 131
Chapter.7 Conclusion 133
7.1. Overall conclusion 133
7.2. Main scientific contributions 134
7.3. Scientific limitations and careful scope of the conclusions 134
7.4. Final perspective 135
References 136

List of Figures

Figure 1-1: Schematic illustration of the global growth of solar photovoltaics and the increasing challenge of achieving further efficiency gains in mature photovoltaic technologies 23
Figure 1-2: Schematic representation of advanced crystalline silicon solar cell architectures, PERC, TOPCon, and heterojunction, highlighting their layer structures and efficiency potential above 25% 24
Figure 1-3: Comparison of the AM1.5G solar spectrum and the usable spectral range of a crystalline silicon solar cell 25
Figure 3-1: X-ray diffraction (XRD) patterns of bare $CsPbBr_3$ and APTES-modified $CsPbBr_3@SiO_2$ quantum dots 65
Figure 3-2: Transmission electron microscopy (TEM) images and size distribution of $CsPbBr_3$ and $CsPbBr_3@SiO_2$ quantum dots. 66
Figure 3-3: Particle Size Distribution of Bare-$CsPbBr_3$ and $CsPbBr_3@SiO_2$ 67
Figure 3-4: X-ray photoelectron spectroscopy (XPS) survey spectra of $CsPbBr_3$ and $CsPbBr_3@SiO_2$ quantum dots. 68
Figure 3-5: UV–visible absorption and photoluminescence spectra of bare $CsPbBr_3$ and $CsPbBr_3@SiO_2$ quantum dots. 69
Figure 3-6: Time-resolved photoluminescence (TRPL) decay of $CsPbBr_3$ and $CsPbBr_3@SiO_2$ quantum dots in solution 72
Figure 3-7: Time-resolved photoluminescence (TRPL) decay of $CsPbBr_3$ and $CsPbBr_3@SiO_2$ quantum dots in thin film 73
Figure 3-8: Photovoltaic performance of crystalline silicon mini-modules coated with PMMA-based LDS layers containing bare $CsPbBr_3$ or $CsPbBr_3@SiO_2$ quantum dots. 75
Figure 3-9: Current density–voltage (J–V) characteristics of silicon mini-modules coated with PMMA-based LDS layers containing $CsPbBr_3$ and $CsPbBr_3@SiO_2$ quantum dots. 76
Figure 3-10: Relative enhancement in power conversion efficiency for different LDS formulations. 77
Figure 4-1: Hybrid plasmonic structure consisting of a CdSe/CdS quantum-dot PMMA layer, a PMMA spacer, and Au nanoparticles deposited on a glass substrate 84
Figure 4-2: Variation of PMMA spacer-layer thickness as a function of PMMA concentration 85
Figure 4-3:SEM image of a bare glass substrate coated with carbon 86
Figure 4-4: SEM image of Au Nanoparticles on a glass substrate 87
Figure 4-5: Size Distribution plot of AuNPs 88
Figure 4-6: Absorption Spectra of Au Nanoparticles 89

Figure 4-7: Absorption and Photoluminescence spectra of CdSe core 89
Figure 4-8: Absorption and Photoluminescence spectra of CdSe-CdS core-shell 90
Figure 4-9: Data Fitting of QDs Photoluminescence 91
Figure 4-10: Raw PL data of QDs smoothed with Savitzky-Golay filter 92
Figure 4-11: Excitation and Photoluminescence Peak of Plasmonic Coupling Structure 93
Figure 4-12: Box plots of PL data of five different samples prepared 94
Figure 5-1: LSTM Architecture for PV module temperature forecasting 105
Figure 5-2: Comparison of Physics-based models' performance evaluation metrics 108
Figure 5-3: Comparison of data-driven predictive models' performance evaluation metrics 109
Figure 5-4: Comparison of best performing data driven and physics based models 111
Figure 5-5: Evaluation metrics comparison on train and test data 112
Figure 5-6: Coefficent of Determination of different data driven models 113
Figure 5-7: Time series cross-validation performance 114
Figure 5-8: Monte Carlo Prediction on High uncertaininty data points 116
Figure 5-9: SHAP feature Impact bar chart for all the input features 117
Figure 5-10: Temporal SHAP Heatmap for overall features 118
Figure 5-11: Pearson coorealtion matrix among different features 119
Figure 5-12: LSTM_seq_50 best performing model prediction for Peak solar hours 120
Figure 5-13: LSTM_seq_50 best performing model prediction for high windy conditions 121
Figure 5-14: LSTM_seq_50 best performing model prediction for summer temperatures 121

List of Tables

Table 2-1: Comparative assessment of major luminescent down-shifting material classes 40
Table 2-2: Plasmonic design parameters for luminescent down-shifting layer design 46
Table 2-3: Representative studies on photovoltaic module temperature prediction 51
Table 3-1: Sample Matrix for LDS formulations 61
Table 3-2: Calculated concentrations of $CsPbBr_3$ quantum dots in LDS solutions prepared with different stock solution volumes 63
Table 3-3: Lifetime decay calculations from TRPL fitting data of the solution phase (where f denotes fractional contribution) 71
Table 3-4: Lifetime decay calculations from TRPL fitting data of the thin film 71
Table 4-1: Area under the Curves and Its Ratio 93
Table 5-1: Input features including physical, temporal and derived statistical features 101
Table 5-2: Physics-based model for determining PV module temperature 103

List of Abbreviations

Abbreviation	Full Form
AM1.5G	Air Mass 1.5 Global
ANN	Artificial Neural Network
APTES	3-Aminopropyltriethoxysilane
AuNPs	Gold Nanoparticles
CdS	Cadmium Sulphide
CdSe	Cadmium Selenide
$CsPbBr_3$	Cesium Lead Bromide
$CsPbBr_3@SiO_2$	Silica-treated or silica-passivated cesium lead bromide quantum dots
c-Si	Crystalline Silicon
EQE	External Quantum Efficiency
EVA	Ethylene Vinyl Acetate
FF	Fill Factor
FRET	Förster Resonance Energy Transfer
IBC	Interdigitated Back Contact
IR	Infrared
IV	Current Voltage
Jsc	Short-Circuit Current Density
J-V	Current Density Voltage
LARP	Ligand-Assisted Reprecipitation
LDS	Luminescent Down-Shifting
LSC	Luminescent Solar Concentrator
LSPR	Localized Surface Plasmon Resonance
LSTM	Long Short-Term Memory
MAE	Mean Absolute Error
MEF	Metal-Enhanced Fluorescence
ML	Machine Learning
NIR	Near-Infrared
NSET	Nanometal Surface Energy Transfer
OA	Oleic Acid
OAm	Oleylamine
PCE	Power Conversion Efficiency
PERC	Passivated Emitter and Rear Cell
PL	Photoluminescence
PLQY	Photoluminescence Quantum Yield
PMMA	Poly(methyl methacrylate)
PV	Photovoltaic
Si-QD	Silane-treated Quantum Dots
QDs	Quantum Dots
R^2	Coefficient of Determination

Abbreviation	Full Form
RMSE	Root Mean Square Error
SAPM	Sandia Array Performance Model
SEM	Scanning Electron Microscopy
SHAP	SHapley Additive exPlanations
SHJ	Silicon Heterojunction
Si	Silicon
SiO_2	Silicon Dioxide
STC	Standard Test Conditions
TCO	Transparent Conductive Oxide
TEM	Transmission Electron Microscopy
TEOS	Tetraethyl Orthosilicate
TOPCon	Tunnel Oxide Passivated Contact
TRPL	Time-Resolved Photoluminescence
UV	Ultraviolet
UV-Vis	Ultraviolet-Visible Spectroscopy
Voc	Open-Circuit Voltage
XPS	X-ray Photoelectron Spectroscopy
XRD	X-ray Diffraction

List of Papers

[1] M. Maoz, Z. Abbas, S. A. B. Shah, and V. Lughi, “Recent Advances in Flexible Solar Cells; Materials, Fabrication, and Commercialization,” *Sustainability 2025, Vol. 17, Page 1820*, vol. 17, no. 5, p. 1820, Feb. 2025, doi: 10.3390/SU17051820.

[2] M. Maoz, S. A. B. Shah, and V. Lughi, “Photoluminescence Enhancement in CdSe/CdS Quantum Dot Colloidal Films Induced by Gold Nanoparticles (AuNPs),” *ACS Omega*, vol. 10, no. 37, pp. 42472–42479, Sep. 2025, doi: 10.1021/ACSOMEGA.5C03718.

[3] Surface-Passivated $CsPbBr_3$ Quantum-Dot Coatings for Luminescent Down-Shifting in Crystalline Silicon Photovoltaics {to be submitted: Progress in Photovoltaics}

[4] Data-Driven Modelling of Photovoltaic Module Temperature Using Long Short-Term Memory Networks {to be submitted: Applied Energy}

[5] Conference presentation on “Scenario-Based Thermal and Optical Analysis of CdSe/CdS Quantum Dot Downshifting Layers for Enhanced Efficiency in Silicon Photovoltaic Modules Using ANSYS” in "Green Energy in MENA Region Conference: Solar Energy, Green Hydrogen and AgroTec"

Executive Summary

This thesis addresses two persistent and practically significant challenges in photovoltaic research, the limited utilization of high-energy photons in crystalline silicon solar cells and the difficulty of accurately predicting module temperature under real operating conditions. Although crystalline silicon remains the dominant photovoltaic technology, its conversion of ultraviolet and short-wavelength visible photons is constrained by shallow absorption depth, front-surface recombination, parasitic absorption, and thermalization losses. In parallel, photovoltaic module temperature plays a central role in determining voltage output, conversion efficiency, operating stability, and long-term degradation. Within this context, the thesis develops a multi-scale framework for photovoltaic improvement by combining nanoscale optical engineering with data-driven thermal prediction.

The work is organized around three complementary research studies. The first study investigates luminescent down-shifting coatings based on $CsPbBr_3$ quantum dots for crystalline silicon mini-modules. A planar coating architecture was developed by combining ligand-assisted reprecipitation synthesis, APTES-mediated surface treatment, and PMMA film integration. This approach was designed to improve the optical utilization of high-energy photons without modifying the underlying silicon junction. The results indicate that surface treatment improves photoluminescence behavior and recombination characteristics, while the polymer-integrated coating leads to measurable enhancement in current density and power conversion efficiency. These findings support the feasibility of surface-engineered perovskite quantum-dot coatings as external spectral-management layers for silicon photovoltaics, while also indicating the need for continued work on long-term stability and deeper mechanistic separation of luminescent and non-luminescent optical effects.

The second study examines plasmon-assisted photoluminescence enhancement in CdSe/CdS core-shell quantum-dot films coupled with gold nanoparticles deposited by magnetron sputtering. The purpose of this work was to establish a more controlled and reproducible nanophotonic platform for tuning plasmon-exciton interaction. Particular attention was given to the influence of nanoparticle morphology and the thickness of the dielectric spacer layer. The results show that spacer thickness is the dominant design parameter, with an intermediate PMMA separation producing the most favorable balance between photoluminescence enhancement and quenching. This study provides useful design insight into how localized plasmonic effects can be tuned in hybrid quantum-dot-metal systems and how such control may support broader light-management strategies relevant to photovoltaics.

The third study develops a high-resolution framework for photovoltaic module temperature prediction using long short-term memory networks. In contrast to conventional steady-state or static empirical approaches, the proposed model is able to capture thermal inertia, sequential dependence, and nonlinear interactions among environmental variables under outdoor conditions. The model

achieved strong predictive performance and was further strengthened through uncertainty quantification using Monte Carlo dropout and interpretability analysis using SHAP. This part of the thesis demonstrates that sequence-based machine learning can provide both accurate and physically meaningful thermal prediction, with relevance to photovoltaic performance analysis, operational intelligence, and future digital-twin development.

Taken together, the thesis demonstrates that photovoltaic improvement can be pursued through complementary advances at different scales. The optical studies focus on photon management through luminescent down-shifting and plasmon-assisted emission control, while the thermal study addresses predictive understanding of photovoltaic behavior under real environmental conditions. Although these research strands are methodologically distinct, they are united by the broader objective of improving photovoltaic efficiency, reliability, and scientific understanding. The thesis therefore contributes a coherent multi-scale perspective in which materials engineering, optical control, and predictive modeling are treated as mutually relevant pathways toward more efficient and better understood photovoltaic systems.

In summary, the thesis makes three principal contributions. First, it demonstrates a practical route for integrating surface-engineered perovskite quantum dots into polymer-based coatings for crystalline silicon photovoltaics. Second, it establishes controlled spacer-dependent plasmonic design principles for the enhancement of quantum-dot emission. Third, it presents an interpretable and uncertainty-aware LSTM-based framework for photovoltaic module temperature prediction. Collectively, these contributions position the thesis as a scientifically grounded and application-oriented study that links photon-level enhancement with system-level predictive intelligence in photovoltaic research.

Chapter.1 Introduction

1.1. Global Energy Context and Photovoltaics

The decarbonization of global energy systems represents one of the most pressing scientific and technological challenges of the twenty-first century. Photovoltaics (PV) has emerged as a cornerstone technology in this transition, driven by continuous reductions in cost, scalability of deployment, and compatibility with distributed generation systems. Recent global energy assessments indicate that solar PV is now the fastest-growing electricity generation technology, surpassing all other sources in annual capacity additions[1], [2].

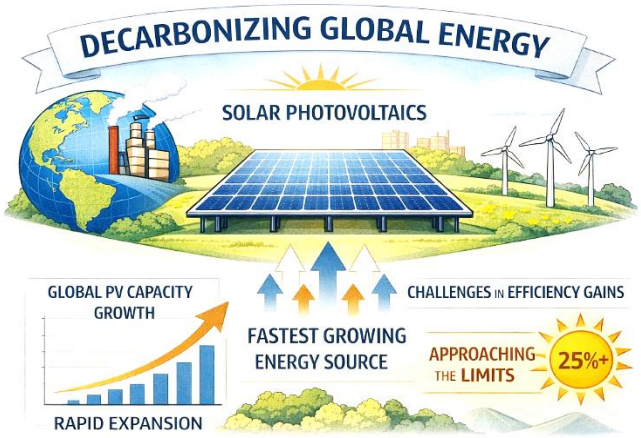

Figure 1-1: Schematic illustration of the global growth of solar photovoltaics and the increasing challenge of achieving further efficiency gains in mature photovoltaic technologies

Despite this rapid growth, the technological trajectory of PV is entering a phase where incremental efficiency gains are increasingly difficult to achieve. Crystalline silicon (c-Si) solar cells, which dominate the market, have benefited from decades of optimization, resulting in highly mature device architectures such as PERC, TOPCon, and heterojunction systems. These architectures, as shown in Figure 1.2, have achieved efficiencies exceeding 26%, approaching the practical limits imposed by fundamental thermodynamic constraints [3], [4].

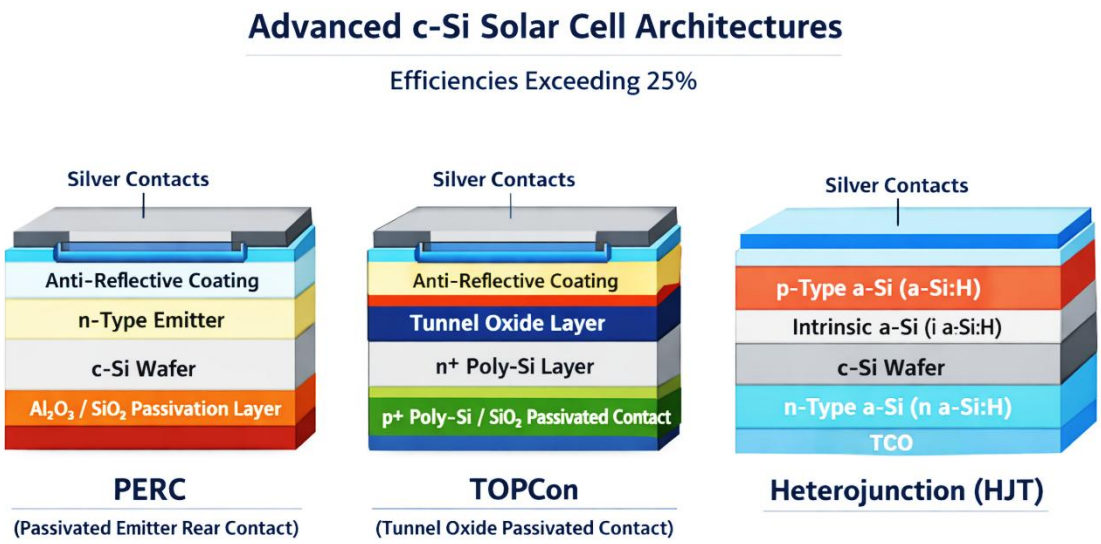

Figure 1-2: Schematic representation of advanced crystalline silicon solar cell architectures, PERC, TOPCon, and heterojunction, highlighting their layer structures and efficiency potential above 25%

This saturation of conventional improvement pathways has led to a paradigm shift in recent research. Rather than focusing exclusively on charge transport and junction engineering, increasing attention is being directed toward photon management strategies, where the incident solar spectrum itself is modified or manipulated prior to absorption. This shift reflects a broader recognition that future efficiency improvements in silicon photovoltaics are unlikely to arise solely from electronic optimization, but rather from integrated optical and material innovations [5].

1.2. Limits of Conventional Silicon Solar Cells

The performance limits of silicon solar cells are fundamentally governed by the detailed balance framework, which defines the maximum achievable efficiency based on radiative recombination and spectral absorption constraints. Within this framework, three dominant loss mechanisms persist: thermalization losses, transmission losses, and recombination losses [6], [7].

Thermalization losses arise from the rapid relaxation of charge carriers generated by high-energy photons, leading to dissipation of excess energy as heat. Transmission losses occur due to the inability of silicon to absorb photons with energies below its bandgap. While these two loss channels are intrinsic to the material, recombination losses, particularly at surfaces and interfaces, are strongly influenced by device design and processing conditions. Recent studies highlight that, even in advanced architectures with optimized passivation, recombination losses remain non-negligible, especially for carriers generated near the front surface [8]. This limitation is exacerbated by the indirect bandgap of silicon, which inherently leads to weak absorption near the band edge and inefficient utilization of high-energy photons [9].

Importantly, conventional strategies such as improved passivation, light trapping, and contact engineering primarily address recombination and absorption efficiency within the device but do not fundamentally resolve spectral mismatch. As a result, these approaches are approaching diminishing returns, reinforcing the need for external spectral engineering strategies that operate independently of the internal device physics [10].

1.3. Spectral Mismatch and Ultraviolet Losses

Spectral mismatch between the solar irradiance spectrum and the absorption characteristics of silicon remains a critical bottleneck in photovoltaic performance, as shown in Figure 1.3. In particular, ultraviolet (UV) photons ($\lambda < 400$ nm) present a dual challenge: while they carry high energy, their contribution to electrical output is disproportionately low due to rapid thermalization and enhanced recombination as shown in the figure.

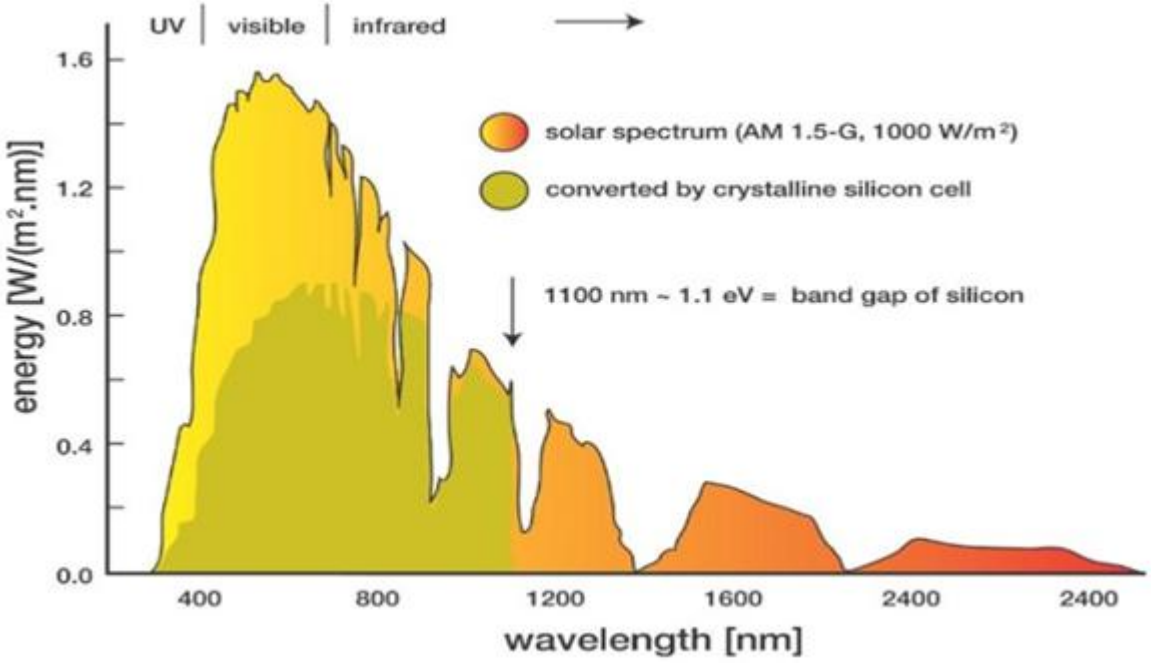

Figure 1-3: Comparison of the AM1.5G solar spectrum and the usable spectral range of a crystalline silicon solar cell [Reproduced from [11]]

Recent investigations demonstrate that UV photons are absorbed within an extremely shallow region, typically within the first tens of nanometers of the silicon surface [12]. This region is highly susceptible to recombination due to surface states and imperfect passivation, leading to significant carrier losses. Consequently, the external quantum efficiency in the UV region remains substantially lower than in the visible spectrum. Moreover, system-level considerations further exacerbate these losses. Encapsulation materials, including glass and polymeric layers, introduce additional attenuation through absorption and scattering of UV photons [13]. This implies that a non-negligible portion of the solar spectrum is either lost before reaching the active layer or inefficiently converted once absorbed.

While these limitations are well recognized, conventional mitigation strategies remain insufficient. This has led to renewed interest in spectral conversion techniques, particularly luminescent down-shifting (LDS), which aim to convert high-energy photons into wavelengths more effectively utilized by silicon. However, the practical implementation of such approaches remains constrained by material inefficiencies and integration challenges [13], [14], [15].

1.4. Role of Nanomaterials in Photovoltaics

Nanomaterials offer a fundamentally different approach to addressing spectral mismatch by enabling direct manipulation of light–matter interactions at subwavelength scales. Their size-dependent optical properties and strong electromagnetic confinement effects provide unique opportunities for enhancing absorption, emission, and energy transfer processes [16].

In recent years, there has been a clear shift toward integrating nanomaterials as externally applied functional layers, rather than embedding them within the active junction. This strategy minimizes disruption to charge transport while enabling independent optimization of optical properties [17]. However, despite extensive research, a critical limitation persists. Many nanophotonic approaches demonstrated at the laboratory scale rely on complex fabrication techniques, lack reproducibility, or are incompatible with large-area processing. As highlighted in recent studies, scalability remains one of the primary barriers to the practical implementation of nanomaterial-based spectral management strategies [18].

This tension between optical performance and manufacturability underscores the need for approaches that combine nanoscale precision with scalable fabrication techniques [19], a challenge that remains insufficiently addressed in current literature.

1.5. Quantum Dots for Spectral Conversion

Quantum dots (QDs) have emerged as one of the most promising classes of nanomaterials for spectral conversion due to their tunable optical properties and high photoluminescence efficiency. Their ability to absorb high-energy photons and re-emit at longer wavelengths makes them particularly suitable for luminescent down-shifting applications [20]. Core–shell systems such as CdSe/CdS provide a robust platform for achieving high photoluminescence quantum yield through effective passivation of surface states. These systems have been extensively studied for their well-defined excitonic behavior and stability [21]. However, their practical implementation in photovoltaic systems is often limited by toxicity concerns and challenges in large-scale processing [22].

In contrast, all-inorganic perovskite quantum dots, particularly $CsPbBr_3$, have demonstrated exceptional optical properties, including high PLQY and strong absorption in the UV region. Recent advances in surface passivation and ligand engineering have significantly improved their stability,

addressing one of the key limitations of perovskite materials [23], [24]. Nevertheless, critical challenges remain. Reabsorption losses in dense QD films, instability under prolonged illumination, and sensitivity to environmental conditions continue to limit their performance. These issues highlight the need for integrated material and structural optimization strategies, rather than isolated improvements in QD synthesis [25].

1.6. Plasmonics for Optical Enhancement

Plasmonic nanostructures provide an alternative pathway for enhancing light–matter interactions through localized surface plasmon resonance (LSPR), which enables strong electromagnetic field confinement at the nanoscale [26]. When coupled with quantum emitters, plasmonic nanoparticles can enhance excitation rates and modify radiative decay processes, leading to increased emission intensity. However, the interaction between plasmonic structures and quantum dots is inherently complex, involving competing mechanisms such as near-field enhancement, Purcell enhancement, and nonradiative energy transfer [27]. Recent work emphasizes that the spatial separation between quantum dots and plasmonic nanoparticles is the key parameter governing this interaction, with optimal performance achieved only within a narrow distance window. However, achieving such precise control in scalable systems remains a significant challenge [28], [29].

1.7. Luminescent Down-Shifting (LDS)

Luminescent down-shifting represents a conceptually simple yet practically challenging approach to spectral management. By converting high-energy photons into wavelengths better matched to the absorption spectrum of silicon, LDS can reduce thermalization losses and improve device performance [29]. While quantum dots are ideal candidates for LDS due to their tunable emission and high absorption coefficients, their integration into functional devices introduces additional complexities. In particular, achieving high PLQY in solid-state films, minimizing reabsorption losses, and ensuring long-term stability remain unresolved challenges[30]. Furthermore, many reported LDS systems demonstrate optical improvements under controlled conditions but fail to translate these gains into significant device-level efficiency enhancements. This discrepancy highlights a critical gap between material-level performance and system-level impact, which remains insufficiently addressed in current research [15].

1.8. Machine Learning in Photovoltaics

Machine learning (ML) has become an increasingly important tool in photovoltaic research because PV systems operate under nonlinear, time-dependent, and weather-driven conditions that are difficult to describe fully using simplified analytical or empirical models. As PV deployment expands across distributed and utility-scale systems, ML is being used not only for power forecasting, but also for

fault diagnosis, degradation analysis, predictive maintenance, and thermal modeling. In this sense, ML in photovoltaics is not merely a computational alternative, but a practical framework for extracting predictive insight from complex operating data [31].

Among these applications, forecasting is the most established, since accurate prediction of PV behavior is essential for grid integration, dispatch planning, storage management, and operational reliability [32]. Because PV output depends on coupled variations in irradiance, air temperature, wind speed, seasonality, and local environmental effects, conventional statistical approaches often struggle to represent the resulting nonlinear dynamics. ML and deep learning methods have therefore been increasingly adopted to improve short-term and day-ahead prediction accuracy, particularly under rapidly changing weather conditions. At the same time, diagnostic applications of ML have become important for identifying faults, anomalies, and degradation signatures that may not be distinguishable from normal environmental variability using rule-based approaches alone [33].

Within this broader landscape, thermal prediction has emerged as a particularly significant area because module temperature directly influences voltage, efficiency, operating stability, and long-term degradation. Unlike power alone, temperature also acts as an intermediate state variable that links environmental forcing to device response. However, PV module temperature is governed by a coupled interaction among irradiance, ambient temperature, wind speed, infrared exchange, mounting configuration, and thermal inertia, making high-resolution prediction difficult under realistic field conditions [34]. This is especially relevant to the present thesis, where photovoltaic performance is considered not only from the perspective of optical enhancement, but also from the viewpoint of predictive system behavior under real operating environments.

A critical reason why ML is effective for this problem is that photovoltaic data are inherently temporal. Variables such as irradiance, module temperature, and power evolve as sequences, and their present values depend not only on current weather conditions but also on recent system history. This is particularly important for temperature prediction, where delayed thermal response and cumulative heat exchange effects are physically meaningful. Sequence-learning methods, especially long short-term memory (LSTM) networks, are therefore well suited to PV applications because they can capture temporal dependencies, lag effects, and nonlinear interactions more effectively than static regressors [35].

For this thesis, ML is not introduced as an isolated computational topic, but as the system-level extension of the broader research framework. Just as nanoscale optical engineering is used to improve photon utilization through quantum dots, plasmonics, and luminescent down-shifting, data-driven modeling is used to improve predictive understanding of PV behavior under dynamic environmental conditions. In this way, the thesis connects material-level and optical-level enhancement strategies

with intelligent system-level analysis. The machine-learning component, particularly the use of sequence-based thermal prediction, therefore represents the predictive counterpart of the experimental work, extending the thesis from optical and material design toward data-driven interpretation and optimization of photovoltaic performance

1.9. Research Motivation

The motivation for this thesis arises from a convergence of unresolved challenges in silicon photovoltaics at both the device and system levels. Although crystalline silicon remains the dominant photovoltaic technology, it does not utilize the ultraviolet and blue region of the solar spectrum efficiently. High-energy photons are absorbed very close to the front surface, where reflection, parasitic absorption, and surface recombination losses are more pronounced, and any excess photon energy above the bandgap is rapidly dissipated through thermalization. As a result, part of the incident solar resource is not converted as effectively as the visible and near-infrared portion of the spectrum. Recent work on luminescent down-shifting for silicon heterojunction devices, together with a 2025 review of QD-enabled down-shifting and down-conversion, reinforces that short-wavelength spectral mismatch remains a meaningful opportunity for external photon-management strategies in silicon PV [36].

Quantum dots provide a compelling response to this limitation because they can convert high-energy photons into lower-energy photons that are better matched to the spectral response of silicon. Their suitability comes from quantum-confinement-driven tunability, strong absorption in the UV-blue region, and the possibility of engineering emission wavelength, Stokes shift, and photoluminescence efficiency through size, composition, and surface chemistry. In practical terms, this makes QDs attractive as luminescent down-shifting materials that can be integrated as external coatings without redesigning the silicon junction itself. Recent studies on core-shell QD LDS layers and broader reviews of QD-based spectral conversion both show that such materials can regulate UV-region spectral mismatch and improve photovoltaic utilization when optical losses are controlled [37].

A further motivation comes from the fact that QD emission is not fixed solely by the nanocrystal itself, but can be modified by its optical environment. In particular, plasmonic nanostructures supporting localized surface plasmon resonance, LSPR, can generate intense near fields and alter excitation and radiative-decay behavior in nearby emitters. When plasmon resonance is properly aligned with QD absorption or emission, and when the metal-QD spacing is carefully controlled, the result can be stronger photoluminescence and improved optical coupling. Recent reviews of LSPR engineering and plasmon-coupled QD systems emphasize that these enhancements originate from field localization, scattering, and modified excitonic decay pathways, while also noting that poor spectral or spatial matching can lead to quenching instead of enhancement. This makes plasmonic

coupling a rational next step after basic QD spectral conversion, namely, not only converting high-energy photons, but also intensifying the efficiency of the conversion process itself [38].

At the system level, photovoltaic performance is also strongly constrained by thermal conditions. Module temperature affects efficiency directly, mainly through voltage loss, and also influences long-term reliability, degradation, and lifetime. Because operating temperature is governed by irradiance, ambient temperature, wind, mounting conditions, and thermal inertia, it varies dynamically under outdoor conditions and cannot be treated as a simple secondary variable. Recent reviews and forecasting studies show that PV temperature prediction is increasingly recognized as essential for performance assessment, plant management, and lifetime-aware operation. In other words, a photovoltaic system may be optically improved at the material level, but its real-world benefit still depends on how temperature evolves during operation [39].

This leads directly to the final motivation of the thesis, accurate thermal forecasting as an enabler of smart PV operation. Data-driven models can use environmental and operational time-series data to estimate module temperature more accurately than simple static correlations, thereby supporting forecasting, diagnostics, anomaly detection, and more informed control strategies. This is particularly important because PV systems are inherently dynamic, with current behavior shaped by recent irradiance history, thermal buildup, and environmental transients. Recent PV temperature-prediction studies and broader ML reviews show that time-aware and sequence-based learning frameworks are especially valuable for capturing these nonlinear temporal dependencies [35].

Therefore, the motivation of this thesis is not limited to material enhancement alone, but extends to intelligent prediction, where optical management and predictive modeling are treated as complementary routes toward higher-performance and smarter photovoltaic systems. In this context, the three works unified in this thesis address one common objective from complementary directions: first, to recover underutilized high-energy photons in silicon photovoltaics through QD-based luminescent down-shifting, second, to amplify QD optical performance through plasmonic coupling, and third, to improve system-level efficiency awareness and operational intelligence through accurate thermal prediction. Together, these themes form a coherent research pathway linking nanoscale photon management with data-driven photovoltaic intelligence [30].

1.10. Research Gap and Thesis Objectives

1.10.1 Research gap

The research gap addressed in this thesis arises from two complementary, but methodologically distinct, limitations in current photovoltaic research.

The first limitation concerns optical management in silicon photovoltaics. Although crystalline silicon remains the dominant PV technology, it still utilizes ultraviolet and blue photons inefficiently because of front-surface losses, shallow absorption depth, and thermalization. The first paper shows that perovskite quantum dots are promising for luminescent down-shifting, but that a practical gap remained in developing a planar LDS architecture that combines LARP-synthesized $CsPbBr_3$ quantum dots, APTES-based surface passivation, and PMMA integration specifically for crystalline silicon solar cells. Existing studies had mainly relied on EVA matrices, conventional ligand systems, or non-photovoltaic applications, leaving limited work on this particular materials and coating configuration. The same study further indicates that APTES passivation improves photoluminescence efficiency and recombination behavior, while the PMMA-based LDS coating yields measurable current and efficiency enhancement on silicon mini-modules. However, the paper also makes clear that further validation of the LDS mechanism and long-term durability remains necessary.

A related, but separate, optical gap is addressed in the second paper. Quantum dots suitable for down-shifting and light management often remain limited by non-radiative recombination, photoluminescence quenching, and insufficient excitation efficiency. The plasmonic study shows that while Au nanoparticle assisted photoluminescence enhancement is known in the broader literature, the use of magnetron-sputtered Au nanoparticles for controlled enhancement of CdSe/CdS core-shell quantum dot films had not been systematically established. This is important because reproducible plasmonic enhancement depends strongly on nanoparticle morphology and QD-metal spacing. The paper demonstrates that magnetron sputtering offers improved morphological control, and that the spacer layer is a decisive parameter, with maximum enhancement observed at about 25 nm PMMA thickness, whereas shorter separations favor quenching. Thus, the second gap is not direct photovoltaic coating integration, but nanoscale optimization of plasmon-exciton coupling for enhancing the radiative performance of quantum dots relevant to spectral-conversion applications.

The third gap addressed in the thesis belongs to a different research stream, photovoltaic thermal prediction. Unlike the first two papers, which are centered on optical materials and nanophotonics, the third paper focuses on system-level predictive intelligence. It identifies that PV module temperature, despite being a critical determinant of efficiency, voltage behavior, and degradation, is still less studied than power or irradiance forecasting. It also shows that many existing approaches do not explicitly represent temporal thermal inertia and often lack uncertainty quantification and interpretability. The study addresses this by comparing physics-based and machine-learning approaches and showing that sequence-based LSTM models provide superior thermal forecasting accuracy under real-world operating conditions.

Accordingly, the thesis is unified not by one single narrow gap, but by a broader need to improve photovoltaic performance at two levels. The first two studies address photon-level enhancement through quantum-dot based spectral conversion and plasmon-assisted emission control. The third study addresses operational-level enhancement through accurate and interpretable thermal forecasting. Together, they establish a thesis framework that links optical management with predictive intelligence, while preserving the methodological distinction between these two research directions.

1.10.2 Thesis objectives

The overall aim of this thesis is to investigate complementary material-level and system-level strategies for improving photovoltaic performance.

The specific objectives are:

1. To develop and investigate $CsPbBr_3$ quantum-dot based luminescent down-shifting coatings for crystalline silicon solar cells.
2. To examine the effect of APTES-mediated surface passivation and PMMA embedding on the structural, optical, and photovoltaic performance of $CsPbBr_3$ quantum-dot LDS layers.
3. To evaluate the feasibility of planar perovskite QD-based LDS coatings as external spectral-management layers for silicon photovoltaics.
4. To investigate plasmon-assisted photoluminescence enhancement in CdSe/CdS core-shell quantum-dot films using gold nanoparticles.
5. To determine the influence of Au nanoparticle morphology and spacer-layer thickness on the balance between enhancement and quenching in QD-AuNP hybrid structures.
6. To develop accurate predictive models for photovoltaic module temperature under real outdoor operating conditions.
7. To compare physics-based, ANN-based, and sequence-learning models for PV thermal forecasting.
8. To assess the importance of temporal dependence, thermal inertia, uncertainty quantification, and explainability in photovoltaic temperature prediction.
9. To present an integrated thesis perspective in which optical photon-management research and predictive thermal intelligence are treated as complementary routes toward improved photovoltaic performance.

1.11. Thesis Organization

This thesis is organized into seven chapters.

Chapter 1 introduces the background, motivation, research gap, objectives, and scope of the thesis.

Chapter 2 reviews the literature relevant to the thesis. It covers the fundamentals of photovoltaic devices, spectral mismatch, luminescent down-shifting, quantum dots as spectral converters, plasmon-assisted photoluminescence enhancement, and machine-learning approaches for photovoltaic thermal prediction.

Chapter 3 presents the first research study on surface-passivated $CsPbBr_3$ quantum-dot coatings for luminescent down-shifting in crystalline silicon photovoltaics. It describes the synthesis, characterization, and photovoltaic evaluation of the coatings, with emphasis on the role of APTES treatment and PMMA integration.

Chapter 4 presents the second research study on plasmonic enhancement of photoluminescence in CdSe/CdS core-shell quantum-dot films coupled with gold nanoparticles. It examines the influence of nanoparticle morphology and spacer thickness on the balance between enhancement and quenching.

Chapter 5 presents the third research study on data-driven modelling of photovoltaic module temperature using long short-term memory networks. It discusses the dataset, model development, performance evaluation, uncertainty analysis, and interpretability of the proposed framework.

Chapter 6 provides an integrated discussion of the thesis findings by linking the optical and thermal aspects of photovoltaic performance improvement explored in the previous chapters.

Chapter 7 summarizes the main conclusions of the thesis, highlights its key contributions, and outlines recommendations for future research.

This thesis does not claim that the optical and thermal studies are experimentally coupled in one device. Instead, it develops complementary strategies addressing photon utilization and temperature prediction as two major routes for improving PV performance

Chapter.2 Literature Review

This chapter reviews the recent literature relevant to the three research strands developed in the thesis, quantum-dot based luminescent down-shifting for silicon photovoltaics, plasmonically modified quantum-dot emission, and data-driven photovoltaic thermal forecasting. Rather than treating these topics as unrelated subfields, the review is organized around the common question of how photovoltaic performance can be improved through better control of photon utilization and better prediction of field-relevant thermal behaviour.

The review is deliberately selective. Its purpose is not to catalogue all work on quantum dots, plasmonics, or machine learning in photovoltaics, but to identify the specific conceptual and methodological gaps that justify the present study. For that reason, emphasis is placed on device relevance, film-state behaviour, interfacial engineering, stability after integration, and model trustworthiness under outdoor conditions. This framing is consistent with the current direction of the literature, where simple proof-of-concept gains are increasingly considered insufficient unless they are supported by realistic integration, durable operation, or operational interpretability.

2.1. Fundamentals of photovoltaic devices

2.1.1 Silicon solar cell structures and where modern performance comes from

Crystalline silicon remains the dominant PV technology, but the internal device architecture has rapidly evolved in the past seven years, largely to reduce recombination and optical losses at contacts. Industry roadmaps and recent reviews document the mainstream industrial transition from Al-BSF toward PERC, and then toward n-type architectures such as TOPCon and silicon heterojunction (SHJ), with IBC architectures also growing in specific segments [40]. From a device-physics standpoint, the common direction is to decouple “good passivation” from “good conductivity” at contacts via passivating contact concepts (e.g., thin tunnel oxides with doped poly-Si) and heterojunction passivation (e.g., amorphous or nanocrystalline silicon layers). Reviews of crystalline silicon passivation strategies highlight that continued gains in silicon cell efficiency are now constrained by a smaller set of loss channels, particularly those associated with contacts, optical management at the front stack, and parasitic absorption in functional layers [41].

2.1.2 Efficiency parameters and device metrics used throughout this review

For a solar cell under irradiance G and device temperature T, the power conversion efficiency is

$$\eta = \frac{P_{\max}}{P_{\text{in}}} = \frac{V_{\text{mp}} I_{\text{mp}}}{GA} \qquad \text{Eq. 1.1}$$

and is commonly decomposed using

$$P_{\max} = V_{\mathrm{oc}} I_{\mathrm{sc}}\,\mathrm{FF} \qquad \text{Eq. 1.2}$$

where V_{oc} encodes recombination and bandgap-related thermodynamics, I_{sc} scales with absorbed photon flux and collection efficiency, and the fill factor (FF) is strongly shaped by resistive and recombination losses. Recent PV technology reviews and parameter-extraction studies stress that FF is often the most sensitive aggregate indicator of subtle resistive and recombination pathways (for example, contact resistance increases, shunt formation, and transport degradation) [42].

Optical-to-electrical conversion is routinely evaluated using external quantum efficiency (EQE),

$$\mathrm{EQE}(\lambda) = \frac{\text{collected charge carriers}}{\text{incident photons at } \lambda} \qquad \text{Eq. 1.3}$$

and integrals over EQE and the illuminant spectrum predict J_{sc}. Recent methodological work links EQE to spectral mismatch correction, measurement best practice, and uncertainty in both single-junction and tandem devices, which becomes especially important when spectral converters (such as LDS layers) are introduced [43].

2.1.3 Temperature dependence of PV output

Across silicon technologies, a recurring observation is that I_{sc} tends to increase slightly with temperature (bandgap narrowing increases absorption near the band edge), while V_{oc} decreases more strongly due to thermodynamic and recombination-related dependencies, yielding a net efficiency reduction at higher operating temperature. Device-specific studies have quantified temperature coefficients for modern architectures (e.g., TOPCon and SHJ), then analysed how temperature alters contact resistivity, passivation quality, saturation currents, and FF [44].

Recent field and reliability-oriented papers further highlight that temperature interacts with packaging, encapsulant chemistry, humidity exposure, and series resistance evolution, making cell temperature a key driver of both short-term performance loss and long-term degradation risk [45].

2.2. Optical losses and spectral mismatch in silicon solar cells

As crystalline silicon devices approach practical passivation and contact limits, “optical current” becomes a dominant lever: the achievable J_{sc} is increasingly dictated by reflection, shadowing, escape losses, and parasitic absorption in non-absorber layers (TCOs, doped layers, antireflection stacks, and encapsulation materials). Recent detailed analyses of record-efficiency SHJ devices show that layer-by-layer optical loss decomposition is now sufficiently mature to define practical J_{sc} limits and prioritise engineering interventions [46].

2.2.1 UV loss mechanisms specific to silicon modules and front stacks

Three classes of UV-related losses recur in recent literature.

First, UV photons may be reflected at the air, glass, and coating interfaces, particularly when front optics are not optimised for 300 to 400 nm. Second, UV can be absorbed in the glass and in encapsulation polymers (or in UV-stabiliser additives), preventing UV photons from reaching the cell and altering the "available spectrum" that the cell experiences. Third, UV can accelerate discolouration and other photochemical degradation in encapsulation materials, which subsequently increases longer-wavelength absorption and scattering losses [47].

The practical implication is that UV losses are not only a spectral mismatch issue, they also potentially become a reliability accelerator via packaging optics and chemistry, so UV management strategies must be evaluated at the laminate and module level, not just at the bare-cell level [48].

2.2.2 Surface recombination and short-wavelength response

In crystalline silicon, high-energy photons are absorbed very near the surface, so carrier collection for UV and blue photons is disproportionately sensitive to surface and emitter recombination. Contemporary passivation reviews emphasise that reducing surface recombination velocity and controlling interface defect density remain central to extracting short-wavelength current, especially as wafer thicknesses decrease and as front stacks become more complex (for example, in SHJ or passivating-contact designs) [41].

2.2.3 Parasitic absorption in non-active layers

Beyond reflection, parasitic absorption in transparent conductive oxides and near-surface layers increasingly sets a ceiling on silicon current generation. Recent work has tackled this from two complementary directions: (i) materials and process engineering for more transparent TCOs and functional layers, and (ii) optical modelling frameworks that represent parasitic absorption in a way that is both physically meaningful and usable for device optimisation [16].

This is directly connected to spectral conversion concepts, because LDS layers are often motivated by the desire to "recover" photons that are otherwise lost in those parasitically absorbing front layers [17].

2.2.4 Spectral response mismatch and spectral variability

Even with standard reporting under AM1.5 reference spectra, real-world spectra vary with aerosol loading, air mass, humidity, cloud microphysics, and angular distribution of diffuse light. Recent studies quantify how spectral mismatch becomes a hidden uncertainty source in PV energy yield and

power forecasting, and they also motivate spectral correction methods that use measured or modelled spectra together with device EQE [18].

At the metrology level, there is renewed emphasis on spectral mismatch correction during device characterisation, including the use of EQE-informed correction methods and modern test systems (LED-based solar simulators) that can more tightly control spectral shape [49].

2.3. Luminescent down-shifting for photovoltaics

2.3.1 Principle of LDS and why it targets silicon's weak spectral regions

Luminescent down-shifting places an optically active layer above (or within) the PV front stack that absorbs higher-energy photons (commonly UV) and re-emits lower-energy photons (commonly visible) that the underlying solar cell converts more efficiently. Recent spectral modification reviews frame LDS as a pragmatic complement to tandem architectures: it leaves the silicon device electrically unchanged but aims to increase usable photon flux in spectral regions limited by surface recombination or parasitic absorption [50]. LDS layers can also contribute through secondary optical effects such as scattering and refractive-index matching, which can reduce reflection or redistribute optical path lengths. This coupling between luminescent conversion and classical light management is repeatedly observed as a confounding but exploitable feature in experimental studies [51].

2.3.2 Key requirements for effective LDS materials

The recent literature converges on a multi-constraint design space:

Absorption must be strong in the target high-energy region but weak in the region where the PV already performs well, to avoid stealing useful photons. The emission spectrum must align with high EQE of silicon, which typically favours the visible and near-infrared. The layer must have high photoluminescence quantum yield (PLQY) under the relevant excitation conditions, maintain optical clarity to avoid scattering losses that do not help trapping, and remain stable against UV, heat, oxygen, and moisture over module lifetimes. Finally, processing and materials compatibility with encapsulants, cover glass, and silicon cell metallisation are required to avoid new reliability problems [52].

2.3.3 Stokes shift, self-absorption, and why "spectral separation" dominates LDS scaling

A large Stokes shift, meaning significant separation between absorption and emission spectra, is a core requirement because self-absorption reintroduces loss via repeated absorption–emission cycles, nonradiative decay, and waveguiding or escape processes that do not return photons to the cell. This is particularly visible in luminescent solar concentrator (LSC) and LDS modelling papers, which show that reabsorption can become the dominant limiter when scaling thickness or lateral dimensions

[53]. A striking recent route to minimising reabsorption is quantum cutting (downconversion) architectures in which emission is pushed into the near-infrared (often via Yb^{3+}), where intrinsic reabsorption can be negligible and PLQY can exceed 100% in photon number under appropriate conditions [53].

2.3.4 PLQY as the governing efficiency metric, and why it is fragile in films

In laboratory demonstrations, near-unity PLQY can be achieved for some nanocrystal systems in solution, yet PLQY in solid films often drops due to aggregation, surface trap formation, ligand loss, or energy transfer to quenching centres. Recent stability-focused literature for perovskite nanocrystals shows that mitigating this "solution-to-solid penalty" generally requires either robust surface chemistry (stronger binding, cross-linking, or defect passivation), or physical encapsulation that prevents environmental exposure while controlling inter-particle spacing [54].

2.3.5 Host matrices and integration strategies

Polymer matrices (e.g., EVA in modules, PMMA in coatings) are widely used because they are processable and can act as diffusion barriers, but the polymer environment also sets refractive index, mechanical behaviour under thermal cycling, and sometimes chemical compatibility with QD ligands. In parallel, silica-rich encapsulation layers and mesoporous silica supports are actively researched because they can strongly improve moisture and thermal stability, though shell thickness and optical scattering must be controlled to preserve high effective PLQY and transparency [55].

2.3.6 Prior work on LDS for silicon solar cells, from laboratory cells to module-like stacks

Several recent demonstrations illustrate both promise and constraints:

Silicon QDs have been applied as LDS coatings on polycrystalline silicon cells, with reported improvements attributed to combined UV conversion and reflectance reduction, and with encapsulation sometimes improving effect stability [56]. Carbon dots have been anchored on anti-reflection silica layers to form a "top-side" LDS approach that avoids the UV filtering imposed by glass and some encapsulants, underscoring the importance of layer placement in the stack [57].

$CsPbBr_3$ perovskite QDs have been integrated as down-shifting and antireflection hybrid structures on multicrystalline silicon, providing a representative perovskite-QD LDS pathway directly compatible with silicon-cell formats [51]. More module-relevant integration trends include EVA-based perovskite QD composite films for silicon solar cells, where interface engineering and stability under heat become dominant design constraints rather than initial PLQY alone [58].

2.4. Quantum dots as spectral converters

2.4.1 QDs as attractive LDS emitters

Quantum dots offer tunable absorption and emission through quantum confinement, and many classes can be engineered for high PLQY, narrow emission linewidth, and broad UV to visible absorption, making them natural candidates for LDS and spectral matching. Recent reviews on QD-based LDS layers emphasise that the same tunability that benefits displays can be leveraged to match silicon's spectral response, with the caveat that stability, toxicity, and film processing become decisive in PV contexts [15].

2.4.2 Cadmium-based QDs (CdSe, CdTe, and core–shell variants)

Cd-based QDs are photophysically mature: they can achieve high PLQY and controllable emission, and they have been applied as conversion and light-management layers in silicon-linked demonstrations. Recent experimental work on CdSe QD hybrid coatings for monocrystalline silicon reports efficiency improvements via a combined downconversion or down-shifting mechanism plus antireflection effects, illustrating how QDs can couple luminescence and optical-texture phenomena [59]. Nevertheless, cadmium toxicity and regulation, and the need for robust encapsulation to avoid environmental release, remain structural weaknesses in PV module contexts, where lifecycle and compliance constraints are stricter than in controlled optoelectronic environments. Recent literature increasingly treats these constraints as decisive when comparing cadmium-based QDs to less toxic alternatives [60].

2.4.3 Carbon dots

Carbon dots and carbon quantum dots are attractive due to lower elemental toxicity, low-cost precursors, and strong chemical tunability. Recent reviews summarize their photophysics, heteroatom doping strategies, and applications in optoelectronics and photovoltaics, while experimental papers report downconversion coatings designed to enhance silicon solar cell performance [61]. A recurring limitation is that many carbon dot systems exhibit broad emission and lower intrinsic absorption cross-sections compared to semiconductor QDs, and they may require careful optical design to avoid parasitic absorption or colour losses. The literature increasingly addresses this through matrix engineering, doping, and interface control to stabilise PL and improve quantum yields in films [62].

2.4.4 Lanthanides, including quantum cutting as a spectral conversion route

Lanthanide-based converters can exploit narrow f–f transitions and, in some architectures, quantum cutting can yield more than one emitted photon per absorbed photon in photon-number terms. Recent studies and reviews focus on Yb^{3+}-related downconversion and the conditions required to sustain high

effective PLQY, as well as integration pathways into solar technologies [63].The key disadvantages remain limited absorption cross-section in many lanthanide systems and the need for sensitisation (for example, using perovskite hosts or other absorbers), which can reintroduce stability and surface-trap constraints [64].

2.4.5 Perovskite QDs

Lead halide perovskite QDs combine strong absorption with narrow, tunable emission and potentially high PLQY. They have been used both as active photovoltaic absorbers (in perovskite QD solar cells) and as spectral converters or protective photonic layers. Recent reviews position them as a leading LDS class, but also highlight that instability under moisture, heat, light, and polar solvents remains a primary barrier to deployment [65]. Across these classes, the recent literature suggests a "tri-constraint" for PV spectral converters: (i) optical merit (high PLQY, strong UV absorption, controlled Stokes shift), (ii) environmental and thermal stability in realistic stacks, and (iii) benignity and manufacturability at scale. Cd-based QDs often lead in optical maturity but lose on toxicity, carbon dots lead on benignity but may lag in spectral precision and PLQY without optimisation, lanthanides can offer quantum cutting but struggle with absorption and integration, while perovskite QDs lead in spectral power but lag in stability and lead management [15]. Table 2.1 gives a comparative assessment of LDS for crystalline silicon.

Table 2-1: Comparative assessment of major luminescent down-shifting material classes

Material class	**Typical strengths for LDS**	**Typical weaknesses for LDS**	**Stability outlook**	**PV readiness outlook**
Perovskite QDs ($CsPbX_3$)	Very high PLQY possible, narrow emission, adjustable visible colour, strong absorption [52].	Environmental instability without robust shells or encapsulation, lead toxicity concerns, ligand loss in solids [53].	Rapidly improving via silica and hierarchical shells, but module-relevant ageing remains the decisive test [53].	High potential if stability and lead-handling barriers are addressed, especially for laminated films [54].
Cd-based core or	High and well-understood PLQY, strong UV	Cadmium toxicity and compliance barrier, potential for parasitic	Good photostability when	Technically mature, but deployment

core–shell QDs	to visible absorption, mature shell passivation, predictable film formation [49].	absorption if absorption tails extend into visible [49].	well-passivated and embedded, but long-term UV exposure and polymer ageing still matter [49].	constrained by regulation and end-of-life considerations [48].
Carbon dots	Low toxicity, chemical stability, potentially low-cost synthesis and scalable processing [50].	Broad, sometimes excitation-dependent emission, variable PLQY and batch reproducibility, self-absorption risk in thicker films.	Generally strong chemical stability, but optical properties depend sensitively on surface chemistry and host [50].	Promising for benign coatings, but spectral precision and PLQY control remain limiting [48].
Lanthanide phosphors and complexes	Exceptional photostability and chemical robustness, narrow emission lines for chosen dopants [55].	Weak absorption bands, often requires thick layers or sensitisation, scattering can dominate optical effects [56].	Strong, often superior to QDs and dyes, suitable for long-life module environments if optical coupling is solved [57].	Potentially high if absorption and coupling constraints are addressed, most credible in robust thick-film or composite [56]. Click or tap here to enter text.

No single LDS material class dominates across PLQY, stability, and PV deployability. Perovskite QDs lead on optical potential but demand aggressive stability engineering, Cd-based QDs provide a technically mature benchmark clouded by toxicity limits, carbon dots offer benign stability with less spectral precision, and lanthanides excel in durability but must overcome absorption limitations. This ranking motivates a thesis strategy that treats interface engineering and encapsulation as core scientific problems, not secondary packaging steps [66].

2.5. $CsPbBr_3$ and related perovskite quantum dots

2.5.1 Structure and optical properties

$CsPbBr_3$ belongs to the ABX_3 lead halide perovskite family and is frequently discussed in the context of bright green emission, narrow emission linewidth, and strong visible absorption. Recent experimental reports using ligand-assisted reprecipitation (LARP) and thin-film fabrication document characteristic absorption features and emission in the green region, with optical constants relevant to film optics [67]. Perovskite nanocrystals are often described as "defect tolerant" relative to many conventional semiconductors, yet the LDS application is particularly sensitive to surface trap states because nonradiative loss directly reduces PLQY and therefore net photon recycling into the silicon cell. Stability and surface-passivation reviews stress that "defect tolerance" does not remove the need for rigorous surface engineering in films and during environmental exposure [54].

2.5.2 Synthesis routes

In the recent literature, $CsPbBr_3$ QDs are commonly produced via hot-injection routes and via room-temperature LARP, with the latter being appealing for scalable processing. Comparative discussions emphasize that the synthesis method affects size dispersion, ligand binding, defect density, and therefore emission linewidth and PLQY, which then conditions suitability for LDS layers [67]. Mechanochemical and solid-state routes, including growth in mesoporous silica confinement, have also been explored to enhance robustness by physically restricting growth and shielding the QDs from the environment, often yielding improved thermal and water stability [68].

2.5.3 Ligand chemistry as the stability and integration bottleneck

Standard $CsPbBr_3$ QD syntheses often rely on oleic acid and oleylamine ligands, but a recurrent message in recent ligand studies is that these ligands can bind dynamically and their desorption or rearrangement during purification and film formation can introduce traps, aggregation, and instability. Within the past five years, zwitterionic ligands and cross-linkable ligand systems have been studied to stabilise nanocrystals while controlling charge transfer and film formation [69] . The optoelectronic implication is not trivial: ligand choice changes trap-mediated recombination, photoluminescence lifetime, and electron transfer rates to adjacent layers. This matters for LDS because it influences both emission efficiency and the probability that energy is lost nonradiatively at the QD surface or transferred into quenching substrates [70].

2.5.4 Instability issues relevant to PV deployment

The dominant instabilities for $CsPbBr_3$ QDs include sensitivity to moisture and oxygen, degradation under light (including UV), and thermal instability that drives aggregation or phase changes. Recent

module-oriented LDS work explicitly highlights thermal aggregation and film deterioration at elevated temperatures as central constraints, because silicon modules routinely operate well above 25 °C in the field [71].

2.5.5 Encapsulation strategies

Encapsulation and coating strategies have diversified substantially in the last seven years.

Silica-based encapsulation, including APTES-derived silica shells, TEOS-based sol–gel coatings, mesoporous silica confinement, and multi-layer inorganic shells, is repeatedly reported to improve water and thermal stability while aiming to preserve high PLQY [55].

Polymer embedding, especially into PMMA or EVA, provides processable, optically transparent host matrices while offering a barrier to oxygen and moisture diffusion, although trade-offs arise in mechanical durability, thermal expansion mismatch, and possible photochemical ageing of the polymer [72]. Recent studies demonstrates multi-coating strategies, including hierarchical shells combining inorganic and polymeric layers, designed to lock nanocrystal surfaces and inhibit both degradation and toxic metal leakage, a key pivot toward technology translation [73].

2.5.6 Prior PV applications

$CsPbBr_3$ and related perovskite QDs appear in PV research in two distinct roles.

As photovoltaic absorbers, perovskite QD solar cells (often $CsPbI_3$-based but within the perovskite QD family) have demonstrated high-performance and flexible architectures, illustrating that QD films can be engineered for charge transport and mechanical endurance [65]. As spectral converters on silicon or related devices, recent work has demonstrated $CsPbBr_3$ QD LDS layers with combined down-shifting and antireflection effects on silicon, as well as EVA-compatible composite films that deliver absolute efficiency improvements and partial retention of gains after heating, which is crucial for module-relevant viability [51].

2.6. Surface chemistry, polymer integration, and plasmonics in quantum dot layers

2.6.1 Role of ligands and interfacial control

For LDS layers, ligands play multiple roles simultaneously: they passivate surface traps (supporting high PLQY), control inter-particle spacing (reducing aggregation quenching), and mediate compatibility with host matrices or coating chemistries. The recent literature shows that ligand design is also inseparable from charge and energy transfer at interfaces, even when the layer is not intended to conduct charge, because unwanted electronic coupling to adjacent oxides or metals can introduce nonradiative channels [70].

2.6.2 APTES and organosilicon chemistry in perovskite nanocrystal protection

APTES has two valuable properties for perovskite nanocrystal composites: it can interact strongly with perovskite surfaces and it can hydrolyse and condense to form silica-like networks, enabling silica-rich protective interfaces. Recent mini-reviews describe APTES-based core–shell strategies, and mechanistic studies show that APTES can suppress trap-mediated recombination compared with conventional ligands, which is directly relevant to improving PLQY in films [55]. At the same time, recent electron-transfer studies demonstrate a key trade-off: cross-linked or strongly insulating ligands can suppress unwanted charge extraction (beneficial for avoiding quenching), but may also alter electronic coupling in ways that matter for adjacent functional layers (for example, when QDs interact with oxides). This underscores that "passivation for PL" and "compatibility with device stacks" are linked but not identical optimisation targets [70].

2.6.3 Silica-rich interfaces and shell thickness effects

Silica shells are widely used because they provide chemical and moisture resistance and can slow ligand loss, but shell thickness introduces optical and physical penalties if uncontrolled, including increased scattering, reduced absorption, or inhibited energy transfer into the cell. Recent reviews explicitly discuss the importance of shell thickness control and single-particle-level coatings to maintain nanocrystal optical quality while improving stability [55].

2.6.4 PMMA as a host matrix

PMMA remains a canonical host polymer for luminescent nanocrystals because it is optically transparent in much of the visible, processable via solution routes, and can stabilise nanocrystals by limiting diffusion and aggregation. Recent studies show that PMMA embedding can yield high PLQY composites and improved environmental stability for $CsPbBr_3$ systems, including thin-film case studies where PMMA passivation improves photophysical properties [72]. However, the stability–performance trade-off emerges in multiple ways: polymer matrices can yellow under UV exposure, can relax or creep under thermal cycling, and can impose diffusion pathways for oxygen and water depending on formulation and laminate architecture. Module-oriented encapsulant research, including efforts toward high-UV-transparency polymers, therefore becomes directly relevant to LDS layer design if the LDS layer is intended for front-of-module implementation [47]. Therefore, PMMA is not treated only as a passive host in this thesis, but as a key integration medium that affects optical stability, film formation, and device-level LDS performance

2.7. Plasmon-assisted photoluminescence enhancement for QDs and implications for LDS layers

Plasmonic nanostructures offer a route to enhance QD photoluminescence without changing the QD chemistry directly, by modifying the electromagnetic environment. In the metal-enhanced fluorescence (MEF) framework, enhancement can arise from increased excitation rates (local field enhancement) and from increased radiative decay rates (Purcell-type modification), while quenching arises from additional non-radiative loss channels such as energy transfer to the metal. The classic MEF literature articulates this as a distance-dependent competition, with strong quenching at very small separations and enhancement at intermediate distances [67].

Two distance-dependence models frequently appear. Förster-type resonant energy transfer (FRET) provides one conceptual baseline, while nanometal surface energy transfer (NSET) frameworks have been proposed to better describe energy transfer to metal nanoparticle layers and the associated quenching behaviour. Experimental studies of QDs near gold nanoparticle planes show that quenching and lifetime shortening depend strongly on distance and nanoparticle concentration, supporting the view that plasmonic enhancement cannot be designed solely from spectral overlap but must incorporate geometry and density [68].

The Purcell effect literature emphasises that large spontaneous emission rate enhancements can be achieved in carefully engineered plasmonic cavities, though these results are often demonstrated under controlled excitation and collection conditions that do not directly map onto broadband solar illumination [74]. For LDS applications, the relevance of Purcell enhancement must therefore be judged by whether it produces net increases in emitted photon flux into the acceptance angles of the underlying solar cell, and whether any additional metal absorption introduces net losses or heating under sunlight [75].

A critical synthesis across studies yields a set of practical design rules for plasmonic–QD coupling in thin films:

First, LSPR tuning should be aligned with either the QD excitation band, the emission band, or both. If the plasmon resonance overlaps strongly with emission, radiative rate modifications are more likely, whereas overlap with excitation can primarily enhance absorption. In practice, the same nanostructure often affects both because plasmon resonances are broad and because broadband illumination excites multiple modes [75].

Second, spacer thickness is a primary control parameter. The MEF literature often reports quenching when emitters are within roughly a few nanometres of the metal, with enhancement emerging over larger separations that can extend to several tens of nanometres depending on system design [55].

This is consistent with the practical observation that an "optimum" spacer thickness exists, beyond which the field enhancement decays, and below which non-radiative energy transfer dominates. Third, nanoparticle density and morphology matter as much as size. Dense films can increase near-field coupling but also increase absorption losses and create inhomogeneous hotspots that broaden behaviour across the film. Morphology also determines whether the system behaves like isolated nanoparticles, coupled arrays, or quasi-continuous metallic films, each with different distance scaling of enhancement and quenching [75].

Fourth, claims of plasmonic "enhancement" should report both intensity changes and lifetime changes, because an intensity increase without an accompanying lifetime change can indicate improved light extraction or scattering rather than true radiative-rate modification. Conversely, lifetime shortening with intensity loss is a signature of quenching. The Purcell and MEF literatures repeatedly stress the necessity of combined intensity and lifetime evidence [76]. The implications for LDS layers are mixed but promising. A plasmonic subsystem could increase the effective photon yield of an LDS layer if it increases radiative emission into the cell, but practical designs must mitigate parasitic absorption in the metal and ensure that the spacer and nanoparticle layers are compatible with scalable, stable transparent coatings. The need for a spacer also introduces an extra optical interface, which can increase reflection unless index-matched [76].

Table 2.2 below summarises reported qualitative behaviours as a function of design parameters, focusing on spacer dependence because it is the most transferable "rule of thumb" to LDS-type layered coatings.

Table 2-2: Plasmonic design parameters for luminescent down-shifting layer design

Plasmonic design parameter	**Typical design choices in literature**	**Observed PL effect trend**	**LDS-specific implication**
Metal type	Au and Ag dominate, chosen for visible LSPR; Al appears for UV plasmonics in some contexts [75].	Metal selection shifts resonance and loss, with Ag often higher field but higher oxidation sensitivity [77].	Metal stability and encapsulation become part of LDS ageing design, not optional [77].

Nanostructure geometry	Nanoparticles, nanorods, microplates, nanocavities, coupled arrays [70].	Strong geometry dependence, hotspot-based structures can show large rate changes but are less uniform [69].	Uniform, large-area LDS coatings favour scalable geometries, potentially trading peak enhancement for reproducibility [55].
Spacer thickness	A few nm to tens of nm dielectric spacers (polymers, silica, oxides) [70].	Quenching dominates at very small spacing, enhancement appears at intermediate distances, decays at large distances [55].	Spacer optimisation must be integrated with optical coupling and anti-reflection constraints of the LDS stack [51].
Density and coverage	Sparse to near-percolated films [72].	Higher density can raise enhancement but increases absorption and can increase quenching probability [72].	For PV, excess metal absorption can reduce net current despite PL boosts, demanding system-level evaluation [51].

The plasmonic–QD literature supports a coherent physical picture, but LDS relevance requires translating narrowband photoluminescence enhancement under controlled excitation into broadband, solar-relevant net photon delivery. Spacer thickness and nanoparticle density emerge as the most transferable design knobs, while parasitic absorption and thermally induced penalties are the most under-addressed risks in PV-facing plasmonic enhancement claims [78].

2.8. PV module thermal behaviour and physics-based operating-temperature models

PV module temperature is governed by an energy balance among absorbed solar irradiance, electrical conversion, convective heat transfer to air, radiative exchange with the sky and surroundings, and conduction to mounting structures. In practice, this balance varies with mounting configuration (open rack, roof mount, building-integrated), wind speed and direction, and atmospheric long-wave radiation, producing systematic deviations from simple “NOCT” style assumptions [79].

Classic temperature models in PV performance tools include:

The Ross model expresses the temperature rise above ambient as proportional to plane-of-array irradiance, implicitly assuming a representative wind speed and quasi-steady behaviour. It is

attractive for simplicity but weak under conditions where wind or mounting strongly modifies heat loss. PV modelling documentation notes these assumptions explicitly, underscoring that Ross is best treated as a coarse baseline [80] .

The Faiman model introduces an empirical heat-loss factor that depends on wind speed, improving realism for many field conditions and becoming influential in standards contexts. PV modelling documentation further notes that IEC temperature measurement and modelling practice has adopted Faiman-type approaches, reflecting a consensus that wind dependence is essential in operational models [81].

The Sandia or SAPM temperature model (often implemented as a back-of-module temperature model with parameters tied to mounting configuration) has been widely used in performance modelling workflows. Its advantage is an empirically calibrated structure that distinguishes module construction and mounting, but its parameters are not universal and must be chosen carefully, otherwise the model can become a "parameter lookup" rather than a predictive mechanism [82].

The Fuentes model represents a more physical, first-principles energy balance approach and is used in common yield tools, providing a path to incorporate geometry, wind heights, emissivity, and absorptance explicitly. By design, it is more complex and data-hungry than empirical models, and its accuracy depends on having the right meteorological inputs and assumptions for radiative exchange [83].

Across these models, the most important critical point is that steady, empirical equations can fail in two ways: (i) structurally, if they omit a dominant term under certain climates (radiative cooling to a cold sky at night or during clear dry days, for example), and (ii) parametrically, if coefficients derived under one mounting or climate are applied elsewhere. Recent modelling work and Sandia documentation emphasise that incorporating radiative losses to the sky can improve common empirical models, indicating that radiative exchange is not a second-order correction but, in some regimes, a primary missing term [84].

A second failure mode concerns dynamics. Thermal inertia creates time constants on the order of minutes to tens of minutes, so a model calibrated on quasi-steady relationships can lag or overshoot during fast irradiance changes, for example passing clouds. The release of an open dataset designed for testing temperature models is significant because it enables systematic validation under varying transient regimes and encourages a shift from "model fits one site" to "model generalises across conditions" [85].

Finally, temperature models are not purely academic. They propagate into energy yield estimates, performance ratio metrics, and fault detection logic. Errors of several degrees can translate into

material energy prediction errors when temperature coefficients are applied, and can distort diagnostic thresholds for hotspot risk. Therefore, the literature trend toward better datasets, model equivalence analysis, and improved parameter extraction should be understood as foundational work for both forecasting and PV reliability analytics [85].

Physics-based PV temperature models are essential and widely deployed, but they embed assumptions that can fail under radiatively dominated conditions and fast transients, and they depend critically on parameter validity for the mounting and climate. The most credible recent shift in the literature is toward open validation datasets and improved handling of radiative losses and dynamics, creating a stronger baseline against which ML models must be compared [85].

2.9. Data-driven thermal modelling and forecasting for PV modules

Data-driven PV temperature prediction spans a continuum from static regression to deep sequence models. In evaluating this literature, three questions are more discriminating than architecture labels: What is the prediction target (cell temperature, back-of-module temperature, or module surface temperature), what is the horizon (nowcasting versus minutes or hours ahead), and does the model generalise beyond the training site and season.

Artificial neural networks (ANNs) have been applied to PV module or surface temperature prediction for years, often using ambient temperature, irradiance, and wind speed as inputs. Such work supports the general conclusion that non-linear regressors can capture temperature relationships better than simple linear correlations when sufficient data exists, but it also reveals sensitivity to data quality and to whether the model is trained in a regime representative of deployment. A representative example is ANN-based surface temperature prediction under measured inputs, which positions ANN as a viable alternative to purely empirical correlations for next-step estimation [86].

Sequence learning models, including LSTM networks, introduce a crucial capability: they can learn thermal inertia implicitly by using a window of past observations. The original LSTM architecture was introduced by Hochreiter and Schmidhuber to address long-term dependency learning problems in recurrent networks, and the PV forecasting community now uses LSTM variants extensively for time-series tasks [87]. For PV temperature prediction specifically, an important methodological choice is the lookback window size: too short and the model cannot learn thermal lag, too long and the model risks learning site-specific periodicity or introducing noise that degrades generalisation.

The PV-temperature literature that explicitly compares ANN and LSTM for panel temperature in hot climates provides a useful, if limited, data point. In the study by Ezzini et al. [88], ANN and LSTM models both achieved test errors on the order of 1 to 2 °C with high R^2, with ANN slightly outperforming LSTM in that specific dataset, underscoring that LSTM is not automatically superior

if the temporal structure is not strong or if the dataset is small. The broader critical interpretation is that architecture superiority is conditional on sampling rate, thermal time constants, and the non-stationarity of the driving inputs.

Beyond neural networks, tree-based ensembles such as XGBoost have become common for PV temperature prediction because they handle non-linearities well, are robust to mixed feature scaling, and offer interpretable feature importance measures. Open access work targeting harsh climates demonstrates that such models can achieve high predictive accuracy and can remain robust across seasons, although some publications still report limited metrics in abstracts and do not fully document leakage control, limiting comparability across studies [89].

Uncertainty quantification is a major gap across PV-temperature ML. Most studies report point-forecast MAE or RMSE but do not quantify predictive uncertainty, which is essential for decision-making under risk, for example thermal derating or hotspot prevention. A practical approach is Monte Carlo dropout, grounded in the interpretation of dropout as approximate Bayesian inference [90]. This approach is attractive because it can be implemented with minor modifications to standard neural networks, but it requires care in calibration and in interpreting uncertainty intervals under distribution shift.

Explainability methods are increasingly used to connect ML predictions to physical drivers. SHAP, introduced by Lundberg and Lee (2017), provides a theoretically grounded way to attribute contributions of each input feature to a given prediction, and has become a default for explainable PV ML because it can be applied to both tree ensembles and neural surrogates, with approximations [91]. However, a critical point is that feature attributions reflect the model's learned correlations, not necessarily causal physics. Therefore, explainability is most credible when the feature set is physically motivated (irradiance, ambient temperature, wind, long-wave radiation proxies) and when attribution stability is tested across seasons and operating regimes.

A second critical issue is dataset quality and openness. The open dataset released through Sandia National Laboratories for PV module operating conditions and temperature provides a benchmark resource because it was designed to test temperature prediction models and includes the main environmental parameters that drive temperature, including downwelling infrared radiation, which is often missing in typical PV plant SCADA datasets [85]. The existence of such datasets shifts the methodological standard: new ML temperature models should demonstrate performance relative to physics-based baselines on open benchmarks, and they should test transfer across subsets and regimes rather than only random train–test splits.

Table 2.3 below compares a selection of accessible studies and benchmarks, focusing on what can be substantiated from openly available sources. Where key values are not provided in accessible text, they are marked as not specified.

Table 2-3: Representative studies on photovoltaic module temperature prediction

Study	**Target and context**	**Model type**	**Inputs and temporal structure**	**Reported performance**	**Generalisation notes**
Ezzini et al. (2025) [88]	PV panel temperature in hot climate context	ANN vs LSTM	Weather inputs, supervised regression, temporal handling not fully detailed in excerpt	Test RMSE about 1.95 to 1.96 °C, MAE about 1.46 to 1.48 °C, R^2 about 0.97	Shows ANN can match or slightly exceed LSTM when temporal dependence is not strongly exploited
Jung et al. (2020) [92]	PV module surface temperature next-step prediction	ANN-based predictive model	Uses measured operational variables, predicts next timestep	Metrics not specified in excerpt	Highlights ANN as viable for short-horizon estimation when data are well curated
Driesse et al. (2023) [85]	Open dataset for validating temperature models, includes key environmental drivers	Dataset and benchmarking resource	Provides irradiance, ambient temperature, wind, downwelling IR, and module temperatures	Not a model result	Enables reproducible benchmarking, supports regime-aware validation

Mehdi et al. (2026) [89]	Desert and semi-arid conditions, includes soiling, multi-technology climate	XGBoost vs linear regression	High-resolution one-year dataset, explicit multi-condition evaluation	R^2 reported about 0.99 for XGBoost in abstract, MAE and RMSE not specified in accessible excerpt	Strong emphasis on robustness across seasons and conditions, but full comparability depends on detailed methodology
Li et al. (2024) [93]	PV panel temperature forecasting, land vs water mounted plants	Multiple ML models including ResNet, RF	Comparative evaluation with numerical simulation baselines	R^2 reported for one case about 0.66 for numerical simulation in water-mounted, detailed MAE and RMSE not specified in abstract	Useful for identifying mounting-specific degradation of baseline models, but full metrics require full text
Ren et al. [94]	Interpretable ML for PV panel temperature, feature engineering plus explainability	Interpretable ML framework using SHAP and boosting	Feature selection combining correlation and SHAP	Detailed MAE and RMSE not specified in accessible excerpt	Highlights emerging trend: accuracy plus interpretability plus extrapolation capability

ML models can predict PV module temperature with high accuracy under controlled conditions, but the literature's central weakness is uneven validation: many studies do not test cross-season and cross-site generalisation, and uncertainty quantification is still uncommon. The emergence of open temperature datasets and established interpretability tools raises the bar, implying that thesis-level contributions should emphasise leakage-safe evaluation, uncertainty, and physically meaningful explanation rather than accuracy alone [95].

2.10. Integrated synthesis and research gaps

A thesis integrating luminescent down-shifting, plasmonically enhanced quantum-dot photoluminescence, and photovoltaic thermal modelling must define research gaps not as generic opportunities for incremental optimization, but as specific unresolved limitations that constrain scientific interpretation, materials integration, and real-world photovoltaic relevance. Across these areas, the central deficiency in the recent literature is the absence of sufficiently integrated strategies that connect nanoscale optical engineering and predictive thermal intelligence to measurable improvements in silicon photovoltaic performance, reliability, and operational understanding.

Within luminescent down-shifting for crystalline silicon photovoltaics, a major unresolved issue concerns the development of perovskite quantum-dot coatings that can simultaneously deliver high photoluminescence efficiency, low parasitic optical loss, effective interfacial passivation, and compatibility with planar polymer-based device integration. Recent studies have confirmed the promise of $CsPbBr_3$ and related perovskite nanocrystals as spectral conversion materials for silicon photovoltaics, yet reported approaches have remained dominated by EVA-based encapsulation, conventional oleate or oleylamine ligand systems, or optoelectronic platforms that are not fully representative of crystalline silicon PV operation. Consequently, comparatively limited attention has been given to coating architectures in which nanocrystal synthesis, surface functionalization, and polymer integration are deliberately designed as a unified photovoltaic interface. This omission is scientifically important because the effectiveness of an LDS layer is governed not only by nanocrystal emission properties, but also by film-state photoluminescence quantum yield, interfacial defect chemistry, optical transparency, self-absorption losses, and compatibility with the silicon device surface.

A closely related gap concerns stability at the level of the integrated photovoltaic coating rather than the isolated nanocrystal or composite material. Although substantial progress has been reported through shell engineering, ligand modification, and polymer encapsulation, many PMMA-based $CsPbBr_3$ composites have been developed primarily for display, photonic, or scintillation applications rather than for broadband solar spectral conversion under realistic photovoltaic operating conditions. Moreover, these systems have generally not been designed around interfacial chemistries capable of simultaneously suppressing trap-assisted recombination and strengthening coupling between the nanocrystal surface and the host matrix. As a result, the literature still reveals a clear disconnect between highly luminescent laboratory composites and photovoltaic LDS coatings requiring stable, spectrally matched, low-loss performance under one-sun irradiation and thermally relevant conditions. The unresolved materials challenge, therefore, lies in developing chemically engineered

perovskite quantum-dot/polymer coatings in which optical efficiency, interfacial passivation, and operational robustness are treated as coupled design requirements.

A further limitation in the LDS literature is conceptual as well as technological. Many reported improvements in silicon device performance are attributed to luminescent down-shifting without adequately separating genuine spectral conversion effects from concurrent anti-reflection, scattering, or surface-passivation contributions. Consequently, the field still lacks sufficient studies in which coating chemistry, film optics, and device-level response are interpreted within a single integrated framework. For a thesis concerned with application-oriented spectral management, the key unresolved question is therefore not merely whether perovskite quantum dots can improve silicon photovoltaic response, but how chemically tailored, polymer-integrated LDS coatings can be designed and evaluated such that the origin, magnitude, and photovoltaic significance of any performance gain are scientifically robust and practically meaningful.

The plasmonic quantum-dot literature reveals a different but related translational limitation. Although it is well established that metal nanostructures can enhance or quench photoluminescence depending on spectral overlap, local field intensity, and emitter-metal separation, progress toward reproducible device-relevant implementation remains limited by fabrication routes that do not permit sufficiently controlled nanoparticle morphology, surface coverage, and spatial arrangement. Much of the existing literature has relied on colloidal Au nanoparticle synthesis, which is valuable for proof-of-concept demonstrations but less effective for establishing scalable and morphology-controlled design rules. The unresolved issue is therefore no longer whether plasmonic enhancement is possible in principle, but how it can be engineered within a fabrication platform that enables systematic control of structural parameters governing localized surface plasmon resonance and emitter coupling.

Within plasmonically coupled CdSe/CdS systems specifically, spacer-layer engineering remains a decisive but still incompletely resolved variable. Prior studies broadly recognize that very small emitter-metal separations tend to favor non-radiative energy transfer and luminescence quenching, whereas intermediate distances can promote local field enhancement and increased radiative emission. However, the literature has not yet established sufficiently clear morphology-distance-performance relationships for CdSe/CdS core-shell quantum dots coupled with Au nanostructures produced by scalable physical deposition methods. This leaves an important gap in the development of reproducible plasmonic luminescent platforms, particularly for applications requiring controlled enhancement rather than isolated demonstrations of intensity variation. Accordingly, there remains a need for distance-resolved and morphology-controlled investigations capable of identifying quantitative design windows for plasmonically enhanced quantum-dot emission and, more broadly, for engineering optical coupling with greater precision.

The photovoltaic thermal modelling literature exposes an equally important gap at the system level. Module temperature is a fundamental determinant of voltage loss, conversion efficiency, and long-term reliability, yet direct forecasting of PV module temperature remains less mature than the prediction of irradiance or electrical output. Classical physics-based approaches, including Ross, Faiman, SAPM, and Fuentes-type formulations, remain important because they are interpretable and physically grounded, but their predictive robustness can deteriorate under transient irradiance, fluctuating wind conditions, and complex radiative or convective environments. Conversely, many machine-learning studies report high predictive accuracy while representing environmental variables as independent tabular inputs, thereby underestimating temporal memory and thermal inertia, both of which are intrinsic to PV heat dynamics. The resulting methodological gap is the lack of forecasting frameworks that simultaneously preserve physical relevance, capture sequential thermal behaviour, and remain suitable for deployment under realistic operating variability.

A further unresolved issue in data-driven PV thermal forecasting concerns model trustworthiness. Much of the recent literature emphasizes point prediction accuracy, whereas comparatively less attention has been given to uncertainty quantification, explainability, and direct benchmarking against accepted physical thermal models within a unified framework. This omission is significant because predictive tools intended for PV monitoring, fault diagnosis, digital twins, and operational optimization must be not only accurate, but also interpretable, transparent in their confidence, and credible across changing environmental regimes. The literature therefore still lacks sufficiently integrated thermal modelling studies in which sequential learning, uncertainty awareness, interpretability, and physics-based benchmarking are treated as concurrent requirements rather than separate objectives.

Taken together, these gaps indicate a broader thesis-level deficiency extending across both the optical and thermal domains. In the optical literature, the central challenge is to translate advances in quantum-dot materials and plasmonic coupling into planar, polymer-compatible, and quantitatively validated strategies for improving silicon photovoltaic light harvesting. In the thermal literature, the corresponding challenge is to translate predictive performance into models that are physically credible, temporally informed, and operationally trustworthy. The common scientific problem is therefore one of translation and integration, namely, how to move from material-level or algorithm-level promise toward rigorously demonstrated photovoltaic relevance at the device and system levels.

The integrated research gap addressed in this thesis is the absence of application-oriented frameworks that connect advanced optical materials engineering and predictive thermal modelling to photovoltaic performance in a scientifically rigorous and practically meaningful manner. On the optical side, the literature lacks sufficiently mature strategies for chemically engineered, polymer-integrated

perovskite quantum-dot luminescent down-shifting coatings on crystalline silicon, as well as reproducible plasmonic design frameworks that relate nanoparticle morphology and emitter-metal spacing to controlled enhancement of core-shell quantum-dot emission. On the thermal side, the literature lacks forecasting frameworks for PV module temperature that are simultaneously sequence-aware, uncertainty-informed, interpretable, and benchmarked against established physical models. Collectively, these gaps justify a unified thesis centred on enhancing silicon photovoltaic performance through coupled advances in spectral management, nanoscale optical control, and data-driven thermal intelligence.

Chapter.3 Polymer-Integrated Surface-Passivated $CsPbBr_3$ Quantum Dots for Luminescent Down-Shifting in Crystalline Silicon Solar Cells

In the previous chapter, it has been established that, despite the technological maturity and market dominance of crystalline silicon photovoltaics, spectral mismatch remains a persistent limitation, particularly in the ultraviolet and short-wavelength visible regions, where front-surface losses reduce the effective utilization of high-energy photons [14], [18]. In this context, external photon-management strategies have attracted increasing attention as practical approaches for improving device performance without modifying the underlying junction architecture. Among these, luminescent down-shifting, LDS, has been widely recognized as a viable optical route for converting poorly utilized high-energy photons into longer wavelengths that are more effectively absorbed by silicon [17], [51].

The literature further indicates that a wide variety of LDS materials, including rare-earth phosphors, organic dyes, carbon-based luminophores, and semiconductor quantum dots, have been investigated for this purpose [61], [62], [96]. Although these studies have confirmed the feasibility of the LDS concept, they have also demonstrated that practical implementation remains dependent on the simultaneous fulfilment of several material and device requirements, including strong absorption in the UV-blue region, high photoluminescence quantum yield, low self-absorption, optical transparency, and adequate environmental stability [51], [57], [96]. Consequently, the present challenge in LDS research is not limited to the identification of emissive materials, but extends to the development of coating architectures capable of preserving their photophysical performance under device-relevant conditions.

3.1. Background

Luminescent down-shifting, LDS, has been extensively investigated as an external spectral-conversion strategy for silicon photovoltaics because it addresses the limited utilization of high-energy photons in crystalline silicon devices. Ultraviolet and blue photons are absorbed within the near-surface region of the cell, where parasitic absorption in front layers and surface recombination processes reduce their effective contribution to photocurrent generation. LDS coatings are designed to mitigate this limitation by incorporating photoluminescent centers into a transparent matrix that absorbs such photons and re-emits them at longer wavelengths, where optical penetration into silicon is greater and carrier collection is more favorable [63], [72], [97]. A broad range of LDS emitters has therefore been explored, including Eu-doped phosphors, organic dyes, carbon dots, and semiconductor quantum dots [57], [96], [97], [98]. Collectively, these studies validate the

fundamental principle of LDS, while also indicating that the magnitude of photovoltaic benefit remains highly sensitive to absorption strength, photoluminescence quantum yield, self-absorption losses, film transparency, and long-term environmental stability [9], [58].

Among the different classes of LDS emitters, all-inorganic lead halide perovskite quantum dots, particularly $CsPbBr_3$, have emerged as particularly promising materials owing to their strong absorption cross section, narrow emission linewidth, high color purity, and favorable spectral overlap with the response range of silicon [51], [99].These characteristics make $CsPbBr_3$ especially attractive for short-wavelength spectral conversion. However, its application in photovoltaic coatings remains constrained by persistent materials-related limitations. Although perovskite nanocrystals are often considered relatively defect tolerant, surface chemistry remains critically important in LDS systems, where nonradiative recombination directly reduces photon-conversion efficiency [100], [101]. In practice, $CsPbBr_3$ quantum dots remain susceptible to ligand desorption, surface trap formation, aggregation, moisture, oxygen, ultraviolet exposure, and thermal stress, all of which can degrade photoluminescence efficiency and compromise long-term coating performance [69], [102]. This issue is particularly significant for front-side photovoltaic coatings, which must maintain optical quality during extended operation under illumination and elevated temperature.

For this reason, recent studies have increasingly focused on stabilization through interfacial passivation and encapsulation. Silica-based protection has been widely investigated because it can reduce environmental degradation and suppress trap-mediated nonradiative recombination [57], [73]. In parallel, ligand engineering has gained importance because conventional oleic acid and oleylamine ligand shells are dynamically bound and may rearrange or detach during purification, film formation, or ageing, thereby generating additional nonradiative pathways [99], [103]. More recent investigations have therefore examined cross-linkable ligands, zwitterionic ligands, and organosilicon functional molecules capable of forming more robust interfacial structures [104], [105]. In this context, 3-aminopropyltriethoxysilane, APTES, is of particular interest because it can interact with the nanocrystal surface and hydrolyse to form a silica-rich interphase, thereby providing both chemical passivation and structural protection [66], [106], [107]. Such interfacial structures are particularly relevant for LDS films, where suppression of trap-assisted recombination is directly associated with improved radiative performance.

In addition to surface modification, polymer incorporation has become an important consideration in the design of practical LDS coatings. The host matrix influences optical transparency, nanocrystal dispersion, environmental stability, and film processability. Among the host materials reported in the literature, EVA and PMMA are among the most frequently studied [24], [57], [97], [108]. EVA has been widely employed in module-compatible laminates and composite LDS systems, including recent

$CsPbBr_3$-based photovoltaic demonstrations [58], [109]. PMMA, however, remains particularly attractive for thin-film coating applications because of its high optical transparency, solution processability, and ability to limit aggregation while stabilizing luminescent nanocrystals in the solid state. Nevertheless, PMMA-based perovskite quantum-dot composites have more commonly been investigated for general light-conversion, display, or scintillation applications than for front-side spectral management in silicon photovoltaics [72], [107], [108]. Furthermore, polymer encapsulation alone does not fully address the interface problem, since the performance of the resulting composite remains strongly dependent on the quality of the nanocrystal surface and its compatibility with the surrounding polymer matrix [103], [110].

3.2. Problem Statement

Despite the strong optical potential of $CsPbBr_3$ quantum dots for luminescent down-shifting, the literature does not yet provide a sufficiently integrated strategy for their implementation as photovoltaic coatings. Beyond encapsulation, there is a growing body of work that couples perovskite nanocrystals with spectrally selective and light management structures directly atop photovoltaic devices. Cao et al. recently used $CsPbBr_3$ QDs as light converting layers in Si nanowire hybrid solar cells, demonstrating nonradiative energy transfer effects that extend the device response to sub band gap photon energies [111]. On the perovskite solar cell side, light management composites that combine scattering, anti reflection, and spectral conversion functionalities have been shown to enhance both PCE and photostability, underscoring the broader relevance of multifunctional optical coatings in photovoltaics [112]. Nevertheless, there remains a clear gap between highly stable PQD–polymer composites developed for the specific demands of LDS layers in c-Si solar cells, where the coating must maintain high PLQY, minimal self-absorption, and excellent stability under prolonged one sun equivalent illumination and realistic thermal cycling.

In this context, there is still limited work on $CsPbBr_3$ LDS layers that simultaneously exploit LARP based synthesis, APTES mediated surface functionalization, and PMMA embedding, especially in direct conjunction with crystalline Si solar cells. Existing $CsPbBr_3$ LDS films for Si typically rely on EVA matrices and conventional oleate type ligands [58], [113], or they focus on photodetectors rather than photovoltaic operation [100], [114]. Moreover, Novikova et al. have shown that APTES modification can improve the stability and functionality of LARP-synthesized $CsPbBr_3$ PQDs [115]. The integration of such APTES-treated PQDs into a PMMA matrix as a planar LDS coating on c-Si solar cells has, to the best of our knowledge, not been reported. To address this gap. $CsPbBr_3$ PQDs were synthesized via ligand-assisted reprecipitation, passivated with APTES to create an inorganic–organic interphase, and incorporated into a PMMA matrix to form transparent down-shifting coatings for crystalline Si solar cells. PMMA was selected because it is optically transparent in the visible

region, solution-processable, compatible with QD dispersion, and able to reduce nanocrystal aggregation in the solid film. APTES treatment improves surface passivation by promoting a silica-rich interphase, which reduces trap-assisted nonradiative recombination. This architecture yields strong and spectrally well-matched photoluminescence, which enhances short circuit current density, and improves power conversion efficiency relative to uncoated reference cells, while the APTES/PMMA encapsulation is expected to improve the PQDs' performance as reported in the literature [106], [108], [116]. In this architecture, LARP synthesis provides room-temperature QD formation, APTES improves surface passivation through a silica-rich interphase, and PMMA provides a transparent host matrix for film integration. This combination of LARP-synthesized $CsPbBr_3$, 3-Aminopropyltriethoxysilane surface engineering, and PMMA-based LDS integration on c-Si devices constitutes the central novelty of the present work.

3.3. Experimental section

All syntheses and film preparation steps were carried out at room temperature unless stated otherwise.

3.3.1 Materials used

All the materials were purchased from Sigma Aldrich and used without any further purification, including Lead (II) bromide (PbBr2, 98+%), Cesium Bromide (CsBr, >98%), Oleic acid (OA, 90%), Oleylamine (OAm, 80-90%), 3-Aminopropyltriethoxysilane (3-APTES, ≥98.0%) and Toluene (99.5%).

3.3.2 Synthesis of $CsPbBr_3$ quantum dots

The QDs were synthesized using the procedure as demonstrated by Mo et al., with slight modifications. [117]. Firstly, PbBr2 (0.4 mmol) and CsBr (0.4 mmol) were dissolved in DMF (10 mL) and stirred for 1 h until a clear solution was obtained. Oleic acid (OA, 0.6 mL) and oleylamine (OAm, 0.2 mL) were then added, followed by stirring for an additional 30 min. For quantum dot formation, 1 mL of the precursor solution was rapidly injected into toluene (10 mL) under vigorous stirring (1500 rpm) for 10 s. Finally, the QDs were further purified by centrifugation of the reaction solution at 10,000 rpm for 10 min, followed by redispersal in Toluene. All the syntheses were carried out at room temperature.

3.3.3 Synthesis of $CsPbBr_3$@SiO_2 quantum dots using 3-APTES

For silica coated quantum dots, 1 mL of the precursor solution was rapidly injected into toluene (10 mL) containing 3-aminopropyltriethoxysilane (3-APTES, 0.69 µL) under vigorous stirring (1500 rpm) for 10 s. Finally, the QDs were further purified by centrifugation of the reaction solution at 10,000 rpm for 10 min and then re-dispersed in Toluene. All the synthesis was done at room temperature.

3.3.4 Preparation of PMMA-embedded LDS solutions

Luminescent down-shifting (LDS) formulations were prepared by embedding either $CsPbBr_3$ QDs (bare) or $CsPbBr_3@SiO_2$ QDs into a PMMA matrix using toluene as the solvent. For each formulation, firstly, PMMA was dissolved in toluene by continuous stirring until it was completely dissolved. Then, PMMA and QD stock solutions were combined and diluted to a total volume of 2.0 mL. PMMA mass was varied between 10 and 40 mg per 2 mL, corresponding to 5, 10, 15, and 20 mg/mL, and represented by corresponding letters from A to D, respectively. For each PMMA concentration, five QD loadings were prepared using QD stock loadings of 0.5×, 0.75×, 1.0×, 1.25×, and 1.5× relative to a reference stock volume. Silane-modified $CsPbBr_3$ samples are represented by the prefix S. The formulation series was designed to identify the balance between QD absorption, film transparency, and concentration-dependent optical losses. Varying PMMA content and QD loading independently allows the effects of polymer matrix concentration and nanocrystal loading to be separated on the optical and photovoltaic responses. The full sample matrix is provided in Table 3.1.

Table 3-1: Sample Matrix for LDS formulations

Bare QDs Sample ID	**Silane-modified QDs Sample ID**	**PMMA mg in 2 mL**	**Final PMMA mg/mL**	**QDs from stock in ml**
A1	S-A1	10	5	0.5×
A2	S-A2	10	5	0.75×
A3	S-A3	10	5	1.0×
A4	S-A4	10	5	1.25×
A5	S-A5	10	5	1.5×
B1	S-B1	20	10	0.5×
B2	S-B2	20	10	0.75×
B3	S-B3	20	10	1.0×
B4	S-B4	20	10	1.25×

B5	S-B5	20	10	1.5×
C1	S-C1	30	15	0.5×
C2	S-C2	30	15	0.75×
C3	S-C3	30	15	1.0×
C4	S-C4	30	15	1.25×
C5	S-C5	30	15	1.5×
D1	S-D1	40	20	0.5×
D2	S-D2	40	20	0.75×
D3	S-D3	40	20	1.0×
D4	S-D4	40	20	1.25×
D5	S-D5	40	20	1.5×

3.4. QDs concentration calculation section

The concentration of $CsPbBr_3$ nanocrystals was determined using a size-dependent molar extinction coefficient approach reported by Maes et al [118]. This method enables estimation of nanocrystal particle molarity from UV-visible absorption measurements when the nanocrystal size and morphology are known.

The average nanocrystal core size was determined from high resolution transmission electron microscopy (HRTEM) images. The nanocrystals exhibit a well defined cubic morphology with an average edge length of 9.64 nm and a relatively narrow size distribution, justifying the use of a single mean size for extinction coefficient estimation.

For optical measurements, 50 µL of the as synthesized nanocrystal stock dispersion was diluted with 1950 µL of toluene, corresponding to a dilution factor of 40. UV visible absorption spectra were recorded using a quartz cuvette with a 1 cm optical path length. Baseline subtraction was applied to remove solvent and scattering contributions. The first excitonic absorption peak was observed at 500 nm, and the absorbance at this wavelength was measured to be 0.035.

The molar extinction coefficient (ϵ) of the $CsPbBr_3$ nanocrystals was calculated using the empirical size dependent relation reported by Maes et al.[1]

$\epsilon = 2.42 \times 10^{-2} \times d^3$

where d is the nanocrystal edge length in nanometers and ϵ is expressed in units of $cm^{-1} \cdot \mu M^{-1}$. Substituting d = 9.64 nm yields an extinction coefficient of 21.7 $cm^{-1} \cdot \mu M^{-1}$.

The nanocrystal concentration in the diluted dispersion was calculated using the Beer–Lambert law, A = ϵcl, where A is the absorbance at 500 nm, c is the nanocrystal concentration, and l is the optical path length. Using A = 0.035 and l = 1 cm, the particle concentration of the diluted sample was calculated to be 0.0016 µM. After correcting for the dilution factor, 2000/50 = 40, the nanocrystal concentration of the stock dispersion was determined to be 0.065 µM which is denoted in this paper as C_stock, corresponding to 6.5×10^{-8} mol L^{-1} of nanocrystal particles.

For LDS solutions prepared to a final volume of 2.0 mL, the final QD concentration is C_final = Dilution factor × C_stock, where C_stock is the molar concentration of the stock used. Interpreting 0.5×, 0.75×, 1.0×, 1.25×, and 1.5× as QDs volume contribution from stock solution to make final 2 ml solution in toluene for the following 0.50, 0.75, 1.00, 1.25, and 1.50 mL, respectively and x represents the dilution factor which is equal to volume contribution of QD/total volume, the estimated final QD concentrations are given in the Table 3.2 below;

Concentration Interpretation

Table 3-2: Calculated concentrations of $CsPbBr_3$ quantum dots in LDS solutions prepared with different stock solution volumes

LDS formulation	**QD Volume used**	**C_Stock**	**Dilution Factor**	**C_Final=C_stock × (V_QD / V_total)**
0.5x	0.50 ml	0.065 µM	500/2000= 0.25	0.01625 µM
0.75x	0.75 ml	0.065 µM	750/2000=0.375	0.0244 µM
1.0x	1.00 ml	0.065 µM	1000/2000=0.5	0.0325 µM
1.25x	1.25 ml	0.065 µM	1250/2000=0.625	0.0406 µM
1.5x	1.50 ml	0.065 µM	1500/2000=0.75	0.0488 µM

3.4.1 Deposition of LDS layers on c-Si mini modules

Each LDS formulation (50 μL) was deposited onto polycrystalline silicon mini-modules by the doctor-blade method, and the film thickness was controlled by tapes (3M Corporation. Samples were covered with a glass lid during drying to slow solvent evaporation and improve film uniformity. The samples were allowed to dry slowly for 1 hour and were then kept in the open air for an additional 30 minutes. The mini module, consisting of multiple sub-cells connected in series, is supplied by SUNYIMA. The illuminated device area used for PV performance calculations was 5.3 cm^2. The solar simulator (IV-5, PV Measurements Company) was calibrated using its standard reference cell before all measurements to ensure consistent illumination intensity. Therefore, the comparison between reference and LDS-coated devices is based primarily on relative changes in photovoltaic parameters obtained under identical measurement conditions.

X-ray photoelectron spectroscopy (XPS) measurements were carried out using a Thermo Scientific Escalab 250Xi spectrometer equipped with an Al Kα radiation source as the probe beam. The base pressure of the analysis chamber was maintained at approximately 2×10^{-10} Torr. Surface etching was performed using Ar^+ ion sputtering at an energy of 3.0 keV for a duration of 10 s to remove surface contaminants and obtain depth-resolved information. The crystalline structure of the samples was analyzed by X-ray diffraction using a Rigaku Ultima IV diffractometer with Cu Kα radiation (λ = 1.5406 Å). The microstructural and morphological features were examined using transmission electron microscopy (TEM) performed on a JEOL JEM-2100F microscope operated at an accelerating voltage suitable for high-resolution imaging. Optical absorption properties were recorded using a JASCO UV-Vis spectrophotometer (model 670). Photoluminescence (PL) spectra were obtained with a HORIBA Jobin Yvon Fluorolog-3 spectrofluorometer. Photovoltaic performance measurements were conducted using a Keithley 2400 source meter connected to an IV-5 solar simulator supplied by PV Measurements Company. The measurements were performed under standard AM 1.5G illumination with an intensity of 100 $mW \cdot cm^{-2}$. Each measurement was repeated four times for each formulation to incorporate the process variability and reproducibility.

3.5. Results and Discussion

3.5.1 Structural and phase analysis by XRD

Figure 3.1 shows the X-ray diffraction (XRD) patterns of bare $CsPbBr_3$ quantum dots and silica-modified $CsPbBr_3@SiO_2$ quantum dots. The diffraction peaks at $2\theta \approx 15°$, 21°, 30°, 34°, 37°, and 43° correspond to the phase-pure perovskite $CsPbBr_3$ nanocrystals, with no clear evidence of secondary crystalline impurities such as Cs_4PbBr_6 or $PbBr_2$ within the detection limit of XRD, which verifies the phase purity of both samples. It is also significant that the lack of any measurable peak shift upon

SiO_2 modification means that this silane-mediated surface treatment does not modify the bulk lattice parameters of the $CsPbBr_3$ core or crystal symmetry. Similar retention of the $CsPbBr_3$ crystal structure after surface passivation and encapsulation has been widely reported for perovskite quantum dots treated with oxide shells or silane-based ligands, where surface chemistry primarily affects interfacial states rather than the perovskite lattice itself [24], [104], [115].

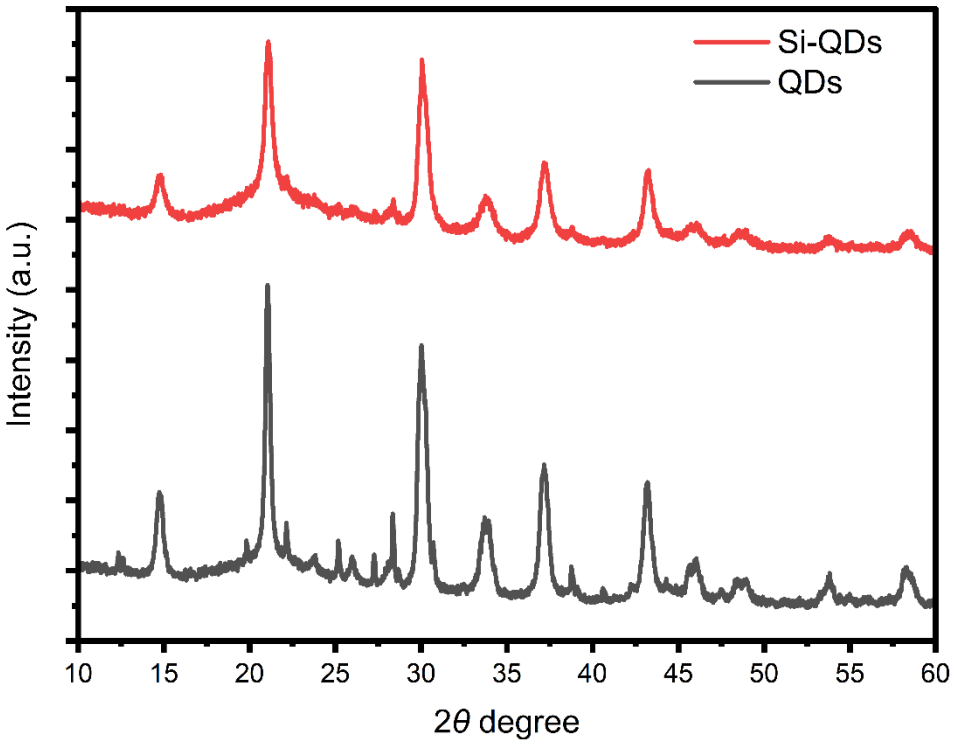

Figure 3-1: X-ray diffraction (XRD) patterns of bare $CsPbBr_3$ and APTES-modified $CsPbBr_3@SiO_2$ quantum dots

Compared to the bare $CsPbBr_3$ QDs, the $CsPbBr_3@SiO_2$ sample exhibits a reduction in diffraction peak intensity along with slight peak broadening. This behavior can be attributed to the nanoscale crystallite size and the presence of an amorphous SiO_2 shell, which does not contribute distinct diffraction peaks but attenuates the diffracted intensity from the crystalline perovskite core. Similar intensity suppression and broadening effects have been reported for silica encapsulated $CsPbBr_3$ and other perovskite nanocrystals, where an amorphous oxide layer surrounds the crystalline core without inducing new crystalline phases. The preservation of the $CsPbBr_3$ phase after SiO_2 modification confirms that the improved optical and luminescent down-shifting performance discussed later arises from surface passivation and interfacial defect suppression rather than from changes in crystal structure, an important requirement for stable and spectrally well defined LDS coatings on crystalline silicon solar cells [58], [119].

3.6. TEM and size distribution, morphology

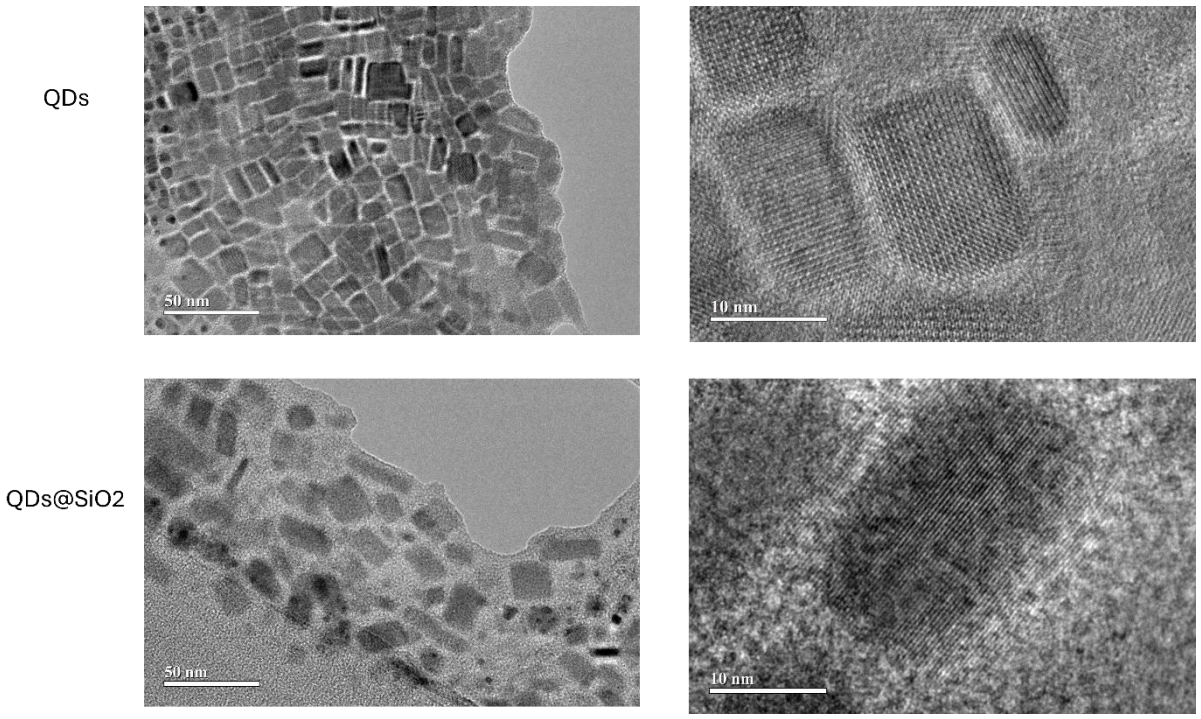

Figure 3-2: Transmission electron microscopy (TEM) images and size distribution of $CsPbBr_3$ and $CsPbBr_3@SiO_2$ quantum dots.

Transmission electron microscopy confirms that both bare $CsPbBr_3$ and silica-modified $CsPbBr_3@SiO_2$ quantum dots consist of well-defined, faceted nanocrystals with sizes in the quantum confinement regime, as shown in Figure 2. The particles are mostly near cubic morphology with good dispersion, confirming the phase-pure perovskite structure identified by XRD. Figure 2 shows that the lattice fringes extend across individual nanocrystals, which indicates that the crystalline $CsPbBr_3$ core is retained after SiO_2 modification. The $CsPbBr_3@SiO_2$ sample exhibits a weak, diffuse contrast around the crystalline core due to the formation of an amorphous silica-rich interphase from APTES hydrolysis and condensation. Similar preservation of lattice fringes together with amorphous oxide shells has been reported for silane and silica encapsulated $CsPbBr_3$ quantum dots, where surface encapsulation improves stability without inducing secondary crystalline phases or lattice distortion [71], [104].

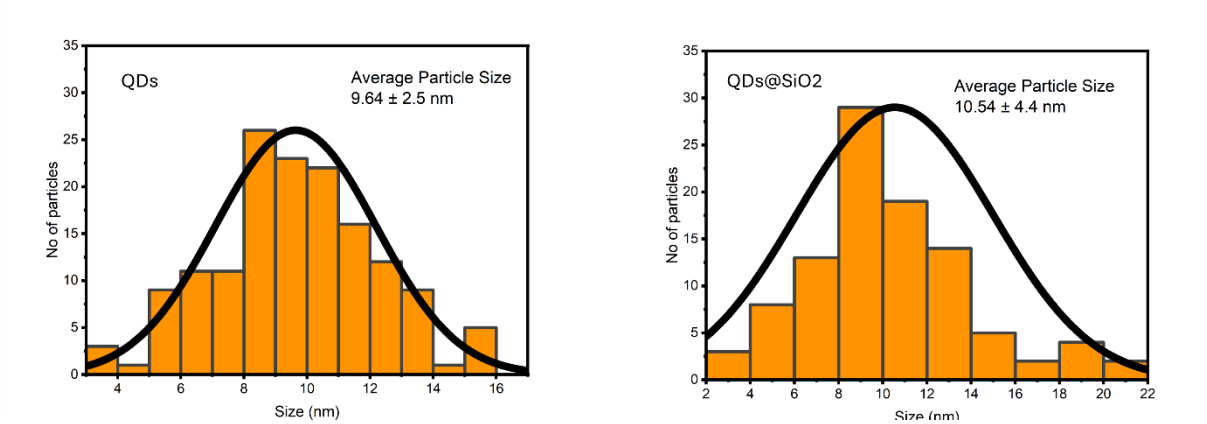

Figure 3-3: Particle Size Distribution of Bare-$CsPbBr_3$ and $CsPbBr_3$@SiO_2

Figure 3.3 shows the particle size distribution of bare $CsPbBr_3$ and $CsPbBr_3$@SiO_2. Statistical analysis of particle sizes (n>100) extracted from TEM images yields an average edge length of 9.64 ± 2.5 nm for bare $CsPbBr_3$ QDs and 10.54 ± 4.4 nm for $CsPbBr_3$@SiO_2 QDs. The slightly larger mean size and broader distribution observed after SiO_2 modification are attributed to the contribution of the silica-rich interphase to the projected particle edge length measured by TEM, as well as to local variations in shell thickness. Importantly, the core sizes of both samples remain comparable, indicating that the pronounced differences in absorption and photoluminescence behaviour discussed earlier do not originate from changes in quantum confinement. Instead, these results support a surface passivation-driven mechanism, where the silica interphase suppresses defect-related recombination while maintaining the intrinsic electronic structure of the $CsPbBr_3$ core, in line with recent reports on oxide-encapsulated perovskite quantum dots developed for optoelectronic and luminescent downshifting applications [103], [115].

3.7. XPS chemical surface analysis

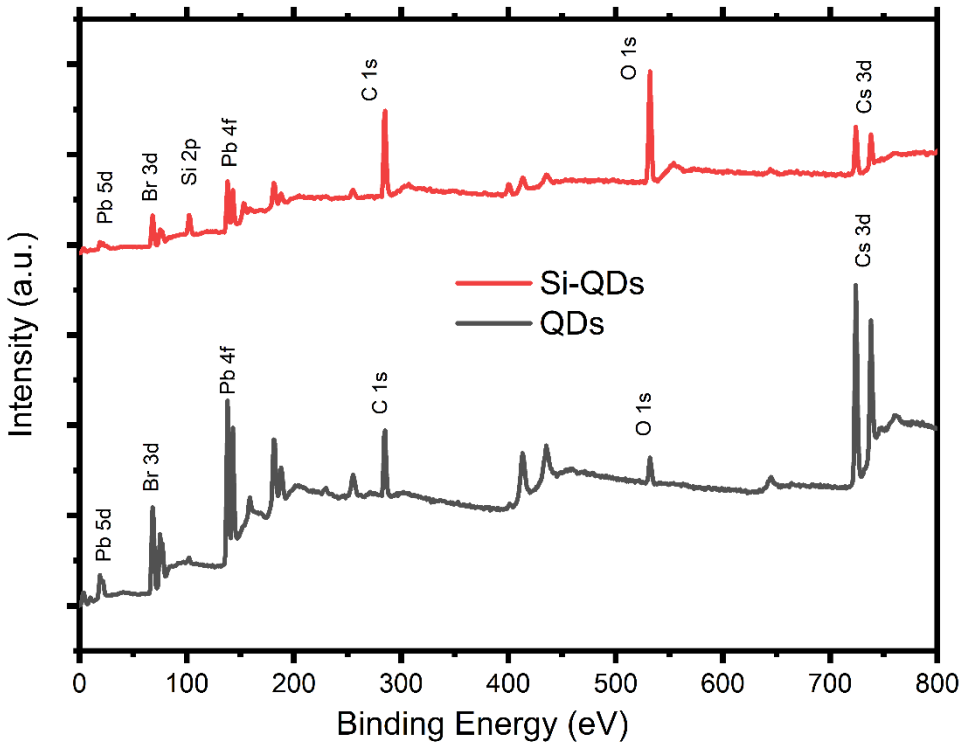

Figure 3-4: X-ray photoelectron spectroscopy (XPS) survey spectra of $CsPbBr_3$ and $CsPbBr_3$@SiO_2 quantum dots.

X-ray photoelectron spectroscopy (XPS) was performed to evaluate the surface chemical composition and interfacial bonding of bare $CsPbBr_3$ quantum dots and APTES modified $CsPbBr_3$@SiO_2 quantum dots. Figure 3.4 gives the survey spectra, which show sharp Pb 5d, Pb 4f, Br 3d, and Cs 3d core level peaks from both samples that indicate the chemical integrity of the $CsPbBr_3$ perovskite lattice is retained during surface modification. Moreover, C 1s and O 1s signals are pronounced and can be ascribed to both the surface ligands and PMMA host matrix. For the APTES-treated sample, a prominent new Si 2p peak along with an enhancement in O 1s intensity is indicative of the presence of silicon at the quantum dot surface. This suggests a silica-rich interphase was formed around the perovskite core. This interphase is amorphous and thus not detected by XRD, but is important to passivate undercoordinated Pb sites and halide-related surface defects. The presence of sharp Pb and Cs core level features is further evidence that the silane-mediated treatment does not destroy the perovskite framework but introduces effective surface passivation. These results represent a direct chemical link between APTES-based surface engineering and the observed improvements in photoluminescence efficiency and luminescent downshifting performance of $CsPbBr_3$@SiO_2 embedded PMMA coatings.

3.8. Absorption and PL

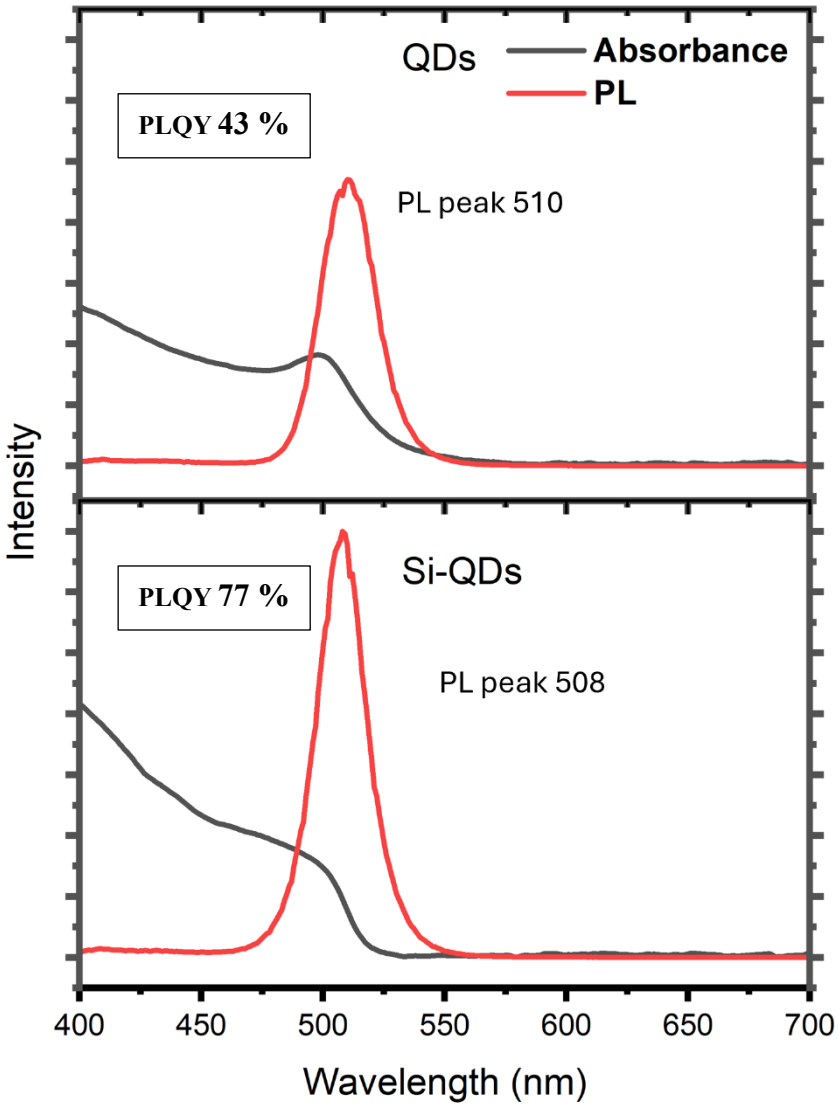

Figure 3-5: UV–visible absorption and photoluminescence spectra of bare $CsPbBr_3$ and $CsPbBr_3@SiO_2$ quantum dots.

The absorption and photoluminescence (PL) spectra of bare $CsPbBr_3$ quantum dots and silica modified $CsPbBr_3@SiO_2$ quantum dots are compared in Figure 3.5. Both samples show broad UV–blue absorption followed by a pronounced excitonic edge at ca. 500 nm, as well as a narrow green emission peak centred at 510 nm for bare QDs and 508 nm for Si QDs. The limited blue shift after silica modification corresponds to a change of the local dielectric environment and surface electronic structure rather than a modification of the $CsPbBr_3$ crystal phase, in agreement with XRD and HRTEM data confirming an immutable lattice structure as well as crystallinity. The emission wavelengths reside in the optimal spectral window for luminescent downshifting on crystalline silicon, where emitted photons are readily absorbed by the Si absorber, as widely reported for $CsPbBr_3$ based spectral conversion layers [51].

The silica modified sample displays a substantially sharper and more intense PL peak along with a wider absorption envelope in the UV–blue region when compared to bare QDs. The increased PL intensity and decreased linewidth suggest that the radiative recombination of the QDs is more efficient owing to a powerful surface passivation provided by the organ siloxane network derived from APTES and rich silica interphase. This passivation suppresses the formation of halide vacancies and undercoordinated Pb sites, minimizes trap assisted recombination, and limits exciton–phonon coupling yielding spectrally purer band-edge emission. Similarly, the PL sharpening and intensity enhancement after silane or silica-based surface engineering have been frequently observed for $CsPbBr_3$ quantum dots and other perovskite nanocrystals[24], [104]. By contrast, the broader absorption for $CsPbBr_3@SiO_2$ is likely a result of interfacial dielectric effects and increased light scattering through the silica modification, allowing UV–blue photon harvesting without sacrificing band edge emission. This expansion in the harvesting range and narrow yet intense emission serves well for luminescent downshifting layers on crystalline silicon solar cells where capturing high energy photons while reducing self absorption losses is important for performance gain and long term stability [58].

3.9. TRPL

The TRPL decay curves of $CsPbBr_3$ and $CsPbBr_3@SiO_2$ quantum dots were fitted using a tri-exponential decay model as given in equation 1.

$$I(t) = A_1 e^{-t/\tau_1} + A_2 e^{-t/\tau_2} + A_3 e^{-t/\tau_3} \qquad 1$$

where τ_1, τ_2, and τ_3 correspond to the decay lifetimes for different recombination pathways and A_1, A_2, and A_3 their respective relative amplitudes. Such multi-component decay characteristic is generally attributed to the coexistence of fast trap-assisted recombination, intermediate surface-mediated recombination, and slow band-edge radiative recombination processes, which is common in perovskite quantum dots. The amplitude-weighted average PL lifetime was measured using the equation 2.

$$\tau_{ave} = \frac{A_1\tau_1 + A_2\tau_2 + A_3\tau_3}{A_1 + A_2 + A_3} \qquad 2$$

Also, the fractional contribution of each decay time to the steady state amplitude was calculated using the equation 3.

$$fi = \frac{A_i \tau_i}{A_1\tau_1 + A_2\tau_2 + A_3\tau_3} \qquad 3$$

Table 3-3: Lifetime decay calculations from TRPL fitting data of the solution phase (where f denotes fractional contribution)

	τ1 (ns)	**f1**	**τ2 (ns)**	**f2**	**τ3 (ns)**	**f3**	**Avg τ (ns)**
$CsPbBr_3$	0.99	0.05	14.18	0.29	80.01	0.66	12.4
Si-$CsPbBr_3$	1.11	0.04	13.97	0.30	65.59	0.66	14.5

Table 3-4: Lifetime decay calculations from TRPL fitting data of the thin film

	τ1 (ns)	**f1**	**τ2 (ns)**	**f2**	**τ3 (ns)**	**f3**	**Avg τ (ns)**
$CsPbBr_3$	7.17	0.07	37.96	0.43	172.18	0.51	42.0
Si-$CsPbBr_3$	0.01	0.00	9.78	0.12	84.07	0.88	35.9

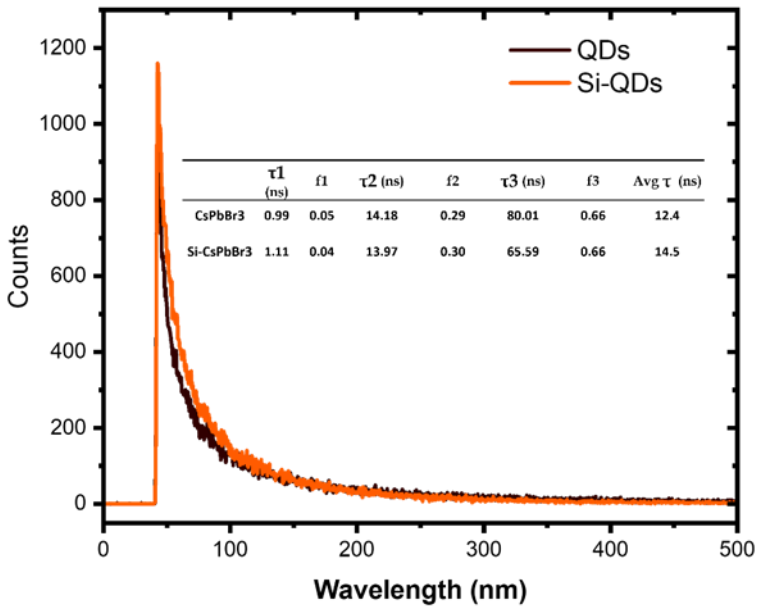

	τ1 (ns)	f1	τ2 (ns)	f2	τ3 (ns)	f3	Avg τ (ns)
CsPbBr3	0.99	0.05	14.18	0.29	80.01	0.66	12.4
Si-CsPbBr3	1.11	0.04	13.97	0.30	65.59	0.66	14.5

Figure 3-6: Time-resolved photoluminescence (TRPL) decay of $CsPbBr_3$ and $CsPbBr_3@SiO_2$ quantum dots in solution

Figure 3.6 shows the Time-resolved photoluminescence (TRPL) decay of $CsPbBr_3$ and $CsPbBr_3@SiO_2$ quantum dots in solution. TRPL decays of $CsPbBr_3$ QDs and silica modified $CsPbBr_3@SiO_2$ QDs were fitted using a tri-exponential model (See Supplementary TRPL section). The silica-modified $CsPbBr_3@SiO_2$ quantum dots exhibit a longer average photoluminescence lifetime (14.46 ns) compared with the bare $CsPbBr_3$ quantum dots (12.39 ns). The reduced contribution of the fastest component and the longer average lifetime are consistent with fewer ultrafast loss channels, matching the sharper PL and the higher PLQY observed after APTES-mediated silica treatment. Similar improvements in recombination dynamics upon organosilicon or silica based surface engineering have been reported for $CsPbBr_3$ nanocrystals, where passivation suppresses defect mediated losses while preserving the perovskite core structure, consistent with the XRD and HRTEM results [24], [51], [99].

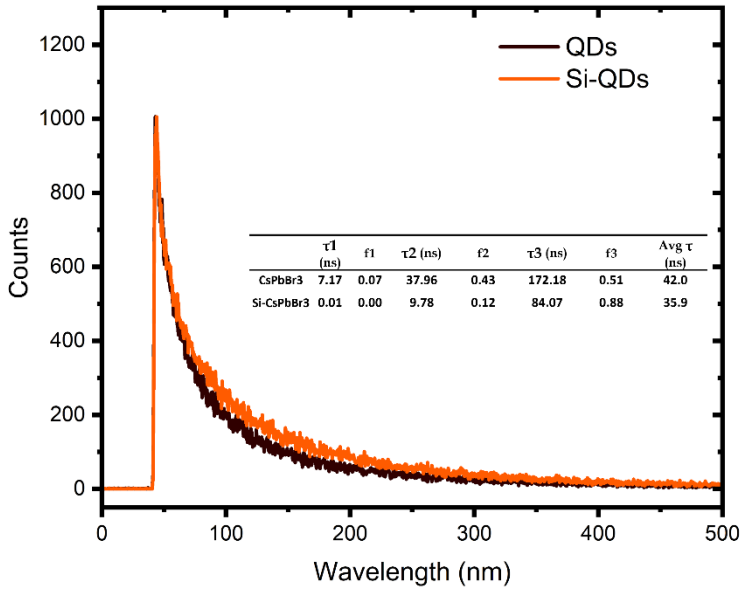

Figure 3-7: Time-resolved photoluminescence (TRPL) decay of $CsPbBr_3$ and $CsPbBr_3@SiO_2$ quantum dots in thin film

Figure 3.7 shows the Time-resolved photoluminescence (TRPL) decay of $CsPbBr_3$ and $CsPbBr_3@SiO_2$ quantum dots in thin films. In thin films, the average lifetime of the bare $CsPbBr_3$ film is 42.00 ns, while the silica-modified film exhibits an average lifetime of 35.93 ns. The shorter average lifetime observed for the modified film, combined with higher PLQY, suggests that the recombination process becomes more radiative in nature. This indicates that surface passivation suppresses nonradiative trap states while allowing faster band-edge emission. Although the average lifetime is slightly lower after silica modification, the decay is heavily dominated by a single long lived component (f3 finally reaches 0.88), showing a more uniform dominant recombination channel in thin film, which aligns with reduced defects and interfacial homogeneity due to the introduction of silica-rich interphase. Related trends were observed for oxide- or organosilicon-stabilized perovskite QD films, in which surface modifications rearrange decay distributions and enhances emission efficiency and operational robustness of solid state films [99], [116].

Overall, the TRPL component analysis reinforces the structure and steady state optical results presented earlier. To this end, XRD and TEM indicate that silica functionalization retains the crystalline nature of the $CsPbBr_3$ core whilst absorption, PL and PLQY suggest improved spectral conversion properties which are desired for luminescent down shifting. The TRPL data add the kinetic perspective, showing that silica modification suppresses the relative contribution of fast decay channels in solution and produces a film decay that is dominated by a longer-lived component. The redistribution of decay components indicates that silica modification alters the recombination dynamics by suppressing fast nonradiative channels and promoting a more uniform radiative

recombination pathway, supporting surface and interfacial passivation. The mechanism is consistent with literature on silane-engineered $CsPbBr_3$ nanocrystals and $CsPbBr_3$ based LDS coatings for crystalline silicon devices [104], [119].

3.10. Performance analysis as LDS layer on Si Solar cell.

3.10.1 PCE and Jsc of bare QDs and Si treated QDs

The performance analysis was done by taking IV curves and finding PCE and Jsc. Figure 3.8 compares the photovoltaic response of c-Si mini modules after coating with PMMA based LDS layers containing either bare $CsPbBr_3$ QDs (left) or silica modified $CsPbBr_3@SiO_2$ QDs (right), plotted as PCE and Jsc versus relative QD loading (0.50× to 1.50×) for four PMMA contents (5, 10, 15, 20 mg). For each formulation, each measurement was repeated four times, and statistical analysis is provided in the Supporting Information. For bare $CsPbBr_3$, the reference cell is at ∼14.5% PCE and 3.20 mA cm−2 Jsc. A distinct optimum can be observed at 1.0× QD loading, most notably for 15 mg PMMA (C), with PCE of 15.40% and Jsc of 3.29 mA cm−2, corresponding to +0.65% absolute PCE and +0.09 mA cm−2 compared to the reference. At the same 1.0× loading, 10 mg PMMA (B) and 5 mg PMMA (A) are slightly lower but still enhanced, ~15.22 to 15.25% PCE and ≈3.26 to 3.27 mA cm−2 Jsc; the thickest matrix, that of PMMA at 20 mg (D), shows the least gain of about 14.95% PCE and ≈3.23 mA cm−2 Jsc. This non-monotonic behavior is a well-known LDS trade-off given in the literature, as moderate QD density facilitates UV–blue photon harvesting and re-emission into the visible, resulting in higher Jsc and PCE while excessive loading results in greater parasitic absorption, reabsorption, and scattering losses that offset the down-shifting benefit [58], [109].

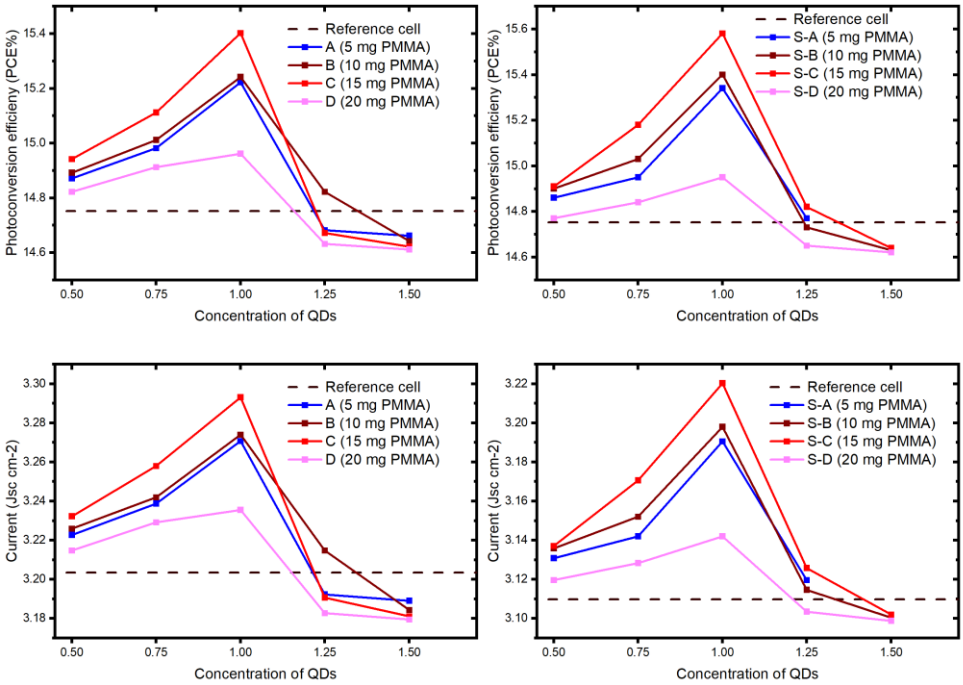

Figure 3-8: Photovoltaic performance of crystalline silicon mini-modules coated with PMMA-based LDS layers containing bare $CsPbBr_3$ or $CsPbBr_3@SiO_2$ quantum dots.

Figure 3.8 gives the photovoltaic performance of crystalline silicon mini-modules coated with PMMA-based LDS layers containing bare $CsPbBr_3$ or $CsPbBr_3@SiO_2$ quantum dots. $CsPbBr_3@SiO_2$ shows a similar optimization trend, but with generally higher gains, which indicates that the window of performance is enlarged when silica modification is implemented. The reference cell used in this case has (around 14.75% PCE and 3.11 mA cm−2 Jsc). For the $CsPbBr_3@SiO_2$, the loading formulations that perform again are 1.0×, 15 mg PMMA (S C), where PCE reaches about 15.58%, Jsc approaches approx. 3.22 mA cm−2 with +0.83% absolute PCE and +0.11 mA cm−2 Jsc as compared to the reference cell, respectively. At 1.0× Si-QD loading, 10 mg PMMAs (S B) and 5 mg PMMAs (S A) remain close to 15.40% and 15.33% PCE, with Jsc approaching around of +3.20 and +3.19 mA cm−2 accordingly while once more the 20 mg PMMA (S D) underperforms, near 14.94% PCE and 3.14 mA cm−2 output values respectively The enhanced peak for $CsPbBr_3$ $@SiO_2$ is consistent with the earlier optical data, silica treated QDs exhibit sharper and stronger PL and higher PLQY implying that more of the absorbed UV–blue photons becomes useful in visible scale as opposed to non radiative losses. Higher PLQY increases the probability that absorbed UV-blue photons are re-emitted as visible photons that can contribute to silicon photocurrent. Silane-mediated interface engineering has been reported to improve $CsPbBr_3$ based LDS films' optical performance, by providing reduced defect-mediated quenching and improved optical stability of the emissive layer,

which translates here into higher Jsc and PCE for solar cell performance, especially near an optimal film thickness and QD loading [113], [120]. At higher loading (1.25× to 1.50×), both systems drop toward or below the reference, for example PCE falls back to about 14.62 to 14.70% and Jsc to about 3.10 to 3.13 mA cm−2 for the Si QD series, which is consistent with the well known onset of concentration quenching, photon reabsorption, and increased optical losses in thicker or more heavily loaded LDS coatings [121], [122].

3.10.2 IV Curves

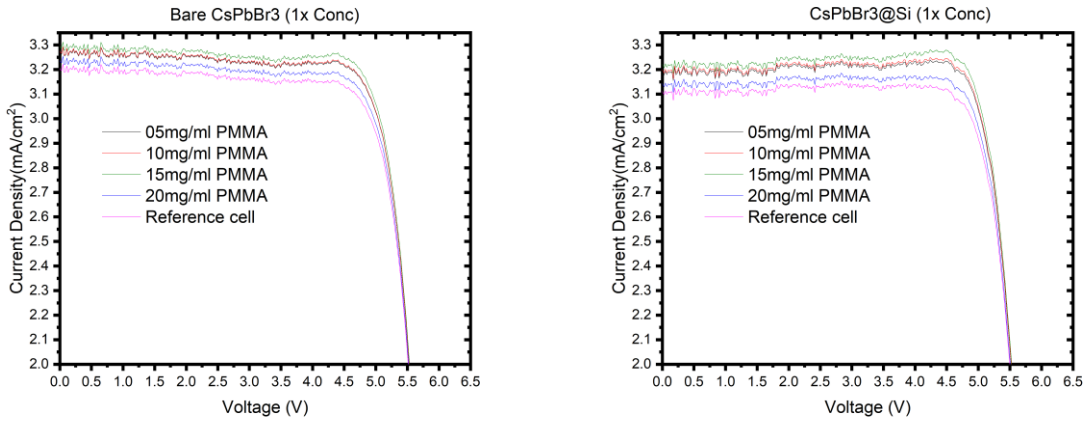

Figure 3-9: Current density–voltage (J–V) characteristics of silicon mini-modules coated with PMMA-based LDS layers containing $CsPbBr_3$ and $CsPbBr_3$@SiO_2 quantum dots.

Figure 3.9 shows the current density–voltage (J–V) characteristics of crystalline silicon mini modules with PMMA based luminescent down-shifting layers loaded with either bare $CsPbBr_3$ QDs or silica modified $CsPbBr_3$@SiO_2 QDs at a constant QD loading of 1× and various PMMA concentrations. Both cases exhibit J–V curves with similar open circuit voltage and fill factor to that of the reference cell, suggesting that the LDS coatings result in no adverse effects to the electrical junction or additional series resistance. The primary change is observed in the short circuit region, where cells coated with bare QDs LDS layers show a systematic increase in current density across the entire voltage range, consistent with enhanced photogenerated carrier density rather than electrical modification of the device. Moreover, the Si-QDs coated cells exhibit a slightly higher current density than their bare QDs counterparts, particularly for the 15 mg mL−1 PMMA formulation, in agreement with the PCE and Jsc trends discussed earlier. This improvement reflects more efficient down shifting of UV–blue photons into the visible region due to the higher PLQY and improved optical stability of the silica-modified QDs. As the J–V curve shape remains the same and there is no sign of Voc loss, confirms that performance enhancement is contributed by optical spectral management rather than changes in charge transport or recombination within the silicon device. This performance is consistent

with previous reports on $CsPbBr_3$-based luminescent down shifting layers integrated with crystalline silicon solar cells.

3.10.3 Relative PCE % Performance

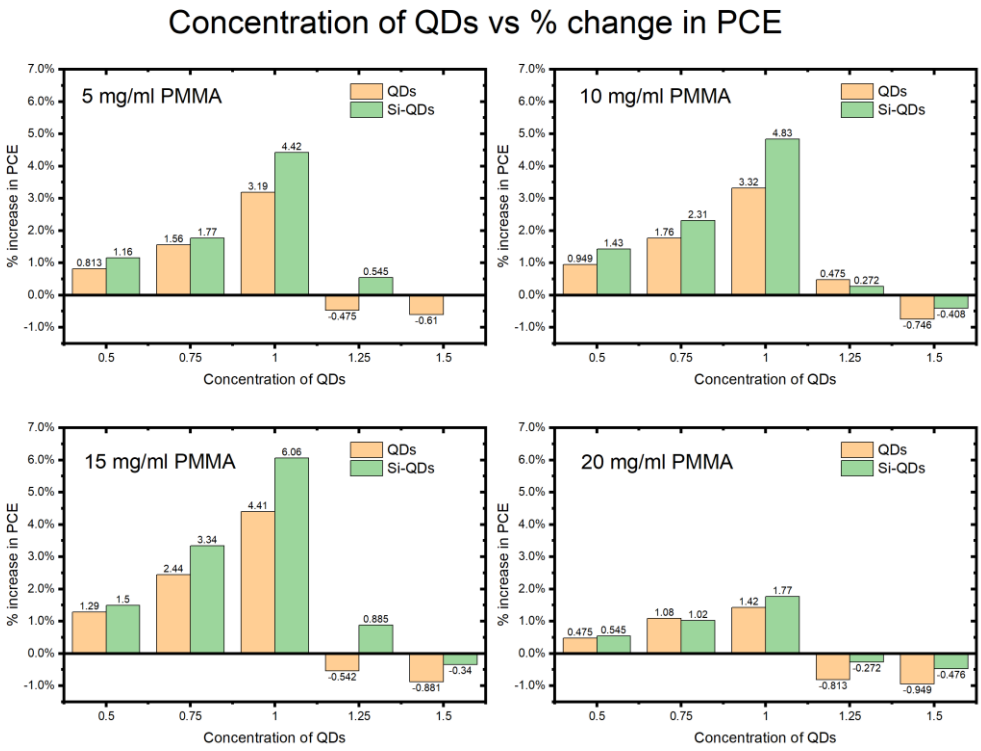

Figure 3-10: Relative enhancement in power conversion efficiency for different LDS formulations.

Figure 3.10 summarizes the relative percentage change in power conversion efficiency (PCE) for different formulations of either bare $CsPbBr_3$ QDs or silica-modified $CsPbBr_3$@SiO_2 QDs as a function of QD concentration and PMMA content. Across all PMMA loadings, both systems exhibit a clear optimum at **1.0× QD concentration**, confirming that LDS performance is governed by a balance between photon conversion and optical losses. For bare $CsPbBr_3$, the maximum PCE enhancement reaches **4.4%**, depending on PMMA content, whereas the corresponding $CsPbBr_3$@SiO_2 layers give higher gains consistently ranging between **≈4.4–6.1%**. The largest gain is observed for **15 mg mL^{-1} PMMA**, where the PCE enhancement reaches **≈6%**. At lower QD loadings (0.5×–0.75×), the PCE enhancement remains positive but smaller, reflecting lesser utilization of UV–blue photons, whereas at higher loadings (≥1.25×) the relative PCE change becomes negligible or negative. This is mainly due to increased parasitic absorption, reabsorption of emitted photons, and scattering losses within thicker LDS layers. The systematically higher percentage gains achieved with $CsPbBr_3$@SiO_2 across all PMMA concentrations are in correlation with its sharper photoluminescence, higher PLQY, and improved recombination characteristics

discussed earlier. This enables more efficient photon downshifting at lower effective QD densities. These trends are fully consistent with reported optimization studies on perovskite quantum dot-based LDS coatings for crystalline silicon solar cells, where surface-engineered nanocrystals exhibit broader processing tolerance and higher efficiency enhancement compared to unmodified QDs [97], [123], [124].

3.11. Conclusion

Here, we show a luminescent down-shifting coating of APTES-functionalized $CsPbBr_3$ quantum dots embedded in a PMMA matrix for crystalline silicon solar cells. Our structural analyses indicate that the silane-induced modifications lead to the formation of an amorphous, silica-rich interphase surrounding the nanocrystals while retaining their intrinsic perovskite-like lattice. This interfacial passivation reduces surface defects, leading to a sharper emission profile, higher photoluminescence quantum yield, and better recombination dynamics of the $CsPbBr_3$ quantum dots compared to those in the bare state.

The modified nanocrystals embedded in PMMA showed efficient absorption of ultraviolet and blue photons, with re-emission in the visible region, matching the spectral response of the silicon absorber layer. Consequently, allowing the luminescent down-shifting layers to enhance short-circuit current density without impacting the electronic properties of the underlying device, proving an optical origin for performance enhancement. The improved formulation achieves an absolute efficiency gain of 0.83% with sustained relative gains approximately 6%.

While external quantum efficiency measurements and long-term stability testing would provide additional insight into the LDS mechanism and durability of the coatings, the present study focuses on demonstrating the feasibility of APTES-modified $CsPbBr_3$ quantum dots embedded in PMMA as luminescent down-shifting layers for silicon solar cells. These results show that a combination of LARP synthesis with APTES-mediated surface engineering and PMMA encapsulation yields a straightforward and scalable route to stabilize perovskite quantum dots for use as spectral converters in silicon.

Overall, this chapter establishes PMMA-integrated, surface-modified $CsPbBr_3$ quantum dots as a promising LDS-oriented coating platform for silicon photovoltaics, particularly because the observed gains are moderate, composition-dependent, and physically plausible. However, full mechanistic separation of luminescent conversion from antireflection, scattering, and other optical effects would require wavelength-resolved EQE measurements, film-state PLQY analysis, and more complete optical accounting. In addition, long-term durability under module-relevant thermal, ultraviolet, and humidity stress remains necessary before the approach can be assessed for practical deployment.

Accordingly, the present work should be regarded as a strong proof-of-concept for passivation-assisted LDS coatings rather than a fully closed demonstration of module-ready spectral conversion technology.

Chapter.4 Plasmon-Assisted Photoluminescence Enhancement in CdSe/CdS Quantum-Dot Films Coupled with Gold Nanoparticles

Chapter 3 demonstrated that the optical performance of quantum-dot based spectral-conversion layers can be improved through chemical and interfacial engineering, particularly by suppressing defect-mediated nonradiative recombination and preserving photoluminescence in a device-relevant film. However, the performance of a luminescent material is not determined solely by its intrinsic composition or surface passivation. It also depends on the electromagnetic environment surrounding the emitter. In this context, plasmonic nanostructures offer an additional route for manipulating quantum-dot emission through localized surface plasmon resonance (LSPR), which can alter excitation efficiency, radiative decay behavior, and emission intensity [125], [126].

Although plasmon-assisted photoluminescence enhancement has been widely reported, the literature remains less resolved than is often implied. Enhancement is frequently presented as a general consequence of coupling quantum dots with metallic nanoparticles, whereas in practice the outcome is governed by a sensitive competition among local field enhancement, radiative-rate modification, and nonradiative energy transfer to the metal [127], [128]. As a result, plasmonic coupling does not automatically improve emission. At very small separations, quenching often dominates, whereas at intermediate distances enhancement may emerge only within a narrow structural window [129], [130]. Thus, the central issue is no longer whether plasmonic enhancement is possible in principle, but whether it can be engineered reproducibly in a morphology-controlled and physically interpretable manner.

4.1. Background

Plasmonic nanostructures have been extensively investigated as a means of modifying light-matter interactions at the nanoscale. When metallic nanoparticles support localized surface plasmon resonance, the confined electromagnetic fields generated near their surfaces can increase the excitation rate of nearby emitters and, under suitable conditions, alter their radiative decay dynamics [131], [132]. In quantum-dot systems, these effects are commonly discussed within the broader framework of metal-enhanced fluorescence or plasmon-enhanced photoluminescence. The magnitude and even the sign of the response, however, depend on several coupled factors, including the type of metal, nanoparticle morphology, spectral overlap, excitation wavelength, and emitter-metal separation [129], [130]. Consequently, plasmonic enhancement is intrinsically a geometry-dependent phenomenon rather than a universal property of metal-quantum-dot composites.

Among quantum emitters, CdSe/CdS core-shell quantum dots remain attractive model systems because they combine high photoluminescence efficiency, spectral tunability, and improved stability

relative to bare-core nanocrystals [133], [134]. The CdSe core provides efficient absorption of high-energy photons, while the CdS shell suppresses surface-related nonradiative recombination and supports stronger emission [135]. Their visible-range emission and good optical quality have therefore made them relevant not only for general optoelectronic applications, but also for ultraviolet down-shifting and related photon-management concepts in photovoltaics [126]. Nevertheless, even these core-shell structures remain limited by incomplete excitation efficiency and residual nonradiative losses, which motivates investigation of external optical coupling strategies capable of further increasing emission output.

Gold nanoparticles are among the most widely used plasmonic materials for this purpose because they exhibit stable and tunable LSPR in the visible region. Their interaction with nearby quantum dots may enhance photoluminescence through near-field amplification or radiative-rate modification, but only when the structure is designed within a suitable spectral and spatial regime [136], [137]. The literature consistently shows that emitter-metal spacing is a decisive control parameter. Very short distances generally favor nonradiative energy transfer and quenching, whereas intermediate separations can produce net enhancement. At larger distances, the plasmonic effect decays and the coupling becomes negligible [138], [139]. Spacer layers such as PMMA or SiO_2 are therefore commonly introduced to regulate separation and to shift the system away from the quenching regime [126], [140]. In addition, nanoparticle size distribution and surface coverage strongly influence the local optical response, because morphology determines resonance position, field localization, and the balance between enhancement and parasitic loss.

Despite this broad understanding, much of the existing literature has relied on colloidal synthesis routes for gold nanoparticle preparation. While such approaches are useful for proof-of-concept demonstrations, they often provide less control over nanoparticle morphology, spatial uniformity, and reproducibility, all of which are critical parameters for reliable plasmonic coupling [28], [141]. In contrast, magnetron sputtering offers a scalable physical deposition route with improved control over particle size, density, and distribution, and is compatible with a wider range of substrates. Recent studies have shown that sputtering conditions can strongly affect nanoparticle morphology and optical response, making this method particularly suitable for constructing plasmonically coupled hybrid films in a more controlled manner [142], [143]. Yet, despite these advantages, the use of magnetron-sputtered Au nanoparticles for enhancing the photoluminescence of CdSe/CdS core-shell quantum-dot films has remained insufficiently explored.

4.2. Problem Statement

Despite the well-known ability of gold nanoparticles to enhance the photoluminescence of nearby quantum emitters, most reported studies have been based on colloidal AuNP synthesis, which often

limits reproducibility and precise control over nanoparticle morphology and distribution. As a result, the relationship between nanoparticle structure, emitter-metal separation, and optical response remains insufficiently resolved, particularly for CdSe/CdS core-shell quantum dot systems. Moreover, the use of magnetron-sputtered AuNPs as a controlled and scalable platform for photoluminescence enhancement in CdSe/CdS films has not been previously established. This highlights the need for a systematic investigation in which AuNP morphology and spacer-layer thickness are deliberately controlled in order to determine the design conditions that maximize enhancement while minimizing plasmon-induced quenching. Scientifically, the chapter is distinct in treating plasmonic coupling not as a purely phenomenological effect, but as a structure-dependent optical problem in which nanoparticle morphology and separation distance are systematically engineered and evaluated. In this way, the chapter contributes a more controlled route toward plasmonically enhanced quantum-dot emission, with relevance to future optical down-shifting and light-management layers for photovoltaic applications.

4.3. Experimental Procedure

4.3.1 Materials

All chemicals were purchased from Sigma-Aldrich unless otherwise specified and were used as received without further purification. The reagents employed in the synthesis of CdSe/CdS core-shell quantum dots included cadmium oxide (CdO, 99.5%), cadmium acetate dihydrate (>98%), selenium powder (99.5+%), sulfur powder (>99%), oleic acid (OA, 90%), 1-octadecene (ODE, 90%), and trioctylphosphine (TOP, 90%).

4.3.2 Synthesis of CdSe Quantum Dots

CdSe quantum dots were synthesized by a hot-injection method under inert atmosphere. A selenium precursor was first prepared by mixing selenium powder (28.5 mg, 0.360 mmol) with TOP (0.2 mL) and ODE (1.5 mL). The mixture was stirred at 50 °C for 20 min under argon until a clear transparent solution was obtained.

In parallel, cadmium oxide (71 mg, 0.390 mmol), ODE (10 mL), and OA (1 mL) were loaded into a three-neck flask. The reaction mixture was degassed on a Schlenk line and then heated to 280 °C under argon for 20 min until complete dissolution of the cadmium precursor was achieved. The selenium precursor was then rapidly injected into the cadmium precursor solution, after which the reaction temperature was immediately reduced to 250 °C and maintained for 10 s to allow controlled growth of the CdSe nanocrystals. The reaction was subsequently quenched to room temperature.

The resulting CdSe quantum dots were purified twice by precipitation with methanol using a 1:3 volume ratio, followed by centrifugation at 4000 rpm. The purified nanocrystals were finally redispersed in octadecene for further processing.

4.3.3 Growth of CdSe/CdS Core-Shell Quantum Dots

4.3.3.1. Preparation of shell precursors

For the cadmium precursor, cadmium acetate dihydrate (54 mg, 0.2 mmol) and OA (0.3 mL, 1 mmol) were added to 4.6 mL of ODE and heated to 220 °C under stirring in an inert atmosphere for 10 min. For the sulfur precursor, sulfur powder (15.8 mg, 0.2 mmol) and TOP (0.1 mL, 0.4 mmol) were added to 4 mL of ODE and heated to 70 °C under inert atmosphere until a clear solution was obtained. Both precursor solutions were then cooled to room temperature and stored for subsequent shell growth.

4.3.3.2. CdS shell growth

The CdS shell was grown around the preformed CdSe cores by a one-pot shelling method. In a typical procedure, 9 mL of ODE, CdSe cores (0.04 mmol), and the calculated amounts of cadmium and sulfur precursor solutions were introduced into a three-neck flask under inert atmosphere. The reaction mixture was then heated gradually to 200 °C and maintained at this temperature for 1 h. This temperature was selected to promote heterogeneous shell growth while minimizing homogeneous nucleation of CdS. After completion of the shell-growth step, the reaction mixture was cooled slowly to room temperature.

The CdSe/CdS core-shell quantum dots were purified with methanol, collected by centrifugation at 4000 rpm, and finally dispersed in hexane for subsequent use.

4.4. Fabrication of AuNPs/QD Coupling Structures

To investigate plasmon-enhanced photoluminescence of CdSe/CdS quantum dots, a multilayer coupling architecture was fabricated consisting of Au nanoparticles deposited on a glass substrate, followed by a PMMA spacer layer, and a top emissive layer of CdSe/CdS quantum dots dispersed in PMMA. PMMA was used as a dielectric spacer to control the QD-AuNP separation, reducing metal-induced quenching while allowing plasmonic interaction at intermediate distances. A schematic representation of this structure is shown in Figure 4.1.

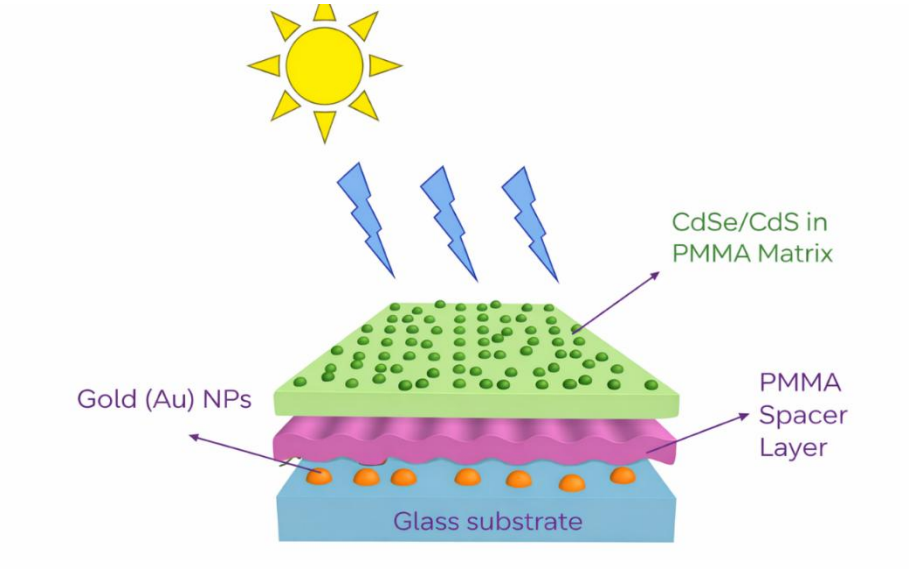

Figure 4-1: Hybrid plasmonic structure consisting of a CdSe/CdS quantum-dot PMMA layer, a PMMA spacer, and Au nanoparticles deposited on a glass substrate

Glass substrates were first cleaned with ethanol and acetone. Gold nanoparticles were then deposited by magnetron sputtering. Prior to Au deposition, the glass substrates were carbon-coated using the pulsed carbon rod program of a Quorum Q150T ES Plus sputter coater. Subsequently, Au nanoparticles were prepared on the carbon-coated glass using an Emitech K550X sputter coater operated at a current of 10 mA for 10 s. The sputtering process was conducted in an argon atmosphere at a pressure of approximately 10^{-1} mbar.

Following AuNP deposition, a PMMA spacer layer was introduced by spin coating at 3000 rpm for 60 s. The spacer thickness was controlled by varying the concentration of PMMA dissolved in toluene. PMMA concentrations of 0.05, 0.075, 0.1, 0.3, 0.5, 0.7, 0.85, and 1.0 wt% were used, corresponding to thickness values in the range of approximately 3 to 51 nm. As a spacer layer, PMMA controls the QD-AuNP distance, whereas in the emissive layer, PMMA acts as a host matrix to disperse CdSe/CdS QDs and form a uniform luminescent film. The thickness-concentration relationship is presented in Figure 4.2. The preparation strategy for the PMMA spacer layer followed the method reported by Song et al. [137] for reproducing controlled spacer thicknesses.

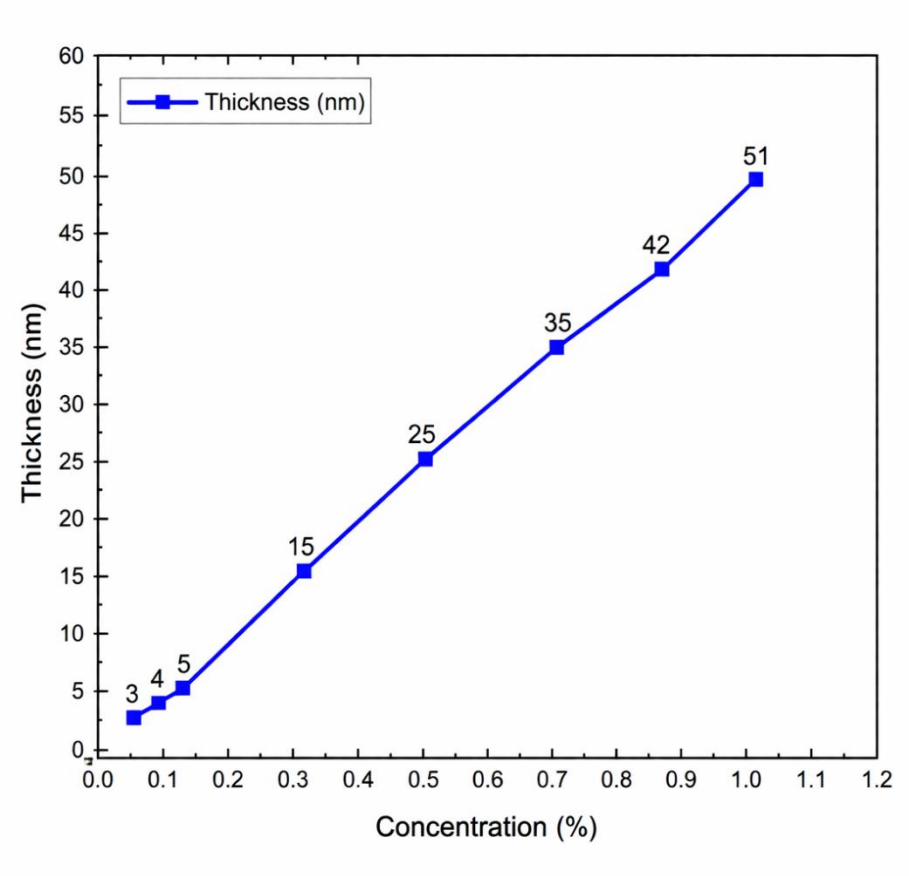

Figure 4-2: Variation of PMMA spacer-layer thickness as a function of PMMA concentration

For deposition of the top emissive layer, 1 mL of the previously prepared CdSe/CdS quantum-dot solution in toluene was mixed with 1 mL of 1.0 wt % PMMA in toluene. The resulting mixture was then spin-coated onto the PMMA spacer layer at 3000 rpm for 60 s to form the QD-containing top film. For each coupling configuration, five independently prepared samples were fabricated to ensure reproducibility.

4.5. Optical Characterization

The photoluminescence spectra of the quantum dots were recorded using an Optica PL spectrometer. Absorption spectra were measured using a Cary 60 UV-Vis spectrometer. The PL spectra of the AuNP/QD coupling structures were acquired using a Renishaw inVia confocal Raman microscope equipped with an external ultraviolet LED source in place of the standard laser. The excitation wavelength of the LED source was 375 nm, with an approximate spectral variation of ±10 nm.

Measurements were performed using a 2400 lines mm^{-1} diffractive grating, and the spectra were collected with a 576-pixel CCD detector. The UV excitation source was positioned at a fixed distance of 10 cm from the sample and maintained at a constant angle throughout all measurements. A 100× objective lens was used to collect the emitted PL signal. All optical measurements were conducted in

a dark room at room temperature in order to minimize interference from ambient light and maintain consistent experimental conditions.

4.6. Results and Discussion

4.6.1 Morphology and size distribution of sputter-deposited Au nanoparticles

To characterize the morphology of the deposited Au nanoparticles, AuNPs, scanning electron microscopy, SEM, was employed. The samples were examined using a Zeiss Gemini 300 scanning electron microscope operated at an accelerating voltage of 5 kV and a working distance of 5 mm. Imaging was performed by collecting both secondary electron signals with the InLens detector and backscattered electron signals with the external BSD detector, thereby enabling reliable assessment of nanoparticle morphology and surface distribution.

To establish a morphological reference for the deposited AuNP layer, a bare glass substrate was first coated with carbon prior to SEM imaging, as shown in Figure 4.3. This conductive coating was introduced solely to facilitate electron imaging of the otherwise poorly detectable glass surface under the selected SEM conditions. It should be emphasized that the samples used for photoluminescence measurements were not carbon-coated, in order to avoid any possible interference of the conductive layer with the optical response of the AuNP/QD coupling structure.

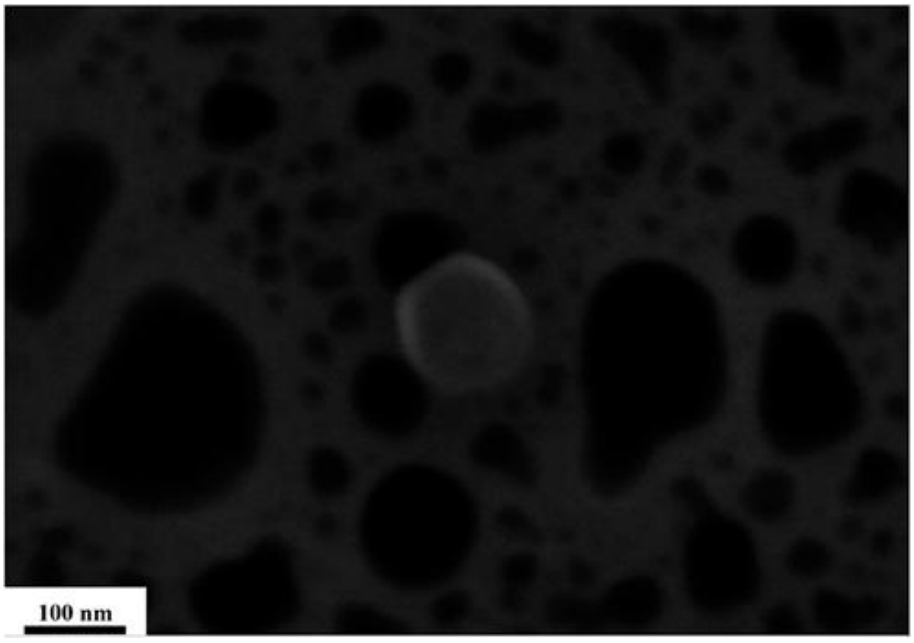

Figure 4-3:SEM image of a bare glass substrate coated with carbon

The SEM micrograph shown in Figure 4.4 reveals the formation of bright, predominantly spherical AuNPs dispersed over the glass substrate with minimal aggregation. The particles appear spatially well distributed, with only limited clustering or coalescence. Such a morphology is advantageous for plasmonic applications because excessive agglomeration can broaden the localized surface plasmon

resonance, LSPR, band, reduce uniformity of the local electromagnetic field, and complicate interpretation of the distance-dependent photoluminescence response. The observed nanoparticle distribution therefore indicates that the sputtering conditions employed in this study are appropriate for producing a comparatively homogeneous plasmonic layer.

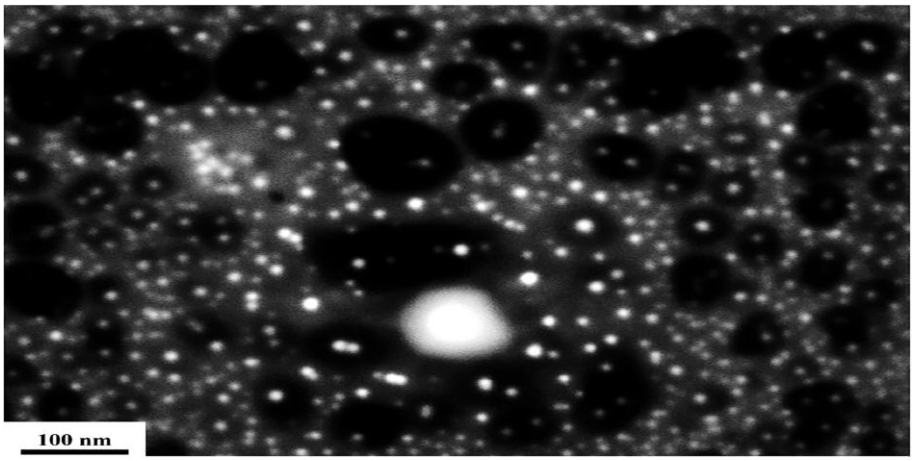

Figure 4-4: SEM image of Au Nanoparticles on a glass substrate

To quantify the particle dimensions, the SEM images were analyzed using ImageJ software. The corresponding size distribution is presented in Figure 4.5. The AuNPs exhibit a relatively narrow diameter distribution in the range of approximately 6 to 18 nm, with an average particle size of 11.1 nm. The majority of the particles fall within the 9 to 12 nm interval, indicating a fairly uniform nanoparticle population. This narrow distribution is of particular significance because the plasmonic response of metallic nanoparticles is strongly dependent on particle size, shape, and spatial arrangement. Accordingly, the relatively uniform morphology observed here is expected to support a more consistent LSPR response and, consequently, a more reproducible plasmon-mediated enhancement of quantum-dot photoluminescence [140].

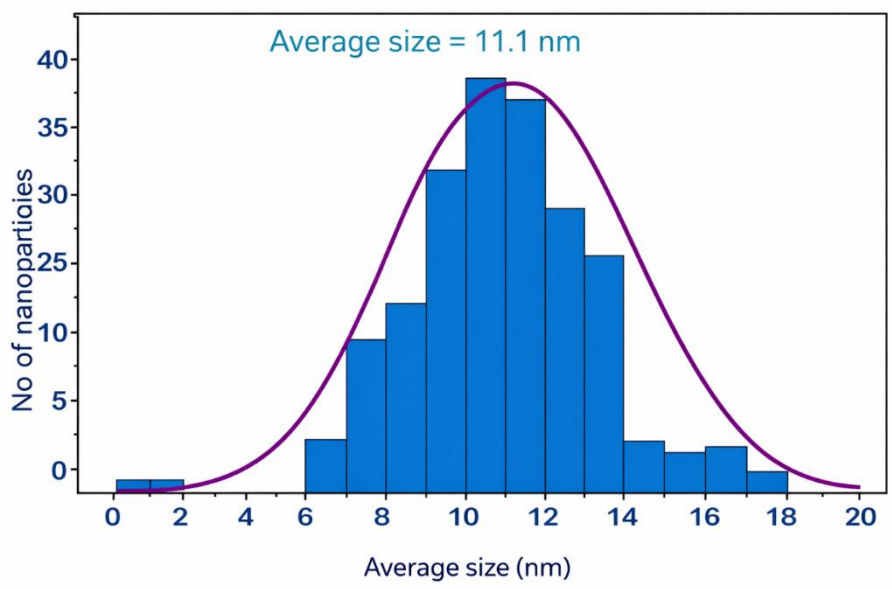

Figure 4-5: Size Distribution plot of AuNPs

4.6.2 Optical characteristics of AuNPs and CdSe/CdS quantum dots

The optical properties of the AuNPs were then examined to confirm the formation of an optically active plasmonic layer. As shown in Figure 4.6, AuNPs deposited at 10 mA for sputtering times ranging from 10 to 50 s exhibit clear plasmonic absorption bands in the visible region, extending approximately from 520 to 595 nm. The absorption intensity increases with deposition time, confirming progressive nanoparticle formation and consistent control over the optical response of the metallic layer. This visible-region resonance is characteristic of Au nanostructures within this size regime and confirms that the sputtered films are suitable for LSPR-based coupling [140], [144].

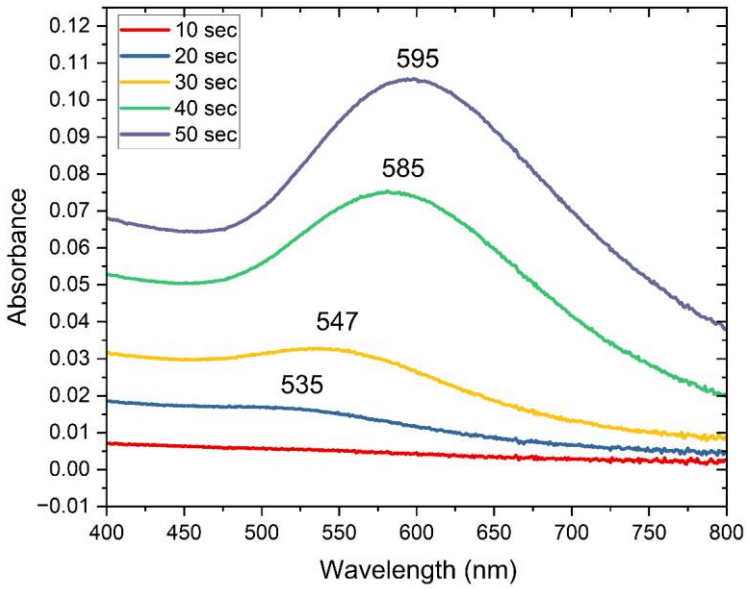

Figure 4-6: Absorption Spectra of Au Nanoparticles

The optical properties of the semiconductor emitters were evaluated next. Figure 4.7 shows that the CdSe core quantum dots display an absorption peak at 515 nm, corresponding to an estimated core diameter of approximately 2.6 nm [145]. After CdS shell growth by the SILAR method, the final CdSe/CdS core-shell size was estimated to be approximately 3.3 nm. Shell growth is important because it improves optical stability and suppresses surface-related nonradiative losses, thereby making CdSe/CdS an appropriate model emitter for plasmonic enhancement studies.

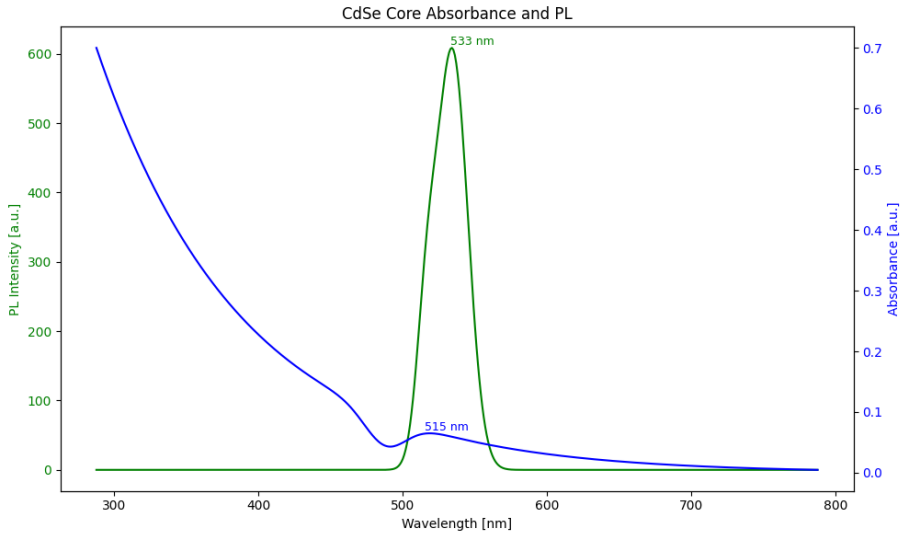

Figure 4-7: Absorption and Photoluminescence spectra of CdSe core

The absorption and PL spectra of the CdSe/CdS core-shell QDs are presented in Figure 4.8. The QDs show strong absorption in the ultraviolet region together with a pronounced visible PL emission band centered near visible region.

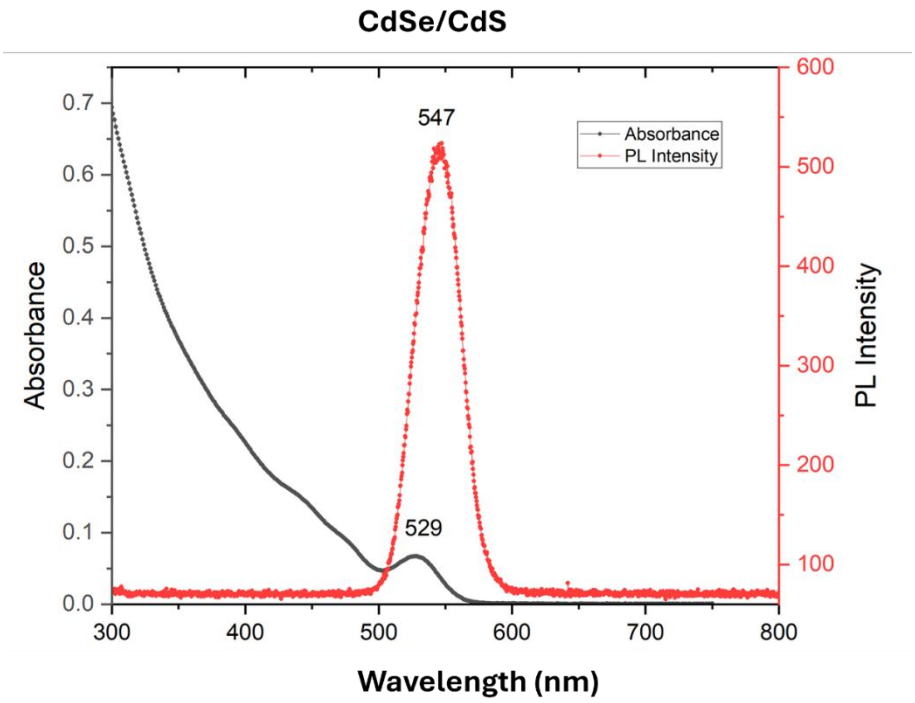

Figure 4-8: Absorption and Photoluminescence spectra of CdSe-CdS core-shell

This spectral configuration is relevant for two reasons. First, the strong UV absorption makes the QDs suitable for ultraviolet down-shifting concepts. Second, the visible emission lies in the spectral vicinity of the AuNP plasmon band, which is favorable for plasmon-mediated modification of the emission process. However, the system does not represent ideal resonance matching at the excitation wavelength because the excitation source is centered at 375 nm, whereas the main AuNP plasmon feature is centered closer to 585 nm. Since the excitation wavelength and main AuNP plasmon band are not perfectly matched, the enhancement is expected to be moderate rather than strongly resonant. This spectral mismatch limits purely resonant energy transfer and explains why the enhancement is measurable but not multifold. Instead, the observed PL increase is attributed primarily to local electromagnetic field enhancement and modified excitation conditions rather than to ideal resonant excitation of the metal nanostructures [146].

This point is scientifically important. In many plasmonic enhancement studies, strong PL amplification is reported when the excitation, plasmon resonance, and QD emission are more closely aligned. In the present system, the AuNPs still absorb into the UV-visible region despite their visible plasmon maximum, allowing measurable PL enhancement even under 375 nm excitation. This makes the present architecture relevant to UV-responsive optical applications, including prospective down-shifting layers, even if the absolute enhancement remains more moderate than that reported for highly resonant hotspot-dominated plasmonic systems [147].

4.6.3 Preprocessing and normalization of PL spectra

To extract a physically meaningful measure of PL enhancement, the raw spectra were preprocessed prior to comparison. As shown in Figure 4.9, each spectrum contains two distinct features, a smaller excitation-related peak near 375 nm and a larger QD emission peak around 547 nm. The baseline was subtracted and the two contributions were fitted separately using Fityk. The QD emission was fitted with a pseudo-Voigt function, appropriate for broadened semiconductor nanocrystal emission, whereas the excitation feature was fitted with a log-normal function, suitable for narrower asymmetric peaks. The representative fit shown in Figure 4.9 yields $R^2 = 1.0$ (Baseline vs Fitted) and $R^2 = 0.96$ (Raw vs Baseline), indicating excellent agreement between the selected fitting functions and the measured spectral features.

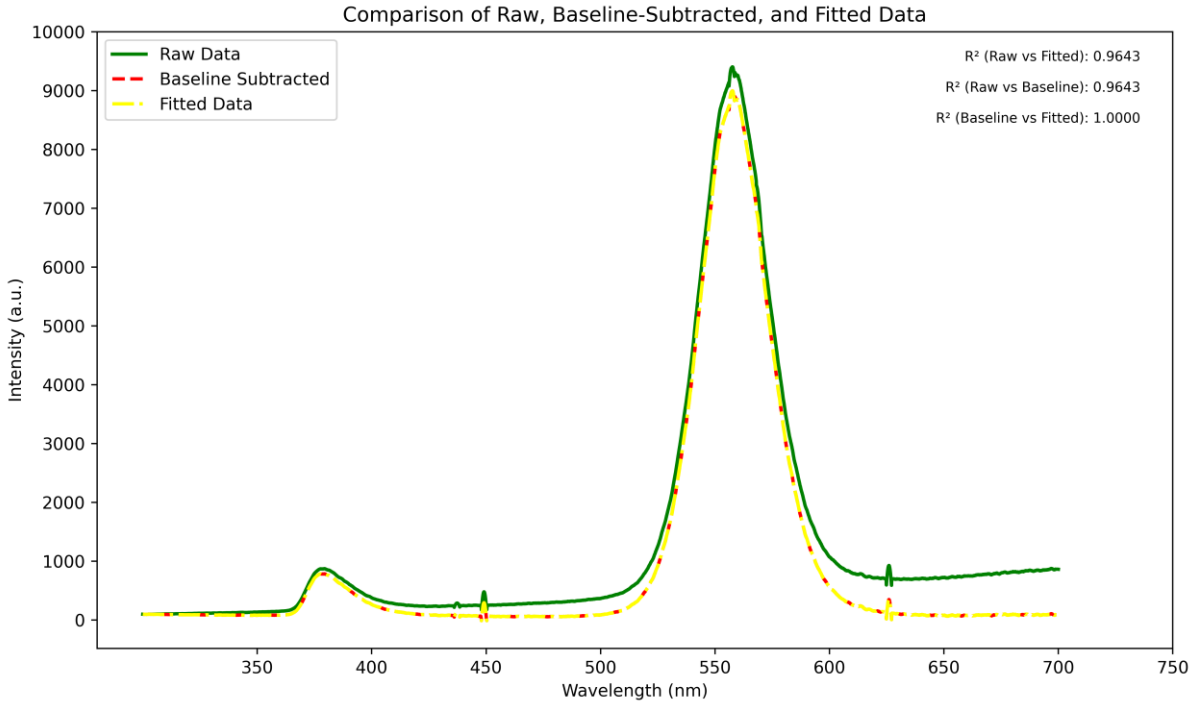

Figure 4-9: Data Fitting of QDs Photoluminescence

The raw spectra were additionally smoothed using a Savitzky-Golay filter, as shown in Figure 4.10, to suppress measurement noise. However, raw or smoothed PL intensity alone does not provide a sufficiently reliable measure of plasmonic enhancement, because apparent intensity changes may also be influenced by excitation scattering and geometry-dependent collection effects. For this reason, the analysis was normalized by taking the ratio of the integrated area of the QD emission peak to that of the excitation-related peak. This ratio-based metric does not represent an absolute PL quantum yield, but it provides a more robust basis for comparing relative PL enhancement across different coupling configurations.

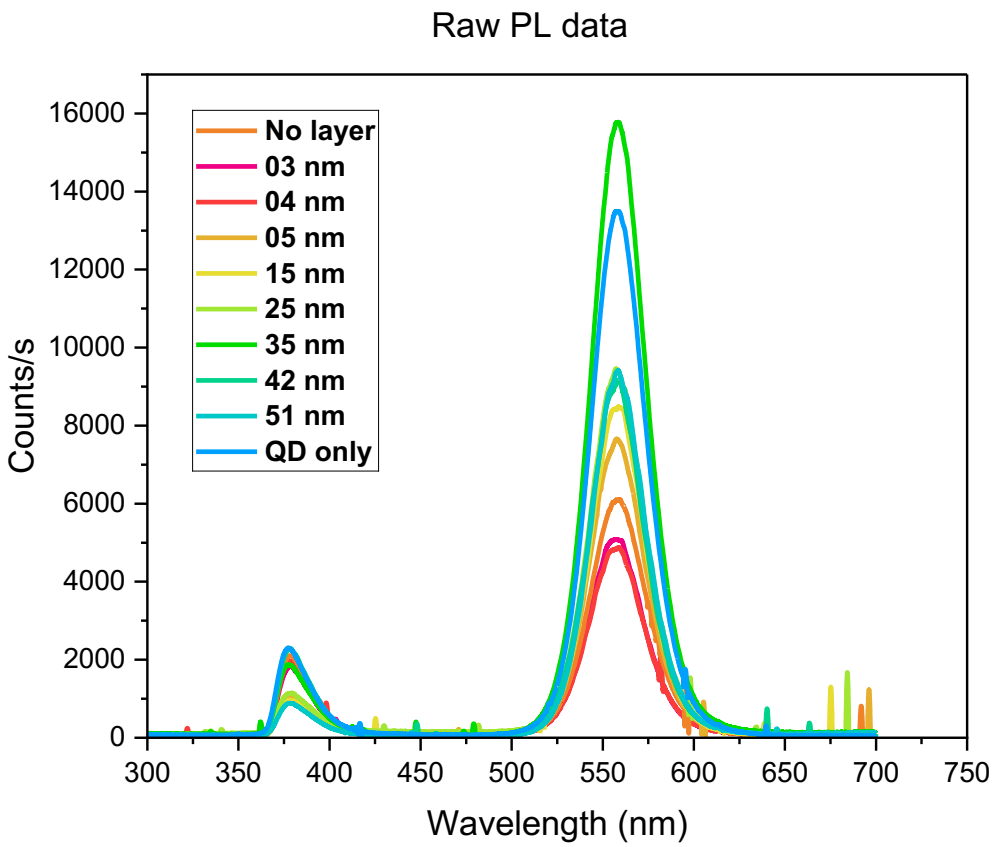

Figure 4-10: Raw PL data of QDs smoothed with Savitzky-Golay filter

The rationale for normalization is supported by the raw data presented in Figures 4.10 and 4.11. Figure 4.11 (left) shows no simple one-to-one correspondence between the height of the excitation-related peak and the geometry of the coupled structure. If scattering from the excitation source were dominating the optical response, a clearer geometric dependence of that peak would be expected. The absence of such a direct relation supports the use of normalized peak-area ratios to isolate changes more closely associated with emitter-metal coupling.

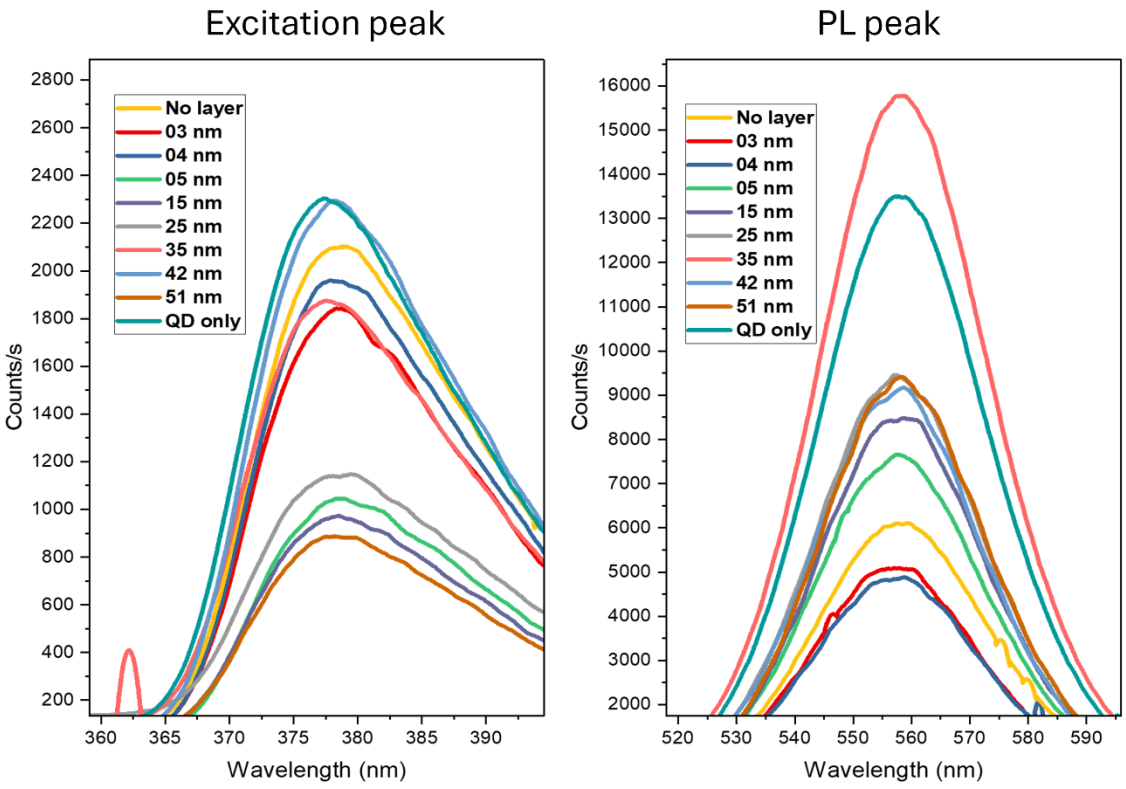

Figure 4-11: Excitation and Photoluminescence Peak of Plasmonic Coupling Structure

The representative example listed in Table 4.1 further illustrates this normalization procedure. Integrated peak area was preferred over peak height because it is less sensitive to local noise, small spectral shifts, and peak broadening, thereby providing a more stable comparison of PL response. For the sample with a nominal 15 nm PMMA spacer, the integrated area of the excitation peak is 20,653.6, whereas the area of the QD emission peak is 366,322, yielding an area ratio of 17.43. This value falls within the enhancement regime and is consistent with the broader trend later summarized in the box-plot analysis.

Table 4-1: Area under the Curves and Its Ratio

Sample name	**peak of excitation source (area under the curve) (function: log normal)**	**peak of QDs emission (area under the curve) (function: Lorentzian)**	**area ratio**
sample (a)*, 15 nm thickness	20,653.6	366,322	17.43

*This refers to a specific sample with 15 nm thickness.

4.6.4 Spacer-thickness-dependent PL response

The principal result of this chapter is the strong dependence of normalized PL on PMMA spacer thickness. The raw spectra for the different coupling geometries are shown in Figures 4.10 and 4.11, while the summary of the normalized responses from five independently prepared samples for each configuration is presented in the box plots of Figure 4.12. Together, these figures show that the PL response is non-monotonic with separation distance and can be divided into three distinct regimes, quenching at very short distances, enhancement at intermediate distances, and decay of enhancement at larger separations.

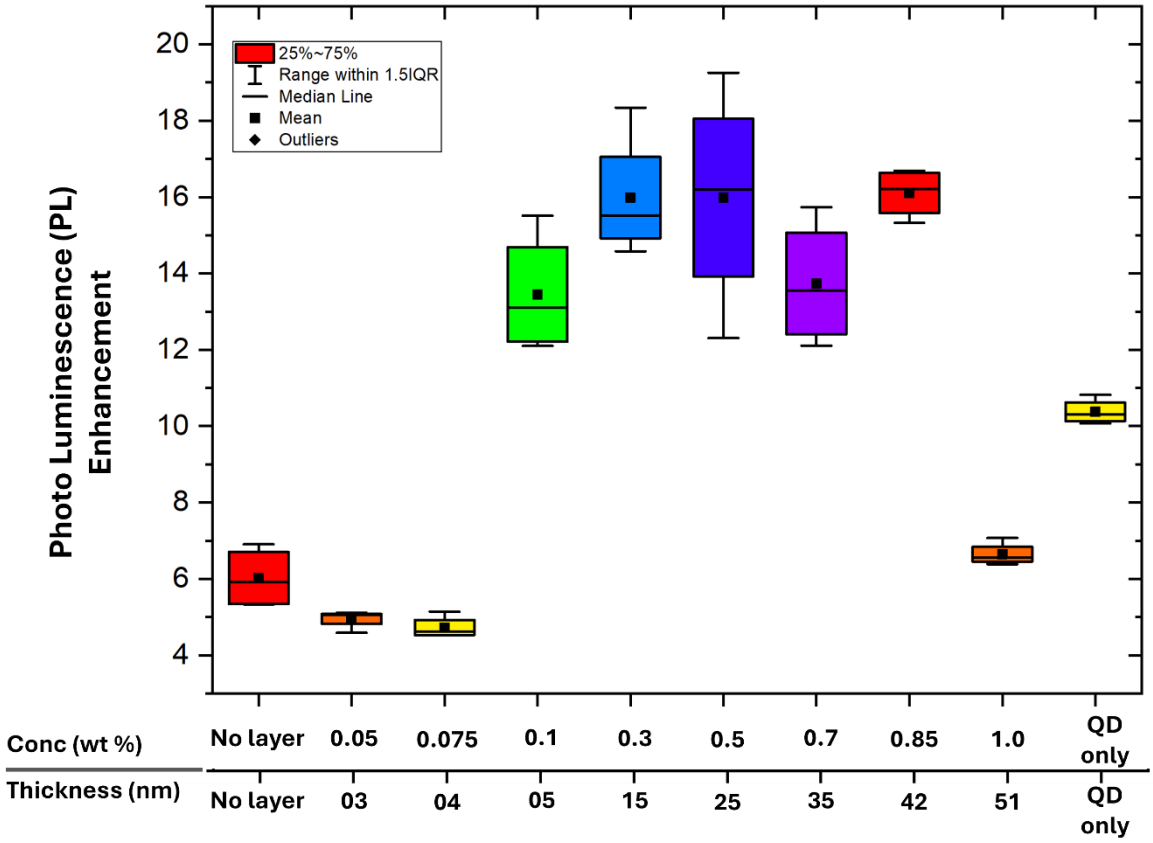

Figure 4-12: Box plots of PL data of five different samples prepared

In the absence of a spacer layer, where the QDs are effectively in direct contact with the AuNP layer, the average normalized PL is approximately 6, substantially lower than that of the QD-only reference, which is approximately 10. Similarly, at the lowest PMMA concentrations of 0.05 to 0.075 wt %, corresponding to spacer thicknesses of approximately 3 to 4 nm, the normalized PL decreases further to an average of approximately 5, that is, roughly half of the QD-only value. This strong suppression indicates that when the emitter-metal distance is too small, nonradiative energy transfer to the AuNPs

dominates the optical response. In the framework of metal-enhanced fluorescence, these configurations lie within the quenching regime, where dissipative channels associated with the metal outweigh any beneficial near-field enhancement [148], [149].

A distinct transition occurs once the spacer reaches approximately 5 nm, corresponding to 0.1 wt % PMMA. At this thickness, the average normalized PL rises to approximately 13, exceeding the QD-only reference and indicating that the system has moved out of the strong-quenching regime. With further increase in spacer thickness, the normalized PL continues to increase through the intermediate-thickness range. The average normalized PL rises from about 13 to 16 for spacer layers beginning at 5 nm, with a particularly strong value of 16.3 at 0.5 wt % PMMA, corresponding to a thickness of about 25 nm. This value represents the highest relative enhancement with respect to the QD-only reference and is therefore identified as the optimum configuration for the present system. This reflects an optimized condition for maximum QD emissions to the relative excitation input, indicating strong plasmonic enhancement of the radiative emission process [150], [151].

The enhancement trend extends over a broader intermediate-thickness interval before decreasing again at larger distances. The strongest average normalized response is obtained at 25 nm, while the broader enhancement regime extends approximately from 5 to 42 nm. Beyond approximately 42 nm, the normalized PL decreases again and approaches the weak-coupling regime. This decline is consistent with the short-range nature of plasmonic near fields. Once the QD layer is displaced too far from the AuNPs, the field amplitude experienced by the emitters becomes too weak to sustain substantial enhancement, and the structure behaves increasingly like an optically isolated QD film. The resulting non-monotonic dependence of PL on spacer thickness therefore follows the classical distance-dependent competition expected for plasmon-coupled emitters, strong quenching at very small separations, net enhancement at intermediate separations, and decaying interaction at larger distances.

The trends observed in Figures 11 and 12 are consistent with the broader state of the art in metal-enhanced fluorescence and plasmon-enhanced QD emission, but the present study contributes two points of practical significance. First, it reproduces the expected distance-controlled transition from quenching to enhancement in a planar CdSe/CdS-Au system. Second, it does so using magnetron-sputtered AuNPs, which provide a more morphology-controlled and scalable platform than many colloidal Au-based coupling architectures reported previously [152].

The quenching behavior observed for 0 to 4 nm spacing agrees well with prior reports in the literature, where very small emitter-metal separations generally lead to nonradiative energy transfer and PL suppression. Enhancement typically emerges only at intermediate distances extending to several tens of nanometres, depending on nanostructure geometry, spectral overlap, and dielectric environment.

The present results are therefore fully consistent with the accepted distance-dependent framework of plasmon-emitter coupling [151].

The optimum enhancement observed around 25 nm, within a broader 5 to 42 nm enhancement window, also compares favorably with previous spacer-controlled plasmonic QD studies. The significance of the present result does not lie in the absolute value of the optimum distance alone, but in the fact that this design window is resolved in a physically deposited AuNP system with a narrow particle-size distribution and validated across multiple independently prepared samples for each configuration. This gives the resulting spacer-thickness window stronger practical relevance for reproducible thin-film implementation [28], [150].

At the same time, the magnitude of enhancement remains moderate rather than extreme. This is scientifically reasonable and strengthens the credibility of the interpretation. Because the 375 nm excitation source is spectrally mismatched with the main AuNP absorption maximum near 585 nm, purely resonant excitation transfer is limited. In highly optimized plasmonic cavity systems or strongly resonant hotspot architectures, far larger apparent enhancements are sometimes reported, but those configurations often involve more localized field singularities, more complex geometries, and less straightforward transferability to large-area coating platforms. By contrast, the present architecture prioritizes planar fabrication control and interpretable spacer engineering over maximum possible peak enhancement [147].

This distinction is important in relation to the state of the art. Many published reports demonstrate large PL changes but do not always distinguish true radiative-rate enhancement from alternative contributions such as scattering, extraction changes, or morphology-induced collection artifacts [28], [29], [141]. The present study does not fully resolve the mechanism at the level of lifetime analysis, and therefore a strict Purcell-type attribution cannot be made. Nevertheless, the normalization strategy, the absence of a simple correlation between excitation-peak changes and geometry, and the systematic spacer-thickness dependence together provide stronger evidence for genuine plasmonic modulation than would raw intensity comparison alone. Thus, while the work does not provide the complete intensity-plus-lifetime verification often recommended in the broader metal-enhanced fluorescence literature, it advances beyond many qualitative demonstrations by combining morphology control, normalized spectral analysis, and distance-resolved statistical comparison.

From an application perspective, the results also have implications for luminescent down-shifting architectures. The CdSe/CdS QDs exhibit strong UV absorption and visible emission, while the AuNP layer can enhance the effective radiative output within an appropriate spacer-controlled geometry. This indicates that plasmonic subsystems could be used to increase the photon yield of QD-based optical coatings, provided that metal-induced absorption losses and quenching are carefully

controlled. The present study therefore does not merely show that AuNPs can alter QD PL, it defines a practical spacer-thickness window in which that alteration is beneficial rather than detrimental. This is more useful for future device-oriented design than an isolated report of enhancement without structural resolution.

4.7. Conclusion

Overall, the results show that the PL response of CdSe/CdS-Au hybrid films is governed by a clear structure-property relationship. Figures 4.4 and 4.5 establish that magnetron sputtering yields well-dispersed AuNPs with a narrow size distribution centered at 11.1 nm. Figure 4.6 confirms that these particles support visible-region plasmonic absorption, while Figures 4.7 and 4.8 show that the CdSe/CdS QDs provide the required UV absorption and visible emission for plasmon-coupled down-shifting behavior. Figures 4.9 to 4.12 then demonstrate that normalized PL depends strongly on PMMA spacer thickness, with quenching under direct contact and at 3 to 4 nm, strong enhancement beginning at about 5 nm, a best-performing configuration around 25 nm, and declining enhancement beyond approximately 42 nm.

The experimental findings therefore support the conclusion that the Au nanoparticle and spacer architecture can modulate the emission properties of CdSe/CdS colloidal films in a controlled manner. The observed enhancement indicates that careful structural design can improve the local optical environment experienced by the emitters, while the spacer-thickness dependence provides direct evidence that the effect is not merely incidental but arises from the coupled nanophotonic geometry. At the same time, the present results do not fully resolve the relative contributions of excitation-rate enhancement, modified radiative decay, extraction effects, or scattering-assisted outcoupling. For this reason, the chapter does not claim definitive proof of a pure Purcell-type mechanism, but rather demonstrates distance-controlled plasmonic modulation of quantum-dot emission.

Scientifically, the main contribution of this chapter lies in clarifying the structural conditions under which plasmonic coupling becomes beneficial instead of detrimental in this material system. This is important for the future design of photon-management layers and optoelectronic interfaces based on colloidal nanocrystals. However, the present work remains primarily an optical structure-property study, rather than a complete photovoltaic device demonstration. Further validation through comprehensive lifetime-resolved measurements, angle-dependent optical studies, and direct integration into device-relevant architectures would be necessary to determine whether the observed enhancement can translate into net photovoltaic benefit without introducing compensating parasitic losses. Thus, the chapter provides a solid mechanistic foundation for future hybrid photonic design, while appropriately limiting the claim to plasmonically modulated luminescence rather than established solar-cell enhancement.

Chapter.5 High-Resolution Prediction of Photovoltaic Module Temperature Using Sequence-Based Machine Learning

The preceding chapters examined photovoltaic improvement primarily through materials and optical engineering, specifically by enhancing spectral utilization and controlling radiative processes in quantum-dot based systems. However, photovoltaic performance under practical operating conditions is also strongly governed by thermal behavior. Module temperature directly influences voltage loss, conversion efficiency, degradation rate, and long-term reliability, and therefore constitutes a critical state variable in photovoltaic performance analysis and system management [153], [154].

Although photovoltaic operating temperature has long been described using empirical and physics-based formulations, direct module-temperature forecasting remains less developed than irradiance or power forecasting. Classical models such as those of Ross, Faiman, the Sandia Array Performance Model, SAPM, and Fuentes remain important because they are physically interpretable and computationally efficient, yet their predictive performance can deteriorate under transient irradiance, fluctuating wind conditions, and radiatively complex environments [79], [81], [83]. Conversely, many machine-learning studies report strong predictive accuracy while treating environmental variables largely as independent inputs, thereby underrepresenting thermal inertia and sequential memory, both of which are intrinsic to photovoltaic heat dynamics [31], [95]. Accordingly, the current challenge is not only to improve predictive accuracy, but also to develop a forecasting framework that is temporally informed, physically credible, and operationally trustworthy.

5.1. Background

Photovoltaic module temperature is governed by an energy balance involving absorbed solar irradiance, electrical conversion, convective heat transfer, long-wave radiative exchange, and thermal interaction with the mounting configuration. Among the various environmental factors affecting photovoltaic performance, module back-surface temperature has emerged as a particularly important, yet often underemphasized, variable. Even a 1 °C increase can reduce module voltage and efficiency by approximately 0.2 to 0.5%, while prolonged heat exposure accelerates degradation processes [153], [154]. Despite its importance, many operational forecasting systems still rely on simplified irradiance-temperature heuristics or empirical steady-state models, which often perform poorly under dynamic conditions such as passing clouds or fluctuating wind.

Historically, PV module temperature has been described using physics-based and semi-empirical formulations derived from heat-transfer principles. Early work by Ross [79] introduced a linear relationship between irradiance and cell temperature based on the nominal operating cell temperature, NOCT, providing a simple but limited approximation. Subsequent models, such as the Faiman model

(2008), improved this formulation by incorporating wind-dependent convective heat loss through empirical coefficients. More advanced approaches, including the Sandia Array Performance Model, SAPM, and the Fuentes thermal model, introduced greater physical realism by accounting for multiple heat-transfer pathways, including convection and long-wave radiative exchange [83], [85].

The Fuentes model, in particular, represents a dynamic energy-balance formulation that incorporates thermal capacitance, thereby allowing transient thermal behavior to be captured rather than assuming steady-state conditions. Similarly, more recent extensions, such as radiatively corrected Faiman-type models, incorporate downwelling infrared radiation to better represent nighttime and low-irradiance cooling processes. These developments reflect a broader progression from purely empirical formulations toward more physically grounded thermal models [81], [83].

To improve predictive accuracy, machine-learning approaches have gained increasing attention. For example, Keddouda et al. (2024) evaluated 12 machine-learning algorithms, including ANN, gradient boosting, and PCA-reduced regressors, for module-temperature prediction using irradiance, ambient temperature, wind speed, and humidity. The best-performing models achieved $R^2 \approx 0.986$and $MAE \approx 0.98$ °C [95]. Abdelsattar et al. (2025) benchmarked nine methods for PV temperature and humidity prediction and found that XGBoost yielded $MAE \approx 1.54$ °Cand $R^2 \approx 0.947$ [155]. Although these ensemble-based methods often provide strong predictive accuracy, they generally do not account explicitly for temporal sequence information or thermal inertia.

The rise of deep learning, particularly Long Short-Term Memory, LSTM, networks, CNN-LSTM hybrids, attention mechanisms, and transformer-based models, has further improved forecasting accuracy in PV power and irradiance prediction. Hybrid transformer-LSTM architectures, such as SolNet and PV-Client, have also demonstrated improved spatiotemporal modelling through cross-variable attention [156], [157]. Nevertheless, most of these studies focus on power or irradiance forecasting rather than direct module-temperature prediction [158].

In addition, many deep-learning models still omit two components that are essential for practical deployment, uncertainty quantification and explainability. Techniques such as Monte Carlo Dropout, MCD, enable probabilistic forecasting through stochastic inference [159] while SHAP values provide interpretable feature attribution for complex models [91]. However, such methods remain only rarely integrated into PV thermal forecasting. More broadly, foundational work in probabilistic and physics-informed forecasting continues to emphasize the importance of integrating uncertainty awareness and domain physics into predictive model design [89], [92], [160].

5.2. Problem Statement

Despite recent progress in photovoltaic thermal modelling, the literature does not yet provide a sufficiently integrated framework for direct module-temperature forecasting. Physics-based models such as Ross, Faiman, SAPM, and Fuentes are physically meaningful, but may lose predictive robustness under transient and radiatively complex conditions [79], [83], [85]. Conversely, many machine-learning studies improve point prediction while underrepresenting thermal memory, and relatively few combine sequence learning with uncertainty quantification, explainability, and direct benchmarking against accepted thermal models [89], [95], [155], [160]. As a result, physical relevance, temporal dependence, and model trustworthiness are still too often treated as separate objectives rather than as concurrent requirements of a reliable photovoltaic temperature forecasting framework.

Accordingly, this chapter investigates photovoltaic module temperature prediction using high-resolution field measurements through a comparative framework that includes physics-based thermal models, ANN and LSTM architectures, feature engineering informed by photovoltaic thermal physics, Monte Carlo Dropout uncertainty analysis, and SHAP-based interpretability assessment. The scientific contribution of this chapter lies in evaluating temperature forecasting not only as an accuracy problem, but as a unified modelling problem requiring temporal learning, physical benchmarking, uncertainty awareness, and interpretability within the same study. In this way, the chapter aims to establish whether an LSTM-based framework can provide a more accurate and operationally credible representation of real-world photovoltaic thermal behavior than conventional empirical and semi-empirical temperature models. In this context, operational credibility means that the model should not only reduce prediction error, but should also follow physically meaningful trends with irradiance, ambient temperature, wind speed, and long-wave radiative cooling.

5.3. Methodology Section

5.3.1 Data Source and Collection

The dataset used in this study was obtained from the DuraMAT DataHub, specifically the module temperature dataset maintained by Sandia National Laboratories under the Systems Long-Term Evaluation (SLTE) project. This open-access dataset captures high-resolution, real-world environmental and operational conditions for PV modules located at the Photovoltaic Systems Evaluation Laboratory (PSEL) in Albuquerque, New Mexico (35.05°N, 106.54°W, elevation: 1660 m).

5.3.2 Key Attributes of the Dataset

Time resolution: 1-minute averaged values (from 1 to 5 second sensor readings)

Time coverage: Seven months of the year 2020 from Jan to July (excluding Jan 20–30 maintenance gap)

The raw dataset contains timestamps, plane-of-array (POA) irradiance, air temperature, infrared downwelling radiation, and module back-surface temperature measurements. Infrared downwelling radiation was included because long-wave radiative exchange contributes significantly to module cooling, particularly during low-irradiance periods. After eliminating null or missing values, the dataset was chronologically ordered and resampled to ensure consistent temporal spacing. The final dataset contained over 216,236 valid entries (Approximately, 51.5 % of samples are daylight, based on poa_global > 10) used for model training and evaluation. The threshold poa_global > 10 W m^{-2} is used to distinguish periods with meaningful solar heating from night or near-dark conditions.

Measured parameters:

- Plane-of-array irradiance (POA) using Kipp & Zonen CMP11 sensors
- Air temperature using Climatronics aspirated shield sensors
- Wind speed at 10 m height
- Infrared downwelling radiation (estimated from ECMWF data)
- Back-of-module temperatures (four Omega SA1-RTD sensors)

These parameters were measured on centrally located 325 W Panasonic HIT modules, chosen to minimize edge and boundary effects.

5.3.3 Feature Engineering

The predictive model was trained on a mix of **physical, temporal, and statistical features**: The input features are given in Table 5.1.

Table 5-1: Input features including physical, temporal and derived statistical features

Type	**Features**
Core environmental	poa_global, wind_speed, temp_air, ir_down
Temporal markers	hour, day, month
Derived indicators	diff_poa (difference between current and last irradiance value), rolling_air_temp (last ten-minute rolling average), is_daylight (poa_global > 10)

This comprehensive input space allowed the models to learn both static and dynamic characteristics of PV module thermal behavior under changing atmospheric conditions. To enhance the model's ability to capture the physical processes governing PV module temperature, several engineered features were included based on their thermodynamic relevance. The ir_down (downwelling infrared radiation) feature is particularly important during nighttime or low-irradiance periods when convective and longwave radiative exchanges dominate PV cooling, despite negligible solar input. diff_poa captures rapid irradiance changes due to cloud movement, whereas rolling_air_temp represents short-term thermal inertia in the environment. Feature engineering operations that depend on temporal aggregation (rolling_air_temp, diff_poa) were computed using only past values within the training window to prevent data leakage. Data normalization was applied exclusively to the training set and then extended to the validation and test sets. The diff_poa, representing the temporal gradient of plane-of-array irradiance, captures rapid changes in solar exposure (e.g., due to cloud transients), which directly influence the short-term heating rate of the module surface. Temporal features such as hour and day are used to encode diurnal and seasonal variations, respectively, accounting for the cyclical nature of irradiance, ambient temperature, and sun angle, all of which influence the module's thermal behavior over different timescales.

5.4. Model Architecture and Training

Seven different models were developed and evaluated to predict the back-surface temperature of the PV module:

5.4.1 Physics based models

In addition to data-driven models, several physics-based thermal models were implemented to provide a benchmark for comparison. These models estimate PV module temperature using simplified or semi-empirical formulations derived from heat transfer principles.

The following models were evaluated:

- Fuentes PV thermal model
- Faiman PV temperature model
- Faiman model with radiative correction (Faiman-rad)
- Sandia Array Performance Model (SAPM) module temperature model
- Ross PV temperature model

These models represent different levels of complexity, ranging from simple empirical relationships to more comprehensive energy-balance-based formulations.

The Fuentes model is based on a steady-state energy balance that accounts for absorbed solar radiation, convective heat loss, and longwave radiative exchange. The Faiman model represents heat loss using empirical coefficients dependent on wind speed, while the Faiman-rad variant extends this formulation by incorporating radiative heat exchange using downwelling infrared radiation.

The SAPM module temperature model, developed by Sandia National Laboratories, estimates module temperature using empirically derived coefficients based on irradiance and wind speed. The Ross model assumes a linear relationship between irradiance and temperature based on nominal operating cell temperature (NOCT), representing one of the simplest thermal formulations.

All physics-based models were implemented using the same measured input variables available in the dataset, ensuring consistency in comparison with the data-driven approaches. The models are given in Table 5.2.

Table 5-2: Physics-based model for determining PV module temperature

Model	**Equation**	**Notation**	**Reference**
Ross PV temperature model	T_c = T_a + ((NOCT - 20)/800) * E_POA	T_c: cell temperature (°C); T_a: ambient temperature (°C); NOCT: nominal operating cell temperature (°C); E_POA: irradiance (W m^{-2})	Ross (1980)
Faiman PV temperature model	T_m = T_a + E_POA / (U_0 + U_1 * WS)	T_m: module temperature (°C); T_a: ambient temperature (°C); E_POA: irradiance (W m^{-2}); WS: wind speed (m s^{-1}); U_0, U_1: heat loss coefficients	Faiman (2008)
Faiman-rad	q_rad = ε * F_sky * (σ * (T_a + 273.15)^4 - IR_down)T_m = T_a + (E_POA - q_rad) / (U_0 + U_1 * WS)	ε: emissivity; F_sky: sky-view factor; σ: Stefan–Boltzmann constant; IR_down: downwelling IR (W m^{-2}); others as above	Driesse et al. (2022)
SAPM module model	T_m = T_a + E_POA * exp(a + b * WS)	a, b: empirical coefficients; other terms as above	King et al. (2004), Sandia

			National Laboratories
Fuentes PV thermal model	C * dT_m/dt = α * E_POA - h_c * (T_m - T_a) - ε * σ * (T_m^4 - T_sky^4)	C: thermal capacitance; α: absorptance; h_c: convective coefficient; T_sky: sky temperature; ε, σ: radiative terms; others as above	Fuentes (1987), Dobos (2014)

5.5. Data-driven models

Two classes of data-driven models were developed: Artificial Neural Networks (ANN) and Long Short-Term Memory (LSTM) networks.

5.5.1 Artificial Neural Networks (ANN)

Three ANN variants were developed:

- **Baseline ANN** using only basic features (ANN_Baseline),
- **ANN with full feature engineering**, incorporating temporal and statistical features (ANN_Baseline_FE),
- **ANN with PCA**, where principal components (retaining 95% variance) were used as input features to reduce dimensionality (ANN_PCA).

Each ANN model was trained using scikit-learn's MLPRegressor with hyperparameter tuning for hidden layer sizes, activation functions, and early stopping.

5.5.2 Long Short-Term Memory Networks (LSTM)

Four LSTM configurations were examined:

- **Raw LSTM** using basic features without sequence context,
- **Tuned LSTM** with optimized hyperparameters,
- **LSTM with sequence window of 5**, capturing short-term history,
- **LSTM with sequence window of 50**, enabling long-range temporal dependency,

All LSTM models were implemented using Keras with TensorFlow backend. The inputs were reshaped into 3D tensors (samples, timesteps, features), and models were trained using Mean Squared Error loss and the Adam optimizer. Early stopping and model checkpointing were used to prevent overfitting. Window of 5 and 50 was selected because the thermal response of PV modules is typically characterized by a time constant of 5–20 minutes for standalone modules, while systems integrated

with additional thermal mass (e.g., BIPV or roof structures) can exhibit response times approaching tens of minutes or up to ~1 hour due to increased thermal capacitance. The shorter window captures rapid thermal response, while the longer window captures slower thermal inertia and delayed heat exchange [161], [162].

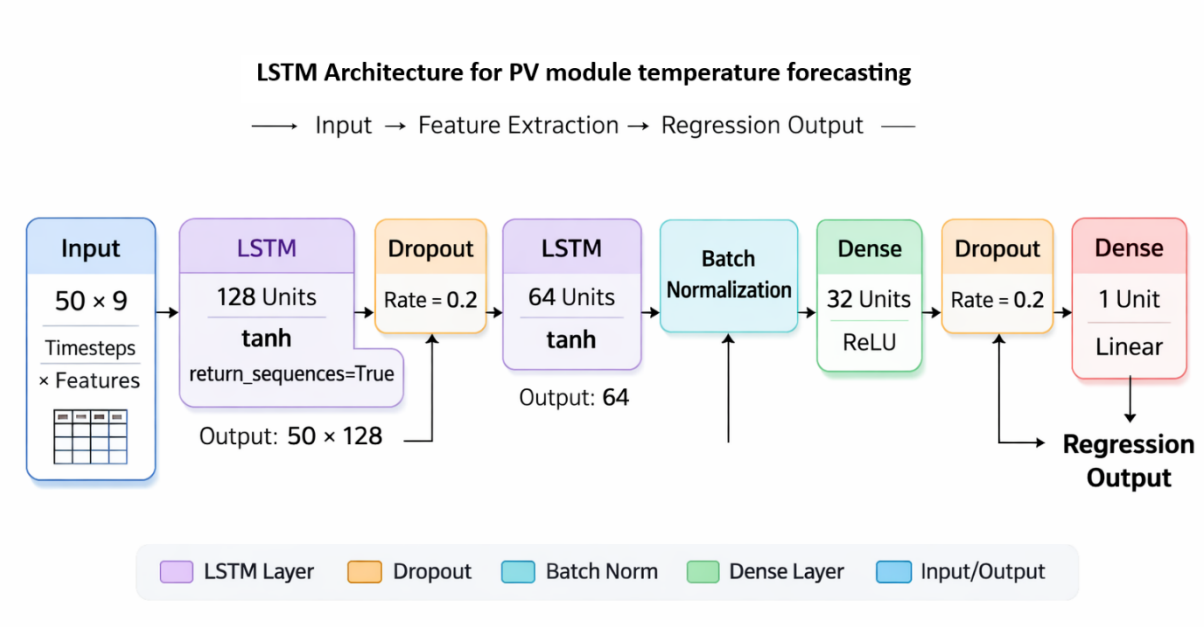

Figure 5-1: LSTM Architecture for PV module temperature forecasting

Figure 5.1 shows stacked LSTM architecture for PV module temperature prediction. The LSTM model uses a sliding window of 50 timesteps as input. Each training sample contains environmental observations from the preceding 50 minutes (t−49 to t). The model predicts the PV module back-surface temperature at the next timestep (t+1). Given the 1-minute sampling interval, the framework therefore performs 1-minute-ahead temperature forecasting with a 50-minute lookback window.

Before training, all input features were standardized using StandardScaler. Sliding window sequence generation with a window length of 50 was used to transform the tabular time-series data into supervised learning samples. The dataset was divided chronologically into training and testing subsets to preserve the temporal dependency inherent in time series data. The first 80% of the observations were used for training, while the remaining 20% were reserved for testing. Random shuffling was avoided to prevent information leakage from future observations. The model was trained using the Adam optimizer with mean squared error, MSE, as the loss function and mean absolute error, MAE, as the evaluation metric. Training was performed for up to 100 epochs with a batch size of 64. To prevent overfitting and improve generalization, early stopping with a patience of 5 epochs was used based on validation loss, and the best model weights were saved using model checkpointing.

5.5.3 Subset Scenario Testing

To assess model robustness under specific operating conditions, the best-performing model (LSTM with a 50-time-step sequence window) was further evaluated on selected environmental scenarios:

- **Peak Solar Hours** (11:00–14:00),
- **High Wind Conditions** (top 5% of wind speeds),
- **Summer Temperatures** (June to July).

These subsets were extracted post-preprocessing and used to generate condition-specific predictions and evaluation metrics.

5.5.4 Model Evaluation

All models were evaluated using:

- **Mean Absolute Error (MAE)**,
- **Root Mean Squared Error (RMSE)**,
- **Coefficient of Determination (R^2)**.

5.5.5 Uncertainty Estimation and Explainability

To further analyze model reliability:

- **Monte Carlo Dropout** was applied to estimate uncertainty bounds, revealing confidence intervals that widened during irradiance transitions (e.g., morning and evening).
- **SHAP (SHapley Additive exPlanations)** SHAP (SHapley Additive exPlanations) analysis was used as a post hoc interpretability tool to examine the contribution of input variables to the LSTM model's predictions. Because the LSTM operates on sequential inputs, each 50-step sequence with 9 features was flattened into a 450-dimensional vector for SHAP analysis and reshaped back to the original sequence format during prediction. Kernel SHAP was applied using 30 randomly selected background samples, and explanations were computed for a representative subset of overall test sequences. The resulting analysis was used to derive both global feature-importance rankings and timestep-wise contribution heatmaps.

This comprehensive methodology integrates data acquisition, feature engineering, neural network modeling, scenario testing, and explainability techniques to develop and validate a robust temperature prediction model for photovoltaic modules. The use of the DuraMAT dataset and advanced deep learning methods provides a reproducible and scalable framework for thermal modeling in PV systems.

5.6. Results

5.6.1 Physics-based models

To establish a physically interpretable benchmark for photovoltaic (PV) module temperature prediction, several widely used thermal models were evaluated using the same test dataset and performance metrics. Figure 5.2 presents a grouped comparison of model performance in terms of Mean Absolute Error (MAE), Root Mean Squared Error (RMSE), and coefficient of determination (R^2).

Among the evaluated physics-based approaches, the Fuentes PV thermal model achieved the highest predictive accuracy, with a MAE of 2.697 °C, RMSE of 3.129 °C, and R^2 of 0.967. This indicates that the model is able to capture a large portion of the variability in module temperature under real-world operating conditions.

The Faiman model with radiative correction (Faiman-rad) demonstrated the second-best performance, achieving a MAE of 3.193 °C and RMSE of 4.074 °C. The inclusion of longwave radiative exchange through downwelling infrared radiation improves its predictive capability compared to the standard Faiman PV temperature model, which yielded higher errors (MAE ≈ 4.497 °C, RMSE ≈ 5.085 °C).

The Sandia Array Performance Model (SAPM) module temperature formulation, developed by Sandia National Laboratories, showed moderate performance, with MAE and RMSE values of approximately 4.427 °C and 4.974 °C, respectively. Although this model is specifically designed for module temperature estimation, its reliance on fixed empirical coefficients limits its adaptability to site-specific and transient environmental conditions.

The Ross PV temperature model exhibited the lowest accuracy among all models, with MAE exceeding 5 °C and R^2 dropping to 0.891. This reduced performance reflects the simplified linear formulation of the Ross model, which neglects key heat transfer processes such as wind-driven convection and radiative exchange.

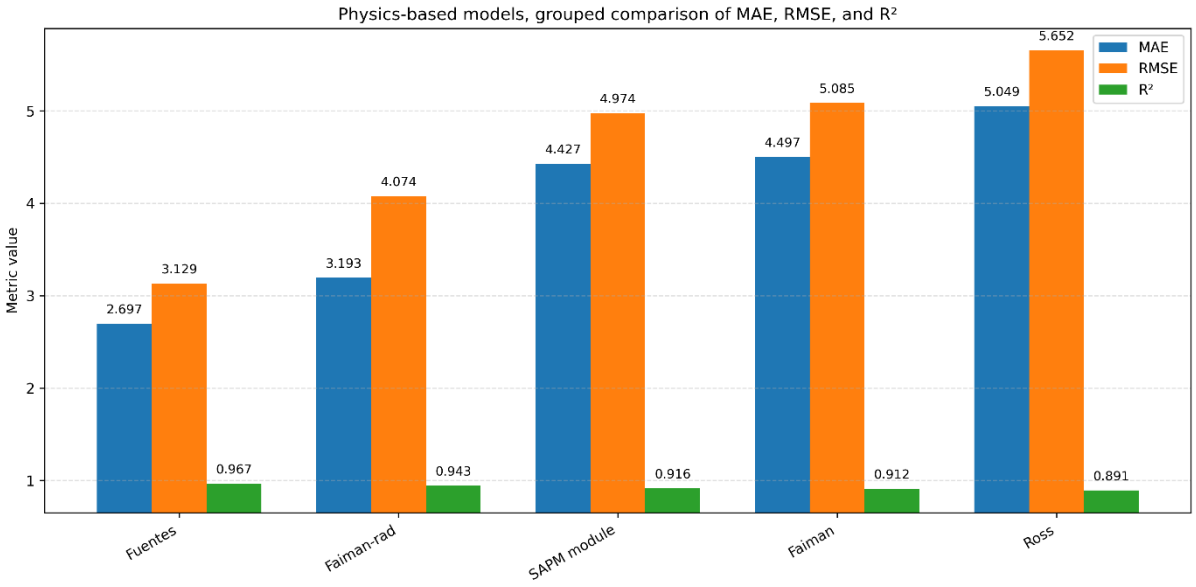

Figure 5-2: Comparison of Physics-based models' performance evaluation metrics

The differences in model performance can be explained by the level of physical realism embedded in each formulation.

The superior performance of the Fuentes model is primarily attributed to its energy balance formulation, which explicitly accounts for absorbed solar radiation, convective heat loss, and longwave radiative exchange. By incorporating multiple heat transfer pathways, the model can better respond to variations in environmental conditions such as wind speed and atmospheric radiation. Energy-balance-based approaches have been widely recognized for their improved predictive capability under dynamic conditions (Fuentes, 1987; Dobos, 2014).

The improved performance of the Faiman-rad model compared to the standard Faiman formulation further emphasizes the role of radiative heat transfer. In real-world conditions, longwave radiation exchange between the module and the sky significantly influences thermal behavior, particularly during low irradiance periods and nighttime cooling. By including downwelling infrared radiation, the Faiman-rad model captures this effect, leading to a measurable reduction in prediction error.

In contrast, the SAPM model relies on empirically calibrated coefficients derived from controlled experimental conditions. While it performs reasonably well under steady-state conditions, its limited flexibility reduces its accuracy under rapidly changing environmental conditions, such as transient cloud cover or fluctuating wind speeds. Similar limitations of semi-empirical PV temperature models have been reported in previous studies (King et al., 2004).

The Ross model performs the worst due to its highly simplified structure. As one of the earliest PV temperature models, it assumes a linear relationship between irradiance and temperature based on nominal operating cell temperature (NOCT). However, it does not account for wind cooling, radiative

exchange, or temporal thermal inertia, making it unsuitable for high-resolution, real-world datasets (Ross, 1980).

5.6.2 Data Driven Models

Figure 5.3 presents a comparative evaluation of seven predictive models developed for photovoltaic (PV) module back-surface temperature forecasting. The models are assessed using three standard regression metrics: Mean Absolute Error (MAE), Root Mean Squared Error (RMSE), and Coefficient of Determination (R^2). The aim is to determine the efficacy of different neural network configurations in capturing the thermal behavior of PV modules under varying conditions.

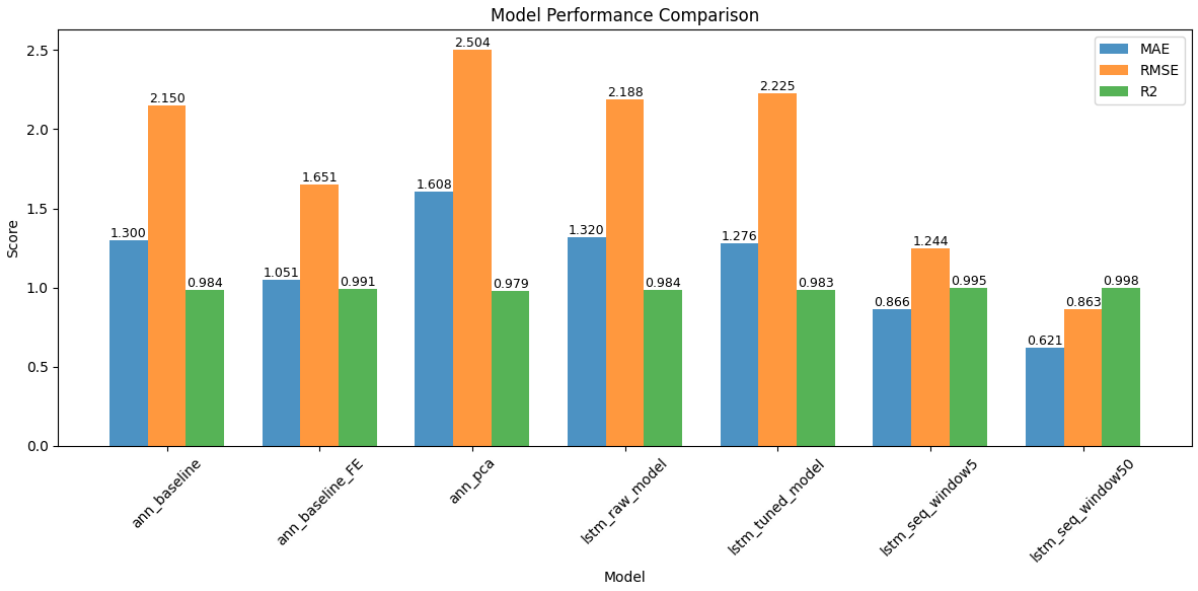

Figure 5-3: Comparison of data-driven predictive models' performance evaluation metrics

5.6.3 ANN-Based Models

The ANN with feature engineering (ann_baseline_FE) demonstrated the best performance among the ANN variants, achieving a MAE of 1.051°C, RMSE of 1.651°C, and a high R^2 of 0.9907. This highlights the importance of domain-informed feature engineering, which includes temporal and statistical descriptors such as rolling air temperature and irradiance differences. By enriching the model's input space with derived features, it is able to better encapsulate the dynamic thermal processes in PV modules.

In contrast, the ANN trained solely on raw features (ann_baseline) showed degraded performance, with a higher RMSE (2.150°C) and a lower R^2 (0.9843). This reinforces the understanding that while ANNs can model nonlinear relationships, the quality and informativeness of input features remain critical to their generalization ability.

The ANN using PCA (ann_pca), intended to reduce feature dimensionality, performed the worst among all models with RMSE of 2.504°C and R^2 of 0.9787. This indicates that PCA may have

inadvertently removed essential variability linked to weather and irradiance fluctuations. It also suggests that reducing dimensionality without preserving temporal interpretability can be detrimental, particularly in time-sensitive physical systems.

5.6.4 LSTM-Based Models

The LSTM architectures showed progressive improvement as temporal structure was increasingly leveraged. The raw LSTM model yielded MAE and RMSE values of 1.320°C and 2.188°C, respectively, with $R^2 = 0.9837$. Slightly better performance was observed for the tuned LSTM model, with marginal improvements in MAE (1.276°C) and RMSE (2.225°C), though the R^2 dropped slightly (0.9832). This limited gain suggests that while LSTM tuning helps with convergence and training stability, the sequence input structure is more critical.

Significant performance enhancement emerged with the use of sequence-windowed LSTM models. The LSTM model using a 5-step input window (lstm_seq_window5) achieved RMSE = 1.244°C and $R^2 = 0.995$, demonstrating improved short-term temporal context handling. Most notably, the LSTM with a 50-time-step window (lstm_seq_window50) recorded the lowest MAE (0.621°C) and RMSE (0.863°C) across all models, along with the highest R^2 (0.998). This result illustrates the model's ability to internalize long-range dependencies and temporal evolution patterns, which are essential in capturing lagged thermal responses to environmental changes.

5.6.5 Discussion and Scientific Insights

The results validate the hypothesis that temporal context and informed feature selection are pivotal in modeling PV module temperatures accurately. While ANN models are computationally efficient and perform well when enhanced with engineered features, their performance plateaus without temporal memory.

The degradation in the PCA-based ANN model highlights a key trade-off in machine learning for physical systems: dimensionality reduction can obscure domain-relevant patterns, especially when components with lower statistical variance carry significant physical meaning (e.g., irradiance transients during cloud passage).

On the other hand, LSTM networks inherently preserve temporal sequences, and their performance scales with the length and quality of the input window. The superior performance of the lstm_seq_window50 model supports findings in prior research that thermal dynamics in PV systems exhibit temporal inertia—with system temperatures responding not only to current irradiance but also to preceding environmental conditions over several minutes.

In summary, the integration of temporal learning through deep sequence modeling (LSTM) combined with engineered features results in the most accurate predictions. This has practical implications for real-time thermal forecasting, anomaly detection, and energy yield management in PV installations.

5.7. Comparison of overall best model

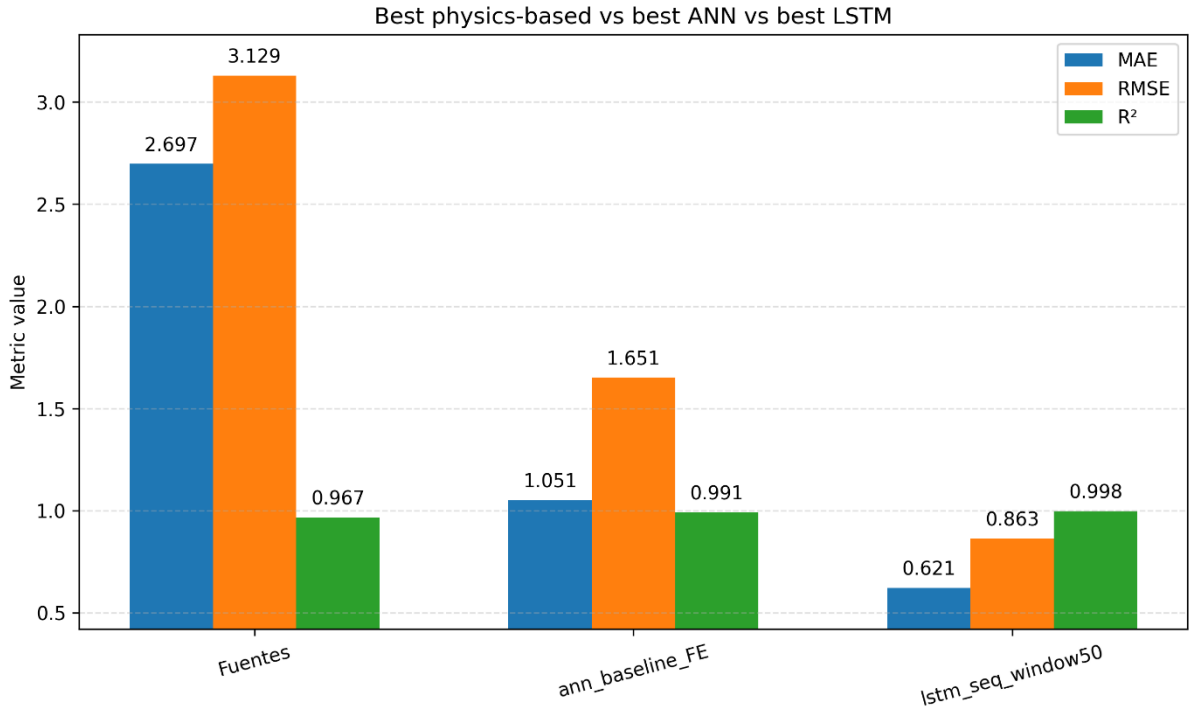

Figure 5-4: Comparison of best performing data driven and physics based models

Figure 5.4 represent the best performing model among physics based and data driven based models. While the physics-based models provide valuable physical insight, their predictive accuracy is significantly lower than that of the data-driven models developed in this study. The best-performing LSTM model achieved a MAE of approximately 0.621 °C and an R^2 exceeding 0.997, substantially outperforming even the most advanced physics-based model (Fuentes).

This performance gap highlights a fundamental limitation of physics-based thermal models. These models rely on fixed or semi-empirical parameters that cannot fully capture the complex, nonlinear interactions between environmental variables and module temperature under real operating conditions. In particular, they are limited in their ability to represent: transient irradiance fluctuations due to cloud movement, delayed thermal response (thermal inertia), nonlinear interactions between wind, irradiance, and ambient temperature.

In contrast, the LSTM model leverages sequence learning to capture temporal dependencies and dynamic system behavior. By incorporating historical information, the model effectively learns thermal lag effects and transient responses that are not explicitly represented in traditional formulations.

These findings are consistent with recent studies demonstrating that deep learning models outperform classical approaches in complex energy systems characterized by nonlinear and time-dependent behavior.

5.7.1 Overfitting and Generalization Assessment

To evaluate the generalization capability and potential overfitting behavior of each model, a comparative analysis of training and testing performance was conducted. The results are presented in Figure X, showing side-by-side bar charts of three critical evaluation metrics: Mean Absolute Error (MAE), Root Mean Squared Error (RMSE), and the Coefficient of Determination (R^2).

5.7.1.1. Observations from MAE and RMSE Trends

The training and testing curves for all models closely align across MAE and RMSE metrics as shown in Figure 5.5, suggesting effective generalization without signs of severe overfitting. The gap between train and test MAE/RMSE is consistently narrow (<0.01–0.02 in most cases), indicating that none of the models exhibit memorization behavior, which is often seen as a hallmark of overfitting.

The lstm_seq_window50 model, which uses a long temporal context of 50 time steps, not only achieved the lowest absolute errors on both training (MAE: 0.613, RMSE: 0.829) and testing (MAE: 0.621, RMSE: 0.863) datasets, but also maintained an extremely small

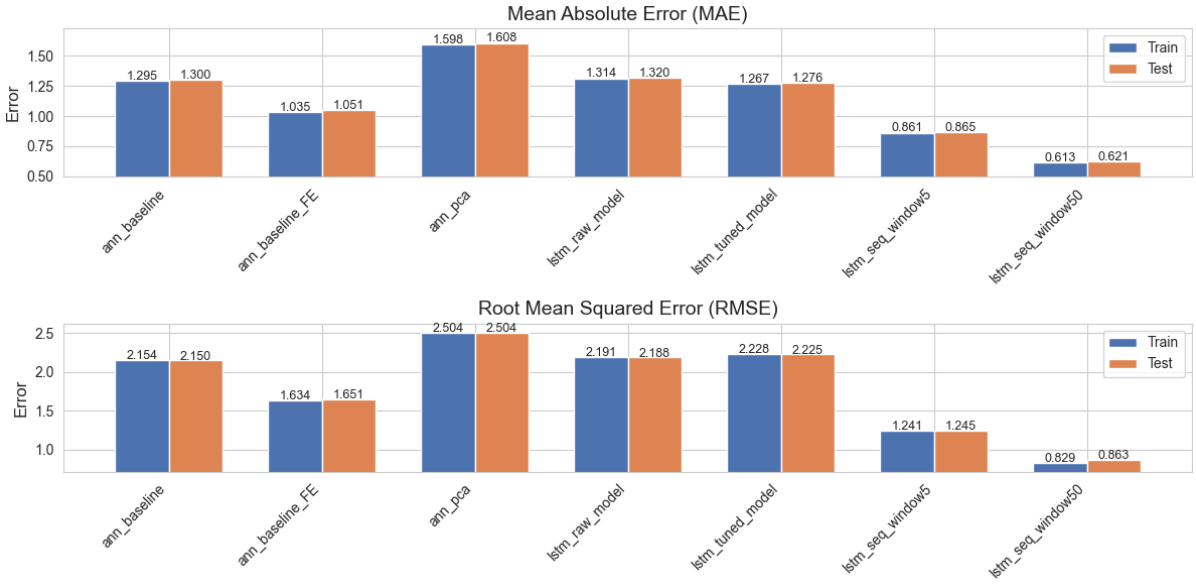

Figure 5-5: Evaluation metrics comparison on train and test data

generalization gap. This confirms that the model's complexity, driven by temporal depth, does not compromise its ability to perform well on unseen data. It is capable of capturing and generalizing time-dependent patterns in PV module thermal behavior effectively.

The ann_baseline model, enhanced through feature engineering, also performed admirably with negligible performance drops between training and test sets (MAE: 1.035 vs. 1.051, RMSE: 1.634 vs. 1.651). This again validates the impact of domain-specific feature enrichment in boosting both accuracy and generalization.

On the contrary, the ann_pca model shows relatively higher errors and maintains consistent training and testing values (MAE: 1.598 vs. 1.608; RMSE: 2.504 for both). While this consistency rules out overfitting, it also reveals that the PCA-based input compression failed to capture important nonlinear interactions, likely resulting in underfitting.

5.7.2 R^2 Behaviour and Stability

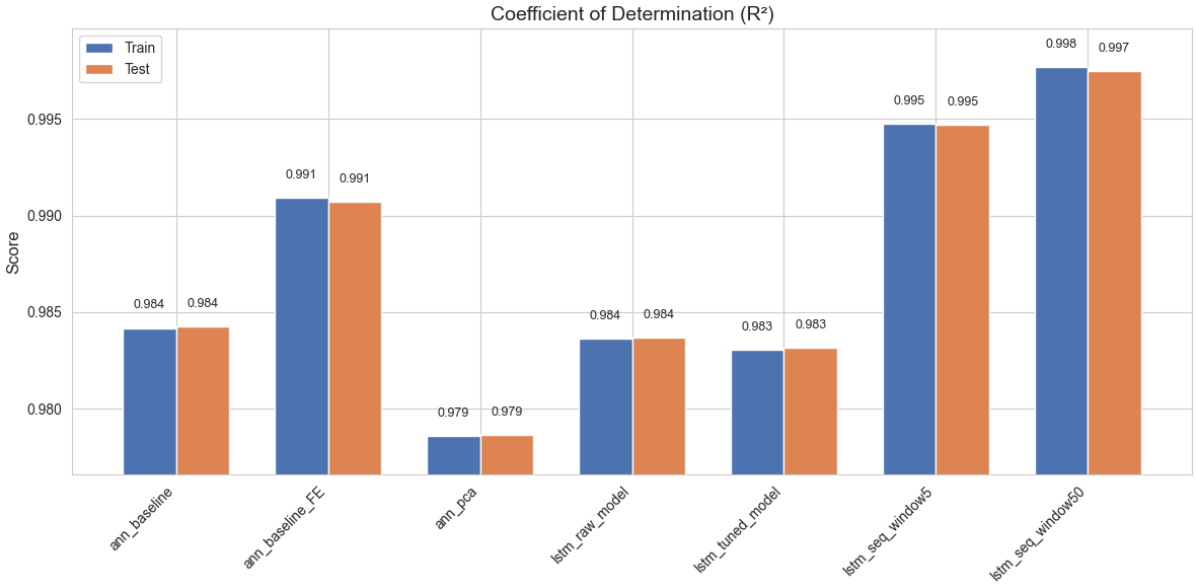

Figure 5-6: Coefficent of Determination of different data driven models

The R^2 scores values as shown in Fig 5.6 across all models remained very high (≥ 0.978), with marginal variation between training and testing sets. Notably, the lstm_seq_window50 model achieved the highest R^2 values of 0.998 (train) and 0.997 (test), reflecting its exceptional capability in explaining variance in temperature data. These values underscore the model's robustness and stability under both training and generalization scenarios.

The consistency of R^2 values across train and test datasets in all models affirms model stability, even for architectures with varying complexities. This also strengthens the validity of the learning strategy, which incorporates early stopping, appropriate sequence windows (for LSTM), and engineered features (for ANN).

5.7.3 Generalization vs. Complexity Trade-off

The absence of overfitting across all architectures, despite their diverse structural and computational complexities, demonstrates the effectiveness of the adopted regularization mechanisms—such as early stopping and validation-based checkpointing. These results provide compelling evidence that:

- Sequence-aware LSTM models with longer memory (e.g., 50-time-step input) can outperform simpler models while maintaining generalization.
- Feature engineering offers a lightweight yet powerful approach to boost model performance, especially for shallow models like ANN.
- Dimensionality reduction via PCA, while useful for reducing computational cost, may impair accuracy if it removes physically meaningful components, leading to underfitting rather than overfitting.

In practical terms, this analysis reinforces that high-performing temperature forecasting models for PV systems must balance architectural depth with temporal and statistical richness in inputs. The results validate that deep models, when carefully trained and evaluated, can avoid overfitting and deliver reliable performance across varied operational conditions.

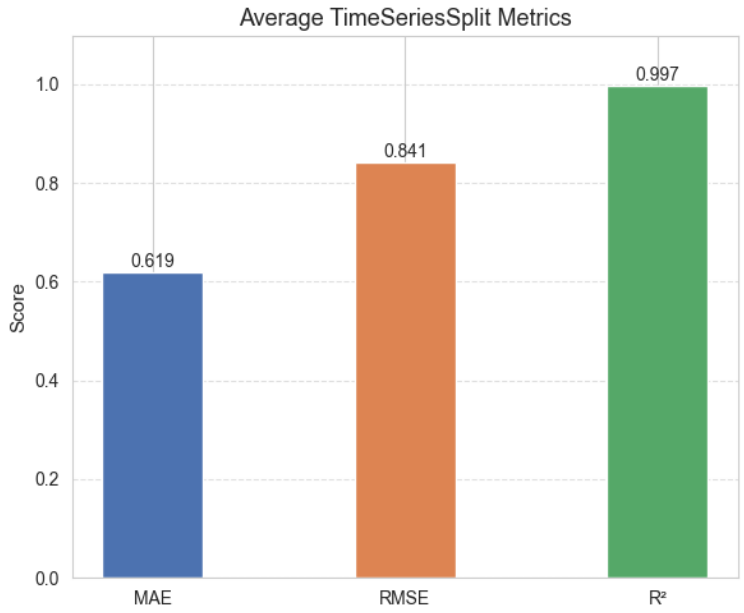

Figure 5-7: Time series cross-validation performance

5.7.4 Average Time-Series Cross-Validation Performance

To robustly assess the generalization capability of the lstm_seq_window50 model, a five-fold timeseries split cross-validation was employed. Unlike random k-fold approaches, this method respects temporal order—ensuring that the model is always validated on future data it hasn't seen

during training. This is essential for time-series problems like PV temperature forecasting, where temporal causality must be preserved.

As shown in Figure 5.7, the model achieved an average MAE of 0.619, RMSE of 0.841, and R^2 of 0.997 across all folds. These values are consistent with its static test performance, indicating strong generalization and no signs of overfitting. The high R^2 confirms the model's ability to capture nearly all variance in unseen, time-forward data.

These findings validate the model's robustness in dynamic operational environments and confirm its suitability for real-time, sequence-based temperature forecasting in photovoltaic systems.

5.7.5 Monte Carlo Dropout Uncertainty Analysis

To further enhance the interpretability and reliability of the lstm_seq_window50 model, a Monte Carlo Dropout (MC Dropout) analysis was conducted to estimate predictive uncertainty. Unlike standard deterministic inference, this method retains dropout during prediction and performs multiple stochastic forward passes, thereby capturing epistemic uncertainty—variability due to limited model knowledge. In this study, the model was evaluated on a subset of 2000 sequences, and 50 Monte Carlo samples were used per input to calculate the distribution of predictions.

As shown in Figure 5.8, the blue curve represents the mean predicted PV module temperature across all Monte Carlo passes, while the shaded envelope indicates ±1 standard deviation, representing the model's predictive confidence. The red markers identify high-uncertainty predictions—specifically, points where the standard deviation exceeded the 95th percentile threshold of 3.4354. A total of 100 such points were detected, corresponding to 5% of the samples.

The uncertainty bands were found to be widest during periods of rapid environmental transition, particularly around the steep rise and peak of the temperature curve (sample indices ~500–900). These regions likely correspond to dynamic atmospheric conditions such as early morning irradiance ramps or transient cloud events, where input data may fluctuate and temporal patterns are harder to resolve. In contrast, the early morning (samples <400) and late afternoon segments (samples >1400) exhibited narrow confidence intervals, reflecting high model certainty during thermally stable conditions.

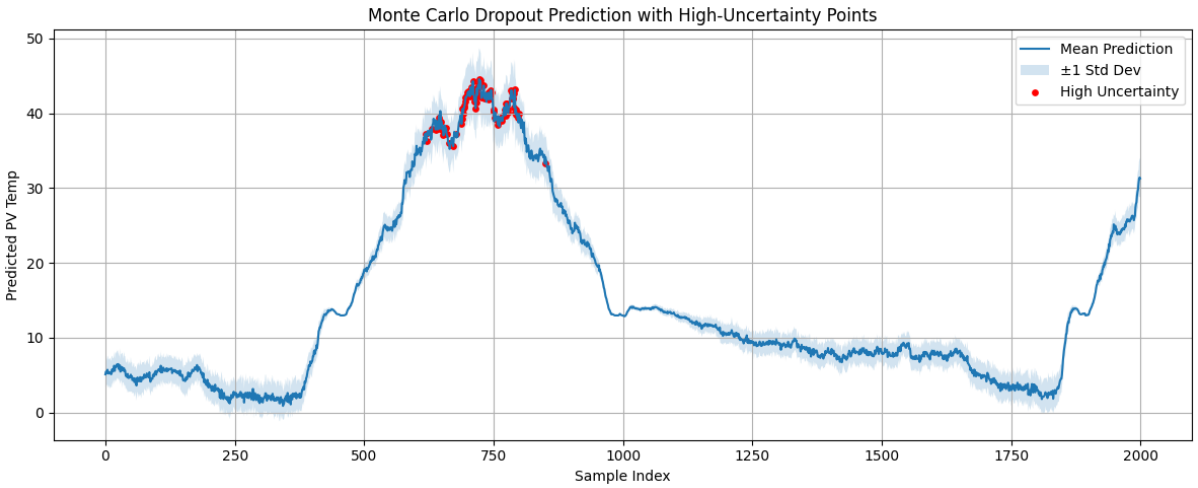

Figure 5-8: Monte Carlo Prediction on High Uncertainty Data Points

This uncertainty analysis provides an important layer of interpretability. It demonstrates that while the model is highly confident under stable conditions, it appropriately recognizes and flags its own limitations during volatile periods. Such insight is vital for real-world applications, as it allows system operators to differentiate between reliable and uncertain forecasts. High-uncertainty predictions could inform risk-aware decision-making, trigger fallback control strategies, or prompt further data verification.

Incorporating uncertainty quantification into deep learning models such as LSTM improves not only forecast accuracy but also operational trustworthiness. By exposing when the model is unsure, MC Dropout transforms a black-box predictor into a more transparent and actionable forecasting tool—critical for safe and robust deployment in photovoltaic power

5.7.6 SHAP analysis

To improve interpretability of the trained lstm_seq_window50 model, SHAP analysis was performed on the overall sample using the model-agnostic Kernel SHAP method. Because the LSTM receives sequential inputs, each sample consists of a 50-step multivariate sequence with 9 features per timestep. For SHAP computation, each sequence was flattened into a 450-dimensional vector, while predictions were generated by reshaping the vector back to the original (50, 9) sequence format before passing it to the trained model. A random subset of 30 background samples was used to initialize the explainer, and SHAP values were computed for a representative subset of overall sequences.

The SHAP bar plot for the overall sample as shown in Figure 5.9 illustrates the relative importance of each input feature in the LSTM model's prediction of PV module temperature. Quantitatively, *poa_global* (plane of array irradiance) holds the highest mean absolute SHAP value (≈0.313), indicating it is the dominant driver of temperature variation across all time steps. This is scientifically consistent, as solar irradiance is the primary source of heat absorbed by the PV module surface. The

second most influential feature is *temp_air* (≈0.165), reflecting the environmental baseline temperature that contributes to convective heat exchange between the module and the ambient air. *Rolling_air_temp* follows closely (≈0.136), capturing short-term thermal memory that informs the model of recent environmental stability or fluctuation. Wind speed showed lower global SHAP importance, likely because its cooling effect is indirectly captured through changes in module temperature and air temperature. Features like *wind_speed*, *diff_poa*, and *is_daylight* show near-zero contributions in this global analysis, suggesting that while they may play roles in localized or specific conditions (e.g., during rapid weather transitions or at night), their overall impact across the dataset is marginal. This ranking confirms that the model prioritizes features with strong physical ties to heat transfer processes, enhancing the scientific interpretability and reliability of its predictions.

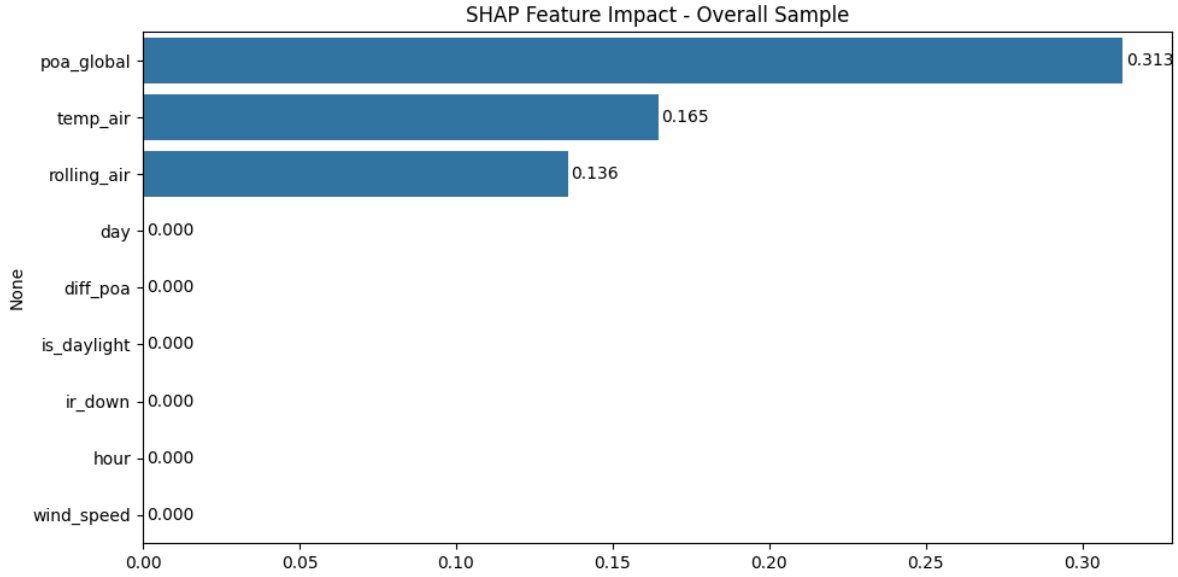

Figure 5-9: SHAP feature Impact bar chart for all the input features

The temporal SHAP heatmap for the overall sample as shown in Figure 5.10 provides deeper insight into how the LSTM model leverages historical patterns across the 50-minute input window. The most influential contributions occur in the final few time steps (closer to t_0), especially for *poa_global*, *temp_air*, and *rolling_air_temp*. This confirms that the model relies heavily on recent irradiance and ambient temperature trends to predict PV module temperature, capturing short-term thermal lag effects. The sharp gradient of SHAP intensity near the present moment (t_0 to t-5) reflects the system's responsiveness to immediate environmental changes, which aligns with the thermodynamic behavior of PV modules that react quickly to irradiance fluctuations and thermal loading. Notably, features such as *ir_down*, *day*, and *hour* contribute negligibly across all time steps, supporting the earlier finding that temporal dynamics of environmental conditions are more predictive than static temporal encodings.

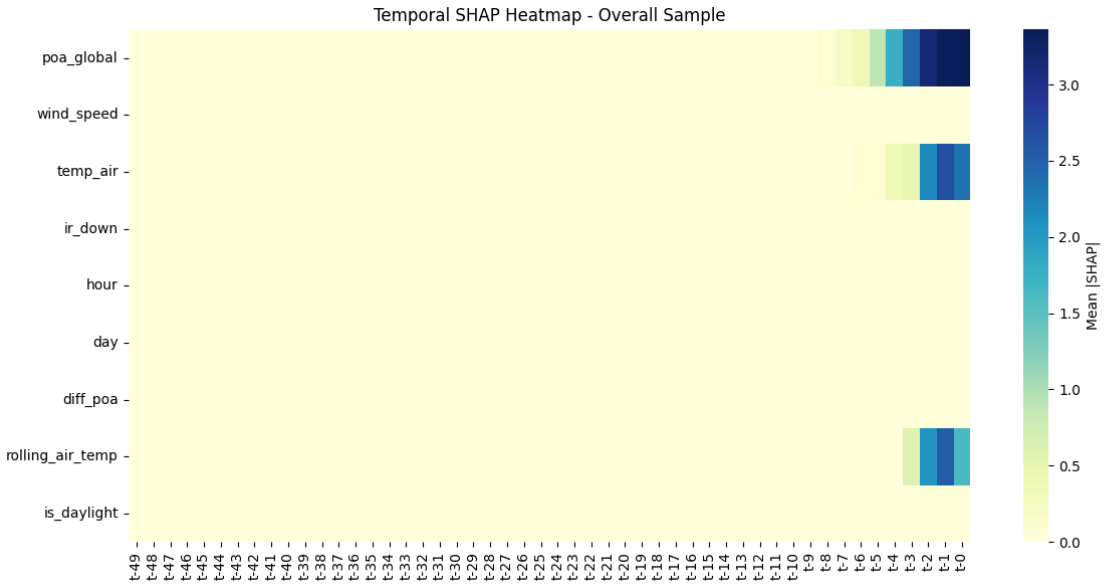

Figure 5-10: Temporal SHAP Heatmap for overall features

Overall, the SHAP analysis reinforces the physical validity of the model by highlighting that the most predictive features—*poa_global*, *temp_air*, and *rolling_air_temp*—are those most directly tied to heat transfer in PV systems. Furthermore, the LSTM model's attention to recent time steps indicates its effectiveness in learning short-term thermal memory and transient environmental behaviors, essential for accurately forecasting module temperature under dynamic operating conditions.

5.7.7 Feature Correlation Analysis

Figure 5.11 presents the Pearson correlation matrix for the engineered input features used to train the LSTM model. This analysis provides insight into how strongly the features are linearly related, both with each other and with the target variable (temp_pv), thereby helping to assess feature redundancy and multicollinearity.

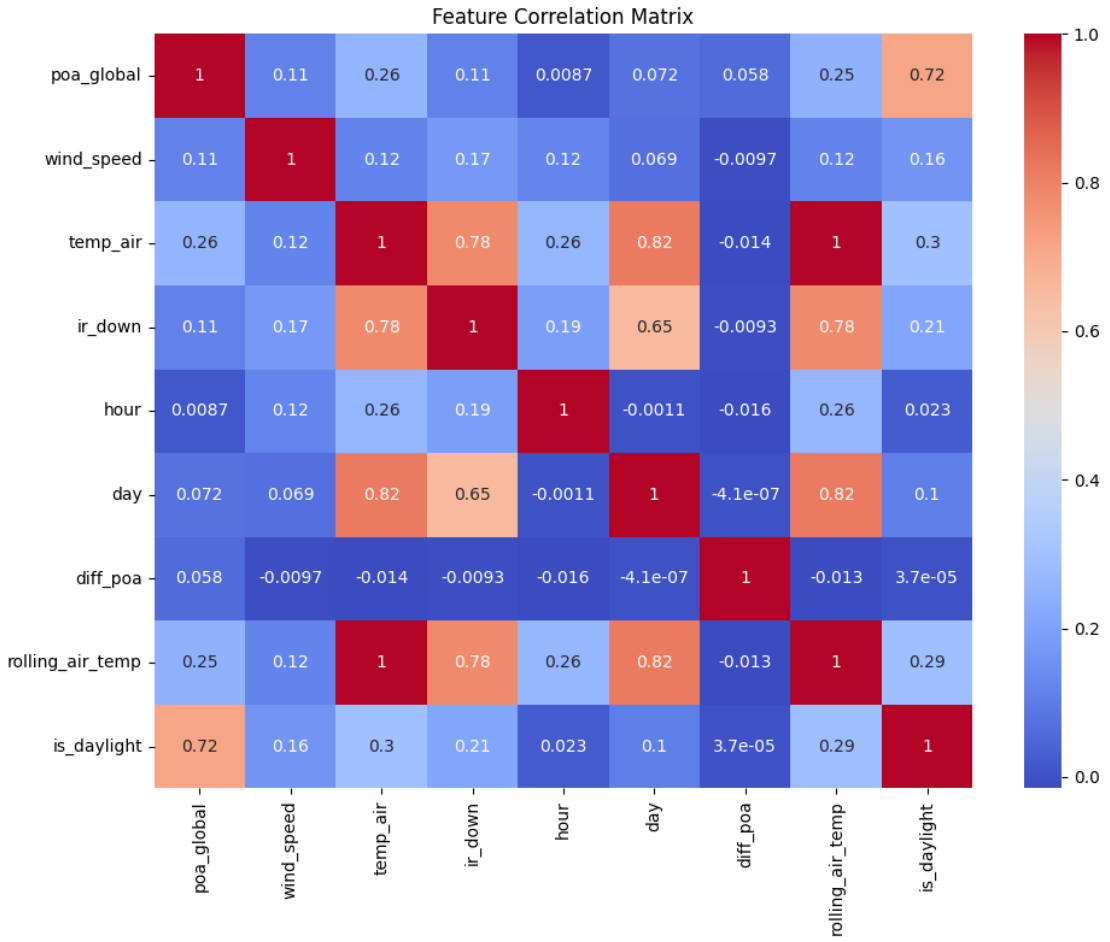

Figure 5-11: Pearson correlation matrix among different features

Figure 5.11 illustrates the Pearson correlation matrix for all engineered input features used in the LSTM model to predict PV module back-surface temperature. The correlation values help assess the degree of linear dependency among variables, supporting both feature selection and interpretability. As expected, poa_global (plane-of-array irradiance) shows strong positive correlation with is_daylight (0.72), since daylight presence is inherently tied to irradiance levels. It also demonstrates moderate correlations with temp_air (0.26) and rolling_air_temp (0.25), reflecting the thermal effect of solar radiation on the surrounding environment. A near-perfect correlation is observed between temp_air and rolling_air_temp (1.0), which is reasonable as the latter is a smoothed version of the former designed to enhance temporal learning in the LSTM network. Similarly, temp_air and ir_down show a strong correlation (0.78), highlighting the thermodynamic relationship between infrared radiation and ambient temperature. The day feature also correlates strongly with temp_air (0.82) and rolling_air_temp (0.82), indicating seasonal temperature shifts, although its low correlation with poa_global (0.072) suggests irradiance is more influenced by daily atmospheric conditions than calendar progression.

Other features contribute unique information to the model. diff_poa, representing the change in irradiance over time, has near-zero correlation with other features, validating its role in capturing

transient effects critical for modeling sudden PV temperature shifts. wind_speed is largely uncorrelated with the rest of the variables (maximum of 0.17), suggesting it contributes independent information related to convective cooling on the PV surface. Overall, the correlation analysis confirms that the selected feature set is both physically grounded and sufficiently diverse, combining stable environmental indicators with dynamic, time-sensitive attributes. This diversity enables the LSTM model to learn complex, non-linear thermal behaviors in PV modules under varying atmospheric conditions without being dominated by feature redundancy.

5.7.8 Condition-Specific Performance Evaluation

Figure 5.12 shows the performance of the lstm_seq_window50 model during peak solar hours (11:00 to 14:00), a period characterized by sustained high irradiance and rapid thermal dynamics in PV modules. The model demonstrates excellent tracking of the actual temperature trend, with minimal phase lag or amplitude deviation, yielding a Mean Absolute Error (MAE) of 0.837°C, Root Mean Squared Error (RMSE) of 1.074°C, and a coefficient of determination (R^2) of 0.994. These values confirm the model's robustness in high-energy operational windows, where rapid irradiance loading, thermal accumulation, and localized convection dominate PV thermal behavior. Despite the presence of high-frequency variability due to transient environmental inputs, the model maintains a tight alignment with ground truth, suggesting that it effectively learns the nonlinear relationships and temporal dependencies critical during this high-output window. This performance indicates the model's suitability for accurate thermal forecasting during periods when PV systems contribute significantly to grid power and temperature-based performance losses are most pronounced.

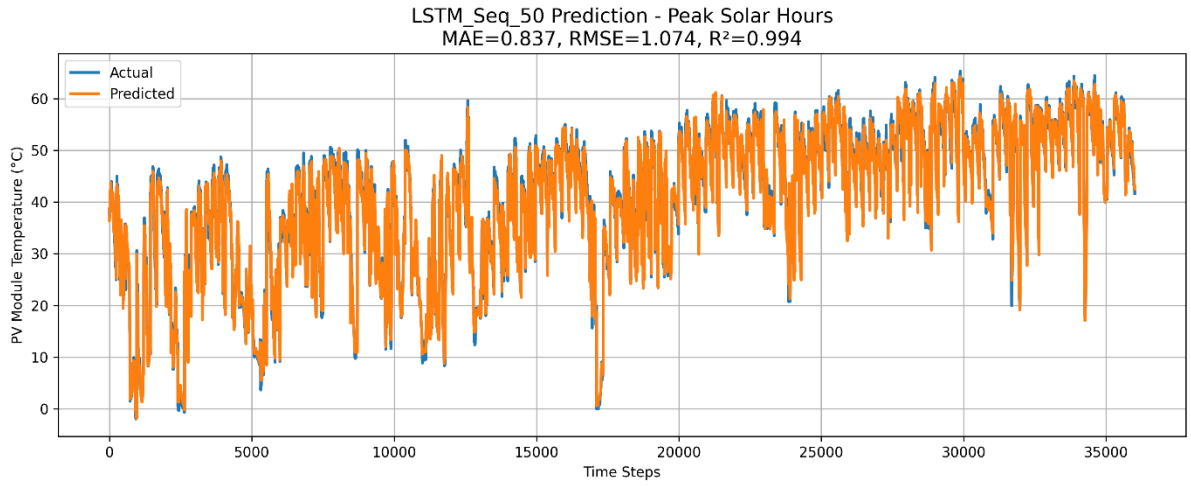

Figure 5-12: LSTM_seq_50 best performing model prediction for Peak solar hours

Figure 5.13 illustrates the performance of the lstm_seq_window50 model under high wind conditions, defined in this study as time periods when wind speed exceeded the 90th percentile, which corresponds to values greater than approximately 5.8 m/s in the dataset. These conditions represent

enhanced convective cooling scenarios, where elevated wind flow rapidly dissipates heat from the PV module surface, often decoupling temperature from irradiance levels. The model demonstrates excellent accuracy with a MAE of 0.419°C, RMSE of 0.581°C, and an R^2 of 0.998, indicating extremely close alignment with actual sensor measurements. Despite the presence of frequent and sharp thermal transitions induced by wind gusts, the model effectively captures the dynamics of both magnitude and timing. This high fidelity suggests that the LSTM architecture successfully learns the transient heat loss mechanisms driven by wind, even though wind_speed is only weakly correlated with other features. The results affirm that wind speed, although statistically independent, provides unique and essential physical information, enhancing the model's generalization under real-world, high-variability environmental conditions.

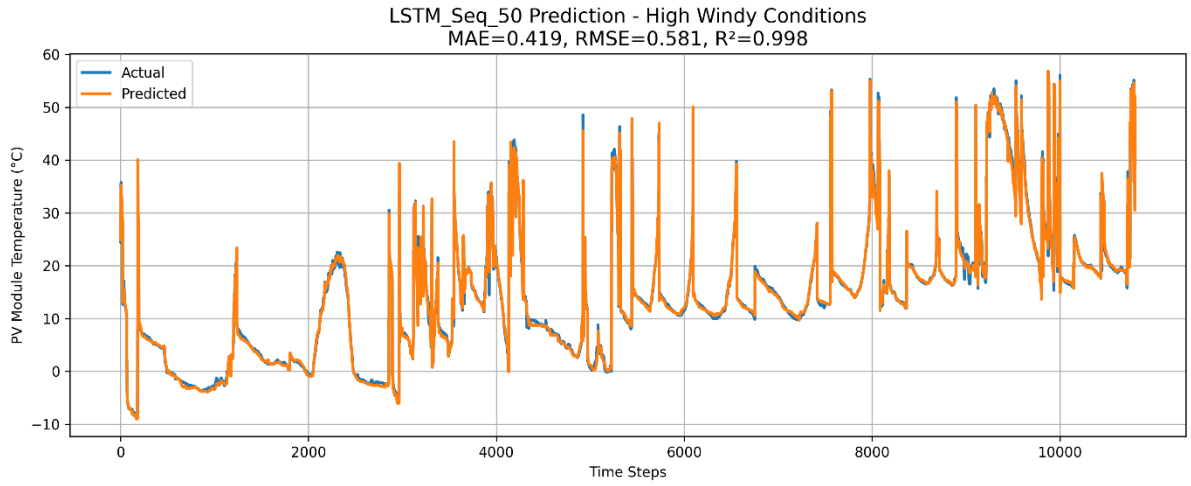

Figure 5-13: LSTM_seq_50 best performing model prediction for high windy conditions

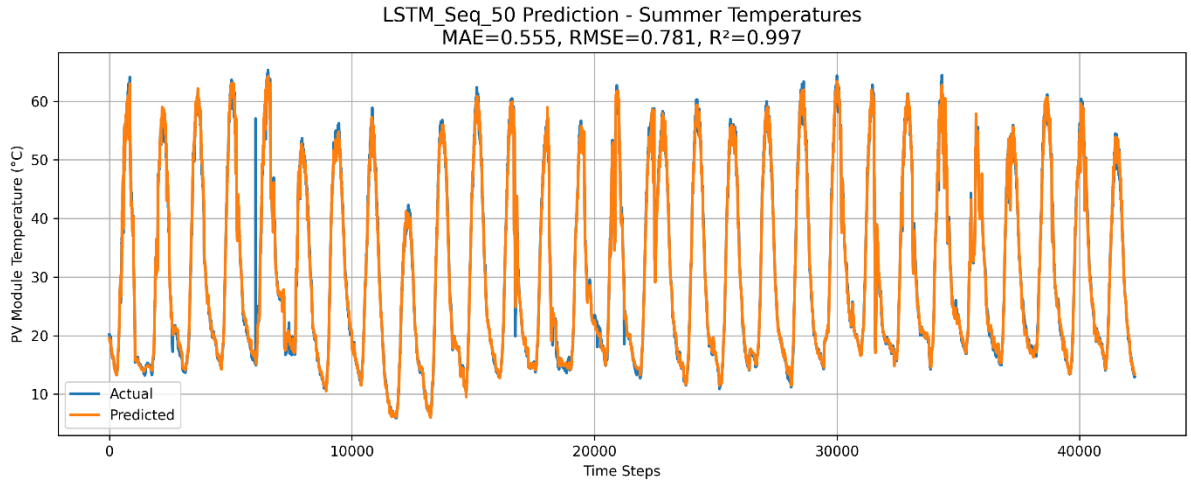

Figure 5-14: LSTM_seq_50 best performing model prediction for summer temperatures

Figure 5.14 presents the model's performance during summer months (June to July), characterized by prolonged daylight hours, high irradiance, and elevated ambient temperatures. The model achieves excellent predictive accuracy, with a Mean Absolute Error (MAE) of 0.555°C, RMSE of 0.781°C,

and a coefficient of determination (R^2) of 0.997, indicating a near-perfect fit to the actual temperature profile. The predicted and actual curves follow closely through daily thermal cycles, capturing sharp midday peaks above 60°C and early morning lows near 20°C. The consistent amplitude and timing of predictions across high-temperature days suggest that the LSTM model has successfully learned the diurnal heating and cooling patterns typical of summer, where irradiance and ambient air temperature are dominant drivers. This performance highlights the model's strength in stable, high-irradiance scenarios, which are critical for yield forecasting and thermal stress evaluation during peak solar production months.

Taken together, the results of this study demonstrate that the proposed LSTM-based deep learning architecture, particularly with a 50-time-step temporal window, delivers highly accurate and stable performance across a wide range of operational conditions. From baseline benchmarking to uncertainty estimation, and from cross-validation to targeted condition-specific evaluations, the model consistently exhibited strong alignment with measured PV module temperatures. It effectively captured both steady-state and dynamic behaviors, including thermal lags, irradiance transients, and convective cooling effects. Importantly, the model's predictive power remained robust even under complex scenarios such as high wind, cloudy transitions, and seasonal extremes, highlighting its generalization capacity and suitability for deployment in real-time PV monitoring and forecasting systems. Although the proposed LSTM framework demonstrates strong predictive performance, this study has several limitations. Because the model was trained using data from a single geographic location, its transferability to other climates requires further validation. Future work should evaluate the model across multiple PV installations with different climatic conditions, module technologies, and mounting configurations to assess its broader applicability.

5.8. Conclusion

This chapter developed and evaluated a data-driven framework for high-resolution photovoltaic module temperature prediction using long short-term memory networks, with comparison against conventional machine-learning models and established physics-based approaches. The results showed that the sequence-aware LSTM architecture consistently outperformed the non-sequential baselines in terms of predictive accuracy, demonstrating the importance of temporal memory for capturing the thermal inertia and delayed environmental response of PV modules. Trained on high-resolution real-world data, the model demonstrated exceptional predictive performance across all tested metrics (MAE: 0.621°C, RMSE: 0.863°C, R^2: 0.998), with consistent generalization across varying atmospheric scenarios. The inclusion of engineered meteorological and time-dependent features further improved the representation of dynamic operating conditions, while chronological

splitting and time-series cross-validation strengthened the methodological reliability of the evaluation.

Beyond point prediction, this chapter extended the analysis through uncertainty estimation and interpretability. Monte Carlo dropout provided a practical estimate of predictive confidence, showing that uncertainty increased during rapidly changing environmental conditions, which is physically reasonable for transient thermal regimes. SHAP-based interpretation further indicated that irradiance, ambient temperature, long-wave radiation, and temporal features play dominant roles in shaping the model response, supporting the physical plausibility of the learned relationships. Taken together, these results show that the proposed framework is not only accurate within the studied dataset, but also more informative than a purely black-box predictor.

Nevertheless, the scientific scope of the conclusions should remain aligned with the validation domain. The present framework has been rigorously tested within the available dataset and against relevant benchmark models, but its transferability to other module technologies, climates, installation geometries, and measurement ecosystems has not yet been established. Similarly, while the uncertainty and interpretability analyses improve confidence in the model behavior, they should be understood as supportive tools rather than complete guarantees of general reliability under all deployment conditions. Therefore, the principal contribution of this chapter is the demonstration of a robust, time-aware, and interpretation-supported within-dataset forecasting framework for PV module temperature, rather than a universally validated model for all operating scenarios. Future work should focus on cross-site evaluation, climate-transfer testing, and hybridization with physics-informed constraints to further improve generalizability and deployment readiness.

Chapter.6 Integrated Discussion of Optical and Thermal Strategies for Photovoltaic Performance Enhancement

6.1. Overview of the integrated research framework

The central aim of this thesis has been to examine how photovoltaic performance can be improved through complementary strategies that operate at different levels of the solar-energy system. These strategies include nanoscale spectral management through luminescent down-shifting coatings, nanoscale optical-field engineering through plasmonically coupled quantum-dot structures, and system-level thermal prediction through data-driven modeling. Although these three research directions differ in method and scale, they are unified by a common scientific objective, namely, to reduce losses that limit photovoltaic performance and to improve the utilization, management, and prediction of energy conversion processes.

Taken together, the work presented in this thesis addresses three distinct but connected dimensions of photovoltaic optimization. The first concerns the spectral mismatch between the incident solar spectrum and the wavelength-dependent response of silicon photovoltaics, particularly in the ultraviolet and blue regions where parasitic absorption and surface recombination reduce useful carrier generation. The second concerns the ability to manipulate local photonic environments in order to enhance or control radiative behavior in quantum-dot systems, which is relevant to future optical management architectures. The third concerns the thermal behavior of photovoltaic modules under dynamic environmental conditions, since operating temperature strongly affects voltage, efficiency, reliability, and long-term energy yield. In this sense, the thesis moves from photon conversion, to photon emission control, to system-level thermal intelligence.

A major strength of this body of work is that it does not treat photovoltaic improvement as a single-variable problem. Instead, it recognizes that modern PV performance is constrained by several coupled loss channels, including optical mismatch, non-radiative deactivation, front-surface parasitic effects, and temperature-driven efficiency loss. The thesis therefore contributes to a broader understanding of PV optimization by showing that meaningful performance improvements may emerge not only from absorber or junction redesign, but also from front-end optical engineering and intelligent operational prediction. At the same time, the results also show that each intervention introduces its own scientific challenges, particularly in terms of mechanism attribution, deployment relevance, and transferability of conclusions.

6.2. Relationship between the optical studies

The two optical chapters of this thesis, the luminescent down-shifting study and the plasmon-enhanced photoluminescence study, are linked by a common focus on photon management through colloidal nanomaterials. In both cases, the optical behavior of semiconductor quantum dots is modified through nanoscale interface engineering in order to improve or control their interaction with light. However, the scientific role of the two chapters is not identical.

In the LDS chapter, the primary objective was application-oriented. The study sought to improve the front-side optical response of crystalline silicon mini-modules by incorporating $CsPbBr_3$ quantum dots into a PMMA-based coating, and by evaluating whether surface modification through silane or silica-related treatment could improve optical quality and translate into measurable device-level performance gains. The chapter therefore sits close to the device-application end of the research spectrum. It combines optical characterization with module electrical measurements and asks whether the engineered nanomaterial can function as a practically useful spectral management layer.

In contrast, the plasmonics chapter is more fundamentally mechanistic. Its main goal was to understand how the optical response of CdSe/CdS quantum-dot films can be altered through proximity to Au nanoparticles, and how spacer thickness controls the balance between enhancement and quenching. Rather than directly measuring photovoltaic output, this chapter focuses on a controlled structure-property relationship in a hybrid nanophotonic system. It provides insight into how local electromagnetic environments can be engineered to modify luminescence behavior, which is an enabling concept for future light-management architectures.

The integrated scientific value of placing these chapters together lies in the fact that both address the design of optically active nanostructures, but at different stages of technological maturity. The LDS chapter investigates a coating strategy already interfaced with a silicon photovoltaic platform, while the plasmonics chapter investigates a more fundamental route to manipulating emission efficiency and local optical fields. One chapter therefore emphasizes immediate application potential, while the other emphasizes mechanistic understanding and future design logic. Their combination strengthens the thesis because it shows both translational intent and nanophotonic depth.

6.3. Interpretation of the LDS findings in a broader scientific context

The results of the LDS chapter suggest that PMMA-integrated $CsPbBr_3$ quantum dots, particularly after surface modification, can produce measurable improvements in the performance of crystalline silicon mini-modules. The optical characterization indicated that surface treatment improved the emission characteristics of the quantum dots, consistent with a reduction in non-radiative losses and a more favorable emissive environment. Device results further showed that the best performance was

obtained at intermediate quantum-dot and polymer concentrations, while excessive loading reduced the benefit. This pattern is scientifically important because it supports a physically realistic picture of luminescent coating behavior.

The non-monotonic trend observed across loading compositions is consistent with the competing processes expected in LDS systems. At moderate loading, the coating can absorb part of the high-energy incident flux and re-emit at wavelengths that are more effectively utilized by silicon, while maintaining sufficient transparency for the rest of the solar spectrum. However, as the concentration increases, detrimental effects such as self-absorption, parasitic attenuation, scattering, and reduced transmittance become increasingly important. The existence of an optimum therefore supports the view that the coating is operating within a genuine trade-off space rather than producing artificially inflated gains.

At the same time, the integrated discussion must remain scientifically cautious. The current evidence supports the interpretation that the observed gains are compatible with LDS-assisted performance enhancement, but it does not fully isolate luminescent down-shifting as the sole or dominant mechanism. Front-surface coatings can also modify reflection, angular scattering, and optical path distribution, and these effects may contribute to changes in measured current and efficiency. Without wavelength-resolved external quantum efficiency measurements, full film-state optical accounting, and a clearer correlation between absorption, emission, and device spectral response, complete causal attribution remains open. This does not invalidate the chapter, but it does define the proper scientific scope of its conclusions.

Another important point concerns materials relevance. The use of surface-modified perovskite quantum dots within a polymer host addresses a real challenge in the LDS literature, namely, how to maintain optical quality after film formation and integration onto device-relevant surfaces. In this sense, the chapter contributes meaningfully to interface engineering for spectral converters. However, the absence of long-duration environmental validation means that the work should still be interpreted as a proof-of-concept coating study rather than a finalized module technology. The integrated conclusion from this chapter is therefore that surface-passivated perovskite quantum dots offer a credible route toward LDS-oriented optical coatings, but that full validation must still include spectral attribution and durability testing under module-relevant stress conditions.

6.4. Interpretation of the plasmonic photoluminescence findings in a broader scientific context

The plasmonics chapter contributes a different but complementary form of optical insight. The study demonstrates that the photoluminescence response of CdSe/CdS quantum-dot films can be modulated

through the presence of Au nanoparticles and that dielectric separation is a critical control parameter. The observed transition from quenching at short distances to enhancement at optimized spacing is fully consistent with the known competition between metal-induced non-radiative decay and beneficial near-field interactions. This confirms that nanoscale architecture, rather than simple material juxtaposition, determines whether plasmonic coupling is beneficial or detrimental.

Scientifically, the most significant outcome of this chapter is not merely the observation of enhanced emission, but the clarification of the structural regime in which enhancement becomes possible. This is valuable because plasmonic systems are frequently overinterpreted on the basis of intensity changes alone. In contrast, the present work identifies the importance of geometry and interprets the results through a physically grounded framework of distance-dependent coupling. The chapter therefore provides a useful mechanistic basis for future hybrid photonic design.

However, the integrated scientific discussion also needs to acknowledge the limits of this evidence. A measured increase in photoluminescence does not by itself distinguish among several possible mechanisms, including excitation-rate enhancement, modified radiative decay, improved extraction, or scattering-assisted outcoupling. The present work provides strong evidence for plasmonically modulated optical behavior, but not full discrimination of the underlying rate processes. For that reason, the chapter is strongest when framed as a controlled study of luminescence modulation rather than definitive proof of a pure Purcell-driven process.

In the context of the thesis as a whole, the plasmonic chapter plays an important conceptual role. It expands the photon-management theme beyond passive spectral conversion and into active control of the local optical environment. While it does not yet demonstrate direct photovoltaic enhancement, it establishes design principles that may become relevant for next-generation optical interfaces, emitters, or photonic coupling layers. Thus, its contribution is enabling rather than directly device-validating. This distinction should be maintained clearly in the integrated narrative.

6.5. Comparison of the two optical strategies

When viewed together, the LDS and plasmonic chapters highlight two different scientific philosophies of photon management. The LDS approach is designed to improve the spectral compatibility between incident solar photons and the electronic response of the cell. It acts at the scale of solar-spectrum conditioning and seeks to redirect unusable or poorly utilized photons into a more favorable spectral range. By contrast, the plasmonic approach acts at the scale of the local electromagnetic environment around the emitter. It seeks to modify the probability, efficiency, or extraction pathway of radiative processes through nanoscale field engineering.

These strategies differ not only in mechanism but also in readiness level. LDS coatings can be deposited on device surfaces and assessed through electrical performance measurements, making them relatively close to translational photovoltaic application. Plasmonic emitter coupling, in the present form, remains a more exploratory nanophotonic strategy. Its immediate value lies in mechanistic understanding and in future architectural inspiration rather than direct deployment. Nevertheless, the two approaches share a common lesson, namely, that nanomaterial performance in photovoltaics depends not only on the intrinsic optical properties of the active species, but also on its environment, interfaces, and spatial organization.

A further shared outcome is that improvement is conditional, not automatic. In both chapters, optimization is essential. Increased quantum-dot loading is not always beneficial in LDS coatings, just as reduced emitter-metal distance is not always beneficial in plasmonic systems. The best performance arises from carefully balanced conditions that minimize one loss pathway without amplifying another. This reinforces a broader scientific message of the thesis, which is that advanced optical materials can improve photovoltaic-relevant behavior only when integrated with attention to competing transport, reabsorption, dissipation, and parasitic optical effects.

6.6. Integration of the thermal prediction study with the optical performance study

At first glance, the thermal prediction chapter differs substantially from the two optical chapters because it is based on data science rather than materials synthesis and spectroscopy. However, it addresses an equally important aspect of photovoltaic performance. While the optical chapters aim to improve how photons are converted or managed before carrier extraction, the thermal chapter focuses on how module operating conditions influence electrical behavior after illumination. Module temperature strongly affects open-circuit voltage, fill factor, and long-term reliability, making thermal behavior a system-level constraint on practically achievable performance.

The LSTM-based modeling framework developed in this thesis shows that temporal information is essential for accurate prediction of PV module temperature. This is scientifically significant because module temperature is not determined solely by instantaneous weather conditions, but by thermal inertia, delayed radiative exchange, and changing environmental histories. The superior performance of the sequence-based model over static baselines therefore supports the physical interpretation that temporal memory is inherent to the thermal dynamics of PV systems. The addition of uncertainty and SHAP-based analyses further strengthens the chapter by improving transparency around the model's behavior.

The deeper connection to the optical chapters lies in the fact that both optical management and thermal management are ultimately concerned with reducing non-ideal operating losses. A spectral converter

aims to deliver a more useful photon distribution to the absorber. A temperature predictor aims to anticipate operating conditions that degrade efficiency or threaten reliable operation. One acts before conversion and the other monitors consequences during operation, but both serve the same broader goal of improving photovoltaic performance through scientifically informed intervention.

At the same time, the integrated thesis must honestly recognize that this relationship remains conceptual rather than experimentally coupled. The thermal model was not trained on modules modified by the optical coatings, and the optical chapters did not include thermal feedback analysis. Thus, while the thematic integration is strong, the system-level coupling has not yet been closed experimentally. This is an important distinction. The thesis should therefore present its integration as a coherent research program on PV optimization across scales, rather than as a single fully coupled platform. Such framing is scientifically accurate and still intellectually compelling.

6.7. Cross-cutting scientific contributions of the thesis

Several broader scientific contributions emerge when the three research strands are considered together.

First, the thesis shows that nanoscale interface engineering is central to photovoltaic materials innovation. In the LDS chapter, surface chemistry and polymer integration determine whether the quantum dots retain useful optical behavior after film formation. In the plasmonic chapter, dielectric spacing and structural separation determine whether metal coupling is beneficial or harmful. In both cases, interfaces govern performance as much as the active nanomaterial itself.

Second, the thesis demonstrates that performance enhancement must be interpreted through trade-offs rather than isolated improvements. A stronger emitter is not necessarily a better coating if transparency is sacrificed. A closer plasmonic partner is not necessarily beneficial if quenching dominates. A more accurate predictive model is not necessarily more useful if its uncertainty and transferability are unknown. This repeated pattern across all chapters gives the thesis scientific coherence and maturity.

Third, the thesis advances the idea that modern photovoltaic optimization must operate across multiple scales. Materials-level control, nanoscale optical design, and system-level predictive modeling are often treated as separate research domains, yet they address related efficiency and reliability limits. By combining these scales within one body of work, the thesis argues for a more integrated view of PV research, where frontier improvements emerge not only from cell architecture, but also from optical conditioning, interfacial photonics, and operational intelligence.

Fourth, the work emphasizes that scientific credibility depends on validation depth. Each chapter includes positive findings, but each also reveals the importance of careful interpretation. In the optical

chapters, mechanism attribution remains a central requirement. In the thermal chapter, transferability and calibration remain the key tests of broader reliability. This consistency in scientific self-evaluation strengthens the thesis because it demonstrates that the contribution is not built on overstatement.

6.8. Main limitations across the thesis

Although the thesis presents meaningful and original contributions, several limitations remain when the work is viewed as an integrated scientific whole.

The first limitation concerns mechanistic closure in the optical chapters. The LDS results are consistent with luminescent down-shifting assisted performance enhancement, but the present evidence does not fully separate this effect from antireflection, scattering, or other front-optical contributions. Likewise, the plasmonic chapter demonstrates distance-dependent modulation of emission, but does not completely distinguish among the possible rate and extraction mechanisms responsible for the observed enhancement. In both cases, the interpretations are scientifically plausible and supported, but not fully closed.

The second limitation concerns deployment readiness. The LDS chapter demonstrates proof-of-concept functionality of a surface-modified quantum-dot coating, but does not yet establish long-term environmental durability under realistic module operating conditions. The plasmonic chapter is even earlier in maturity because it remains an optical structure-property study without direct device integration. Thus, the optical advances are scientifically meaningful, but still positioned before full technological validation.

The third limitation concerns external generalization in the predictive modeling work. The LSTM framework is rigorously evaluated within the available dataset, and the methodology is considerably stronger than many simple train-test demonstrations. However, validation within one measurement ecosystem does not establish full transferability to other climates, mounting configurations, technologies, or sensor conditions. The uncertainty and interpretability analyses improve confidence, but they do not eliminate the need for broader deployment-oriented validation.

The fourth limitation concerns the level of coupling among the thesis components. The work is integrated conceptually, but not experimentally or computationally across chapters. For example, the optical modifications were not propagated into thermal or energy-yield modeling, and the predictive framework was not extended to modules bearing the studied coatings. As a result, the thesis presents a coherent multi-scale program, but not yet a closed, end-to-end photovoltaic optimization pipeline.

6.9. Future directions emerging from the integrated work

These limitations also identify the natural next steps of the research program. For the LDS work, future studies should focus on spectral attribution through external quantum efficiency measurements,

film-state photoluminescence quantum yield, angular and optical-transmission analyses, and long-duration environmental stability testing under ultraviolet, humidity, and thermal stress. Such work would transform the present coating concept from a promising optical proof-of-concept into a more deployment-relevant photovoltaic technology.

For the plasmonic work, future efforts should include comprehensive time-resolved spectroscopy, angle-dependent optical studies, and integration into device-relevant architectures where net energy or carrier-generation benefit can be assessed directly. This would help determine whether the observed luminescence enhancement can be translated into practical photonic advantage without incurring metal-related parasitic losses.

For the thermal modeling work, future research should emphasize cross-site and cross-climate validation, domain transfer, and physics-informed model design. These steps are essential if the framework is to move from strong within-dataset prediction toward generalized deployment in diverse PV systems. Coupling uncertainty quantification with operational decision metrics would also improve relevance for real-world control and diagnostics.

At the program level, one particularly promising direction would be to link these domains more explicitly. Optical coatings that alter front-surface absorption, reflection, or thermal loading could be incorporated into energy-yield and thermal simulations, while predictive models could be trained to capture the thermal consequences of optically modified modules. Such integration would create a more complete understanding of how nanoscale optical interventions influence module-scale performance over time.

6.10. Final integrated perspective

In integrated terms, the thesis shows that improving photovoltaic systems requires attention not only to absorber physics, but also to how light is conditioned, how emission is controlled, and how operating conditions are predicted. The work demonstrates that colloidal quantum dots can be engineered to provide useful optical functions, that plasmonic structures can modulate emissive behavior in a controllable manner, and that time-aware machine learning can capture thermal dynamics more effectively than static models. These contributions operate at different scales, yet all address the broader challenge of extracting more reliable and useful performance from photovoltaic systems.

At the same time, the thesis also shows that credible advancement in photovoltaics depends on disciplined scientific interpretation. Optical gains must be attributed carefully, mechanistic claims must remain proportional to the evidence, and predictive models must be judged by their generalization limits as well as their in-sample accuracy. In this sense, the thesis contributes not only

specific results, but also a methodological position, namely, that multi-scale photovoltaic innovation must combine creative engineering with rigorous validation.

Chapter.7 Conclusion

7.1. Overall conclusion

This thesis investigated complementary strategies for improving photovoltaic performance through nanoscale optical engineering and data-driven thermal prediction. The work focused on three research directions: luminescent down-shifting coatings based on perovskite quantum dots for crystalline silicon mini-modules, plasmonically modulated photoluminescence in hybrid quantum-dot and gold nanoparticle structures, and high-resolution photovoltaic module temperature prediction using long short-term memory networks. Although these topics differ in material platform, methodology, and scale, they are unified by the aim of reducing losses and improving the functional efficiency of photovoltaic systems.

The thesis first demonstrated that $CsPbBr_3$ quantum dots can be incorporated into PMMA-based front-side coatings for silicon mini-modules and that surface modification improves their optical behavior and device-level performance trends. The best-performing coatings were obtained at intermediate compositions, confirming that the benefit of spectral conversion depends on balancing emission efficiency with optical transparency and minimizing parasitic losses. These results establish surface-passivated perovskite quantum dots as promising materials for LDS-oriented photovoltaic coatings. At the same time, the work also shows that full attribution of the observed gains requires additional spectral validation and that long-term environmental durability remains a key requirement for practical deployment.

The thesis next showed that the emission behavior of CdSe/CdS quantum-dot films can be modulated in a controlled manner through coupling with Au nanoparticles and by tuning dielectric spacer thickness. The observed transition between quenching and enhancement confirms the importance of nanoscale geometry in determining the optical outcome of plasmonic coupling. This chapter therefore provides a mechanistic contribution to the design of hybrid nanophotonic structures based on colloidal emitters. However, the present evidence most strongly supports the conclusion of distance-dependent plasmonic modulation of luminescence, rather than complete proof of a single underlying enhancement mechanism or direct photovoltaic benefit.

Finally, the thesis demonstrated that LSTM-based sequence modeling provides accurate and physically meaningful prediction of photovoltaic module temperature when trained on high-resolution environmental data. The temporal nature of the model allowed it to outperform non-sequential baselines, highlighting the importance of thermal memory and delayed environmental response in PV operation. The inclusion of uncertainty estimation and SHAP-based interpretation further strengthened the scientific quality of the framework by improving transparency and diagnostic

value. Nevertheless, the model's conclusions are most robust within the studied dataset, and broader transferability across climates, technologies, and deployment conditions remains to be established.

7.2. Main scientific contributions

The first major contribution of this thesis is the development and evaluation of surface-modified perovskite quantum-dot coatings for silicon photovoltaics within a polymer-integrated architecture. This work adds to the growing field of spectral conversion by demonstrating that interfacial passivation and matrix integration are central to obtaining meaningful optical and electrical outcomes.

The second major contribution is the clarification of spacer-dependent plasmonic effects in hybrid quantum-dot films. By showing that nanoscale separation determines whether coupling is beneficial or detrimental, the work provides a useful design framework for future photonic interfaces involving colloidal emitters and metallic nanostructures.

The third major contribution is the construction of a time-aware, interpretation-supported machine-learning framework for PV module thermal prediction. The use of chronological validation, comparison with benchmark models, uncertainty quantification, and explainability distinguishes this work from simpler purely predictive studies and improves its scientific credibility.

More broadly, the thesis contributes a multi-scale perspective on photovoltaic enhancement. It shows that meaningful performance gains may emerge through spectral management, local optical-field engineering, and intelligent operational prediction, and that these approaches should be viewed as complementary rather than isolated.

7.3. Scientific limitations and careful scope of the conclusions

A consistent message throughout this thesis is that the interpretation of improvement must remain aligned with the strength of the evidence. In the LDS chapter, the observed module gains are consistent with luminescent down-shifting assisted enhancement, but the present data do not fully isolate luminescent conversion from other front-optical effects such as reflection change or scattering. In the plasmonic chapter, the results demonstrate controllable emission modulation, but do not fully close the distinction among radiative-rate modification, excitation effects, and extraction-related contributions. In the thermal chapter, the predictive framework is robust within the studied dataset, but wider transferability remains an open question.

These limitations do not diminish the scientific value of the work, but they define its correct scope. The thesis therefore does not claim to have established a fully deployment-ready spectral-conversion technology, a complete mechanistic closure of plasmonic enhancement pathways, or a universally validated thermal prediction model. Instead, it presents three scientifically sound and complementary

contributions that advance photovoltaic research while also identifying the key validation steps needed for further progress.

7.4. Final perspective

The overall conclusion of this thesis is that photovoltaic improvement can be pursued effectively through coordinated advances in photon management and operational intelligence. Surface-engineered quantum dots can enhance the optical functionality of front-side coatings, nanoscale plasmonic architecture can tune emissive behavior in hybrid nanostructures, and sequence-aware machine learning can improve the prediction of thermally driven performance constraints. Each of these approaches addresses a different loss channel, and together they point toward a broader model of photovoltaic innovation in which materials engineering, nanophotonics, and predictive analytics work in concert.

At the same time, the thesis also shows that scientific progress in this field depends on rigorous validation and careful claim discipline. Mechanism attribution, stability assessment, and transferability testing remain essential if laboratory-level advances are to translate into durable photovoltaic benefit. For this reason, the most important outcome of the thesis is not only the specific results obtained, but also the research direction it defines, a multi-scale, evidence-aware pathway for improving photovoltaic systems through both engineered optical functionality and intelligent operational modeling.

References

[1] M. Victoria *et al.*, "Solar photovoltaics is ready to power a sustainable future," *Joule*, vol. 5, no. 5, pp. 1041–1056, May 2021, doi: 10.1016/j.joule.2021.03.005.

[2] S. Ahmed, A. Ali, J. A. Ansari, S. A. Qadir, and L. Kumar, "A Comprehensive Review of Solar Photovoltaic Systems: Scope, Technologies, Applications, Progress, Challenges, and Recommendations," *IEEE Access*, vol. 13, pp. 69723–69750, 2025, doi: 10.1109/ACCESS.2025.3558539.

[3] Q. Wang *et al.*, "Electrical Performance, Loss Analysis, and Efficiency Potential of Industrial-Type PERC, TOPCon, and SHJ Solar Cells: A Comparative Study," *Prog. Photovolt. Res. Appl.*, vol. 32, no. 12, pp. 889–903, Dec. 2024, doi: 10.1002/PIP.3839;REQUESTEDJOURNAL:JOURNAL:1099159X;PAGE:STRING:ARTICLE/CHAPTER.

[4] H. Lin *et al.*, "Silicon heterojunction solar cells with up to 26.81% efficiency achieved by electrically optimized nanocrystalline-silicon hole contact layers," *Nat. Energy 2023 88*, vol. 8, no. 8, pp. 789–799, May 2023, doi: 10.1038/s41560-023-01255-2.

[5] M. J. Hossain, M. Sun, and K. O. Davis, "Photon management in silicon photovoltaic cells: A critical review," *Sol. Energy Mater. Sol. Cells*, vol. 267, p. 112715, Apr. 2024, doi: 10.1016/J.SOLMAT.2024.112715.

[6] L. C. Andreani, A. Bozzola, P. Kowalczewski, M. Liscidini, and L. Redorici, "Silicon solar cells: toward the efficiency limits," *Adv. Phys. X*, vol. 4, no. 1, p. 1548305, Jan. 2019, doi: 10.1080/23746149.2018.1548305.

[7] A. Richter *et al.*, "Design rules for high-efficiency both-sides-contacted silicon solar cells with balanced charge carrier transport and recombination losses," *Nat. Energy 2021 64*, vol. 6, no. 4, pp. 429–438, Apr. 2021, doi: 10.1038/s41560-021-00805-w.

[8] S. Garshasbi, S. Huang, J. Valenta, and M. Santamouris, "Enhancing the cooling potential of photoluminescent materials through evaluation of thermal and transmission loss mechanisms," *Sci. Rep. 2021 111*, vol. 11, no. 1, pp. 14725-, Jul. 2021, doi: 10.1038/s41598-021-94354-7.

[9] T. Yatsui and T. Yatsui, "Recent improvement of silicon absorption in opto-electric devices," *Opto-Electron. Adv. 2019 Vol 2 Issue 10 Pages 190023-1-190023-8*, vol. 2, no. 10, pp. 190023–1, Oct. 2019, doi: 10.29026/OEA.2019.190023.

[10] Z. Wu *et al.*, "A review of spectral controlling for renewable energy harvesting and conserving," *Mater. Today Phys.*, vol. 18, p. 100388, May 2021, doi: 10.1016/J.MTPHYS.2021.100388.

[11] R. Williams and A. Farawar, "Perovskite Solar Cells: Stability, design architecture, photophysical properties, and morphology of the film in organometal halide Perovskite--based Photovoltaics," 2016. doi: 10.13140/RG.2.1.1406.8242.

[12] S. S. Kharintsev *et al.*, "Photon Momentum Enabled Light Absorption in Silicon," *ACS Nano*, vol. 18, no. 39, pp. 26532–26540, Oct. 2024, doi: 10.1021/ACSNANO.4C02656.

[13] A. Sinha *et al.*, "UV-induced degradation of high-efficiency silicon PV modules with different cell architectures," *Prog. Photovolt. Res. Appl.*, vol. 31, no. 1, pp. 36–51, Jan. 2023, doi: 10.1002/PIP.3606;WEBSITE:WEBSITE:PERICLES;JOURNAL:JOURNAL:1099159X;WGROUP:STRING:PUBLICATION.

[14] J. Day, S. Senthilarasu, and T. K. Mallick, "Improving spectral modification for applications in solar cells: A review," *Renew. Energy*, vol. 132, pp. 186–205, Mar. 2019, doi: 10.1016/J.RENENE.2018.07.101.

[15] Y.-M. S. ; ; Huang *et al.*, "Recent Advances in Colloidal Quantum Dots or Perovskite Quantum Dots as a Luminescent Downshifting Layer Embedded on Solar Cells," *Nanomater. 2022 Vol 12 Page 985*, vol. 12, no. 6, p. 985, Mar. 2022, doi: 10.3390/NANO12060985.

[16] C. Q. Wang, C. Wen, B. Li, M. Chen, Y. Ren, and Q. Y. Dai, "Parasitic absorption of zinc oxide as a transparent conductive oxide layer for silicon heterojunction solar cells," *Phys. B Condens. Matter*, vol. 715, p. 417594, Oct. 2025, doi: 10.1016/J.PHYSB.2025.417594.

[17] Y. C. Kim *et al.*, “Luminescent down-shifting CsPbBr3 perovskite nanocrystals for flexible Cu(In,Ga)Se2 solar cells,” *Nanoscale*, vol. 12, no. 2, pp. 558–562, Jan. 2020, doi: 10.1039/C9NR06041C.
[18] G. S. Kinsey *et al.*, “Impact of measured spectrum variation on solar photovoltaic efficiencies worldwide,” *Renew. Energy*, vol. 196, pp. 995–1016, Aug. 2022, doi: 10.1016/J.RENENE.2022.07.011.
[19] M. Maoz, Z. Abbas, S. A. B. Shah, and V. Lughi, “Recent Advances in Flexible Solar Cells; Materials, Fabrication, and Commercialization,” *Sustain. 2025 Vol 17 Page 1820*, vol. 17, no. 5, p. 1820, Feb. 2025, doi: 10.3390/SU17051820.
[20] A. Singh, A. Srivastava, J. A. K. Satrughna, S. M. Rajore, A. R. Kanwade, and P. M. Shirage, “Spectral accessibility tuning through perovskite quantum dots for up-/down-converting photovoltaic applications: a review,” *Nanoscale*, vol. 17, no. 47, pp. 27111–27150, Dec. 2025, doi: 10.1039/D5NR02712H.
[21] A. W. Achtstein *et al.*, “Impact of Shell Growth on Recombination Dynamics and Exciton–Phonon Interaction in CdSe–CdS Core–Shell Nanoplatelets,” *ACS Nano*, vol. 12, no. 9, pp. 9476–9483, Sep. 2018, doi: 10.1021/ACSNANO.8B04803.
[22] E. Buitrago, A. M. Novello, and T. Meyer, “Third-Generation Solar Cells: Toxicity and Risk of Exposure,” *Helv. Chim. Acta*, vol. 103, no. 9, p. e2000074, Sep. 2020, doi: 10.1002/HLCA.202000074;WEBSITE:WEBSITE:PERICLES;JOURNAL:JOURNAL:15222675;ISSUE:ISSUE:DOI.
[23] J. Chen, D. Liu, M. J. Al-Marri, L. Nuuttila, H. Lehtivuori, and K. Zheng, “Photo-stability of CsPbBr3 perovskite quantum dots for optoelectronic application,” *Sci. China Mater. 2016 599*, vol. 59, no. 9, pp. 719–727, Sep. 2016, doi: 10.1007/S40843-016-5123-1.
[24] J. Wang *et al.*, “Improvement of the Stability and Optical Properties of CsPbBr3 QDs,” *Nanomater. 2023 Vol 13 Page 2372*, vol. 13, no. 16, p. 2372, Aug. 2023, doi: 10.3390/nano13162372.
[25] M. Albaladejo-Siguan, E. C. Baird, D. Becker-Koch, Y. Li, A. L. Rogach, and Y. Vaynzof, “Stability of Quantum Dot Solar Cells: A Matter of (Life)Time,” *Adv. Energy Mater.*, vol. 11, no. 12, p. 2003457, Mar. 2021, doi: 10.1002/AENM.202003457;ISSUE:ISSUE:DOI.
[26] S. Kasani, K. Curtin, and N. Wu, “A review of 2D and 3D plasmonic nanostructure array patterns: fabrication, light management and sensing applications,” *Nanophotonics*, vol. 8, no. 12, pp. 2065–2089, Jun. 2019, doi: 10.1515/NANOPH-2019-0158;ISSUE:ISSUE:DOI.
[27] P. A. D. Gonçalves, T. Christensen, N. Rivera, A. P. Jauho, N. A. Mortensen, and M. Soljačić, “Plasmon–emitter interactions at the nanoscale,” *Nat. Commun. 2020 111*, vol. 11, no. 1, pp. 366-, Jan. 2020, doi: 10.1038/s41467-019-13820-z.
[28] H. Wang *et al.*, “Controllable photoluminescence enhancement of CdTe/CdS quantum dots thin films incorporation with Au nanoparticles,” *Nanoscale Res. Lett. 2015 101*, vol. 10, no. 1, pp. 128-, Mar. 2015, doi: 10.1186/S11671-015-0833-3.
[29] A. Perveen *et al.*, “Sputtered gold nanoparticles enhanced quantum dot light-emitting diodes*,” *Chin. Phys. B*, vol. 27, no. 8, p. 086101, Aug. 2018, doi: 10.1088/1674-1056/27/8/086101.
[30] A. Azam *et al.*, “Quantum Dots-Enabled Downshifting and Downconversion Strategies for Enhanced Photovoltaics,” *ACS Nano*, vol. 19, no. 32, pp. 28969–28991, Aug. 2025, doi: 10.1021/ACSNANO.5C04988.
[31] M. P. Bakht, M. N. H. Mohd, B. S. K. K. Ibrahim, N. Khan, U. U. Sheikh, and A. A. H. A. Rahman, “Advanced automated machine learning framework for photovoltaic power output prediction using environmental parameters and SHAP interpretability,” *Results Eng.*, vol. 25, p. 103838, Mar. 2025, doi: 10.1016/J.RINENG.2024.103838.
[32] M. Gupta, A. Arya, U. Varshney, J. Mittal, and A. Tomar, “A review of PV power forecasting using machine learning techniques,” *Prog. Eng. Sci.*, vol. 2, no. 1, p. 100058, Mar. 2025, doi: 10.1016/J.PES.2025.100058.

[33] L. Yang and X. Fu, “A Review of Photovoltaic Uncertainty Modeling Based on Statistical Relational AI,” *Energ. 2026 Vol 19 Page 1509*, vol. 19, no. 6, p. 1509, Mar. 2026, doi: 10.3390/EN19061509.
[34] E. H. Sepúlveda-Oviedo, “A review of operational factors affecting photovoltaic system performance,” *Energy Convers. Manag. X*, vol. 26, p. 100942, Apr. 2025, doi: 10.1016/J.ECMX.2025.100942.
[35] A. Keddouda *et al.*, “Photovoltaic module temperature prediction using various machine learning algorithms: Performance evaluation,” *Appl. Energy*, vol. 363, p. 123064, Jun. 2024, doi: 10.1016/J.APENERGY.2024.123064.
[36] Y. Li, J. Yu, J. Li, Y. Wang, and B. Sun, “Critical Factors and Equilibrium Analysis of Luminescent Down-Shifting Process for Silicon Heterojunction Solar Cells,” *Adv. Energy Mater.*, vol. 15, no. 24, p. 2405918, Jun. 2025, doi: 10.1002/aenm.202405918.
[37] H. Chen *et al.*, “Highly luminescent AgInGaS2/AgGaS2 quantum dots as luminescent down-shifting layers for crystalline silicon solar cells with enhanced photovoltaic performance,” *J. Power Sources*, vol. 658, p. 238361, Dec. 2025, doi: 10.1016/J.JPOWSOUR.2025.238361.
[38] C. Pang, R. Li, X. Wang, W. Kong, and F. Chen, “Engineering Localized Surface Plasmon Resonance of Nanoparticles in Transparent Materials for Advanced Optical Applications,” *Laser Photonics Rev.*, p. e02571, 2026, doi: 10.1002/LPOR.202502571;WEBSITE:WEBSITE:PERICLES;JOURNAL:JOURNAL:18638899;WGROUP:STRING:PUBLICATION.
[39] P. Li *et al.*, “Advancing photovoltaic panel temperature forecasting: A comparative study of numerical simulation and machine learning in two types of PV power plant,” *Renew. Energy*, vol. 237, p. 121602, Dec. 2024, doi: 10.1016/J.RENENE.2024.121602.
[40] “Photovoltaics Equipment International Technology Roadmap for Photovoltaics (ITRPV) 2023 Results”.
[41] S. P. Muduli and P. Kale, “State-of-the-art passivation strategies of c-Si for photovoltaic applications: A review,” *Mater. Sci. Semicond. Process.*, vol. 154, p. 107202, Feb. 2023, doi: 10.1016/J.MSSP.2022.107202.
[42] R. A. M. Lameirinhas, J. P. N. Torres, and J. P. de M. Cunha, “A Photovoltaic Technology Review: History, Fundamentals and Applications,” *Energ. 2022 Vol 15 Page 1823*, vol. 15, no. 5, p. 1823, Mar. 2022, doi: 10.3390/EN15051823.
[43] R. Daxini, K. S. Anderson, J. S. Stein, and M. Theristis, “Photovoltaic Module Spectral Mismatch Losses Due to Cell-Level EQE Variation; Photovoltaic Module Spectral Mismatch Losses Due to Cell-Level EQE Variation,” *IEEE J. Photovolt.*, vol. 15, no. 3, 2025, doi: 10.1109/JPHOTOV.2025.3545820.
[44] A. H. T. Le *et al.*, “Temperature-dependent performance of silicon solar cells with polysilicon passivating contacts,” *Sol. Energy Mater. Sol. Cells*, vol. 225, p. 111020, Jun. 2021, doi: 10.1016/J.SOLMAT.2021.111020.
[45] D. Afonso, O. Mesbahi, A. Bouich, and M. Tlemçani, “Influence of Long-Term and Short-Term Solar Radiation and Temperature Exposure on the Material Properties and Performance of Photovoltaic Panels: A Comprehensive Review,” *Energies*, vol. 18, no. 19, pp. 1–33, 2025.
[46] “Optical losses in silicon heterojunction solar cells: analysis of record-efficiency devices and practical limits based on ray-tracing simulations - EES Solar (RSC Publishing) DOI:10.1039/D5EL00001G.” [Online]. Available: https://pubs.rsc.org/en/content/articlehtml/2025/el/d5el00001g?utm_source=chatgpt.com
[47] V. Fiandra, L. Sannino, C. Andreozzi, G. Flaminio, A. Romano, and G. Rametta, “New high UV transparency PV encapsulants: Properties and degradation after accelerated UV aging tests,” *Polym. Degrad. Stab.*, vol. 234, p. 111257, Apr. 2025, doi: 10.1016/J.POLYMDEGRADSTAB.2025.111257.
[48] N. Pinochet, R. Couderc, and S. Therias, “Solar cell UV-induced degradation or module discolouration: Between the devil and the deep yellow sea,” *Prog. Photovolt. Res. Appl.*, vol. 31, no. 11, pp. 1091–1100, Nov. 2023, doi: 10.1002/PIP.3725;ISSUE:ISSUE:DOI.

[49] D. Chojniak *et al.*, “Measuring the External Quantum Efficiency of Tandem Photovoltaic Modules Using an LED-Based Solar Simulator,” *Sol. RRL*, vol. 9, no. 1, p. 2400517, Jan. 2025, doi: 10.1002/SOLR.202400517;SUBPAGE:STRING:FULL.
[50] T. Ju and Z. Li, “An Updated Review for Performance Enhancement of Solar Cells by Spectral Modification,” *Energ. 2024 Vol 17 Page 4492*, vol. 17, no. 17, p. 4492, Sep. 2024, doi: 10.3390/EN17174492.
[51] Y. Cao, D. Wu, P. Zhu, D. Shan, X. Zeng, and J. Xu, “Down-Shifting and Anti-Reflection Effect of CsPbBr3 Quantum Dots/Multicrystalline Silicon Hybrid Structures for Enhanced Photovoltaic Properties,” *Nanomater. 2020 Vol 10 Page 775*, vol. 10, no. 4, p. 775, Apr. 2020, doi: 10.3390/nano10040775.
[52] A. Mayavan, “Comprehensive Review on Downconversion/Downshifting Silicate-Based Phosphors for Solar Cell Applications,” *ACS Omega*, 2024, doi: 10.1021/ACSOMEGA.3C08806.
[53] T. A. Cohen, T. J. Milstein, D. M. Kroupa, J. D. Mackenzie, C. K. Luscombe, and D. R. Gamelin, “Quantum-cutting Yb3+-doped perovskite nanocrystals for monolithic bilayer luminescent solar concentrators,” *J. Mater. Chem. A*, vol. 7, no. 15, pp. 9279–9288, Apr. 2019, doi: 10.1039/C9TA01261C.
[54] S. Chatterjee, S. Biswas, S. Sourav, J. Rath, S. Akhil, and N. Mishra, “Strategies To Achieve Long-Term Stability in Lead Halide Perovskite Nanocrystals and Its Optoelectronic Applications,” *J. Phys. Chem. Lett.*, vol. 15, no. 40, pp. 10118–10137, Oct. 2024, doi: 10.1021/ACS.JPCLETT.4C02240.
[55] C. K. Trinh and Z. Ahmad, “SiO2-coated lead halide perovskites core–shell and their applications: a mini-review,” *R. Soc. Open Sci.*, vol. 11, no. 1, p. 230892, Jan. 2024, doi: 10.1098/RSOS.230892.
[56] E. Kymakis, D. A. Chalkias, Q. Masaadeh, E. Kaplani, and Y. Chao, “Luminescent Downshifting Silicon Quantum Dots for Performance Enhancement of Polycrystalline Silicon Solar Cells,” *Electron. 2022 Vol 11 Page 2433*, vol. 11, no. 15, p. 2433, Aug. 2022, doi: 10.3390/ELECTRONICS11152433.
[57] T. Lv, Y. Tang, H. Fan, S. Liu, S. Zeng, and W. Liu, “Carbon quantum dots anchored on the anti-reflection silica layer as solid luminescence down-shifting materials in solar panel encapsulation,” *Sol. Energy Mater. Sol. Cells*, vol. 235, p. 111450, Jan. 2022, doi: 10.1016/J.SOLMAT.2021.111450.
[58] J. Song *et al.*, “Performance Enhancement of Crystal Silicon Solar Cell by a CsPbBr3–Cs4PbBr6 Perovskite Quantum Dot @ZnO/Ethylene Vinyl Acetate Copolymer Downshifting Composite Film,” *Sol. RRL*, vol. 6, no. 11, p. 2200336, Nov. 2022, doi: 10.1002/solr.202200336.
[59] L. Pei, X. K. Gong, L. Li, Z. H. Ma, Z. J. Chen, and X. S. Zhang, “3D surface microstructure of silicon modified by QDs to improve solar cell performance through down-conversion and anti-reflection mechanism,” *Colloids Surf. Physicochem. Eng. Asp.*, vol. 675, p. 132015, Oct. 2023, doi: 10.1016/J.COLSURFA.2023.132015.
[60] “Degradation and Failure Modes in New Photovol-taic Cell and Module Technologies 2025 PVPS Task 13 Reliability and Performance of Photovoltaic Systems”, [Online]. Available: www.iea-pvps.org
[61] J. Kong *et al.*, “Carbon Quantum Dots: Properties, Preparation, and Applications,” *Molecules*, vol. 29, no. 9, p. 2002, May 2024, doi: 10.3390/MOLECULES29092002.
[62] T. Mandal, S. R. Mishra, M. Kumar, and V. Singh, “Emergence of carbon dots as luminescent solar concentrators for building integrated photovoltaics,” *Sustain. Energy Fuels*, vol. 8, no. 24, pp. 5638–5671, Dec. 2024, doi: 10.1039/D4SE00806E.
[63] C. S. Erickson, M. J. Crane, T. J. Milstein, and D. R. Gamelin, “Photoluminescence Saturation in Quantum-Cutting Yb3+-Doped CsPb(Cl1–xBrx)3 Perovskite Nanocrystals: Implications for Solar Downconversion,” *J. Phys. Chem. C*, vol. 123, no. 19, pp. 12474–12484, May 2019, doi: 10.1021/ACS.JPCC.9B01296.

[64] D. Gao *et al.*, “Near infrared emissions from both high efficient quantum cutting (173%) and nearly-pure-color upconversion in NaY(WO4)2:Er3+/Yb3+ with thermal management capability for silicon-based solar cells,” *Light Sci. Appl.*, vol. 13, no. 1, p. 17, Jan. 2024, doi: 10.1038/s41377-023-01365-2.
[65] L. Hu *et al.*, “Flexible and efficient perovskite quantum dot solar cells via hybrid interfacial architecture,” *Nat. Commun. 2021 121*, vol. 12, no. 1, pp. 466-, Jan. 2021, doi: 10.1038/s41467-020-20749-1.
[66] S. Song, W. Wang, and B. Cao, “Single silica-coated CsPbBr3 perovskite quantum dots with enhanced stability and excellent optical properties,” *Opt. Mater.*, vol. 133, p. 113070, Nov. 2022, doi: 10.1016/J.OPTMAT.2022.113070.
[67] P. Ahirwar and R. Kumar, “Synthesis and investigation of CsPbBr3 perovskite quantum dot thin-film on FTO substrate,” *Chem. Phys. Lett.*, vol. 810, p. 140180, Jan. 2023, doi: 10.1016/J.CPLETT.2022.140180.
[68] J. Zhang, D. Chen, K. Xu, J. Hu, S. Liang, and H. Zhu, “Ultra-stable CsPbBr3 nanocrystals encapsulated in mesoporous silica KIT-6 for LED applications,” *J. Lumin.*, vol. 260, p. 119856, Aug. 2023, doi: 10.1016/J.JLUMIN.2023.119856.
[69] S. Guo *et al.*, “Eco-Friendly Strategy To Improve Durability and Stability of Zwitterionic Capping Ligand Colloidal CsPbBr3 Nanocrystals,” *Langmuir*, vol. 36, no. 24, pp. 6775–6781, Jun. 2020, doi: 10.1021/ACS.LANGMUIR.0C00883.
[70] X. Liu *et al.*, “Ligand-modulated electron transfer rates from CsPbBr3 nanocrystals to titanium dioxide,” *Nanophotonics*, vol. 10, no. 8, pp. 1967–1975, Jun. 2021, doi: 10.1515/NANOPH-2020-0631/XML.
[71] H. Liang *et al.*, “Suppressing thermal degradation of CsPbBr3 quantum dot/EVA films via APTES-mediated interface engineering: toward efficient and stable luminescence down-shifting for silicon solar cells,” *Mater. Horiz.*, vol. 12, no. 22, pp. 9630–9642, Nov. 2025, doi: 10.1039/d5mh00578g.
[72] W. Liu *et al.*, “Luminescence, stability, and applications of CsPbBr3 quantum dot/polymethyl methacrylate composites prepared by a solvent- and ligand-free ball milling method,” *Opt. Mater.*, vol. 136, p. 113398, Feb. 2023, doi: 10.1016/J.OPTMAT.2022.113398.
[73] Q. Zeng *et al.*, “A hierarchical shell locks and stabilizes perovskite nanocrystals with near-unity quantum yield,” *Science*, vol. 391, no. 6782, Jan. 2026, doi: 10.1126/SCIENCE.ADY1370;WEBSITE:WEBSITE:AAAS-SITE;JOURNAL:JOURNAL:SCIENCE;WGROUP:STRING:PUBLICATION.
[74] Y. J. Lu *et al.*, “Dynamically controlled Purcell enhancement of visible spontaneous emission in a gated plasmonic heterostructure,” *Nat. Commun. 2017 81*, vol. 8, no. 1, pp. 1631-, Nov. 2017, doi: 10.1038/s41467-017-01870-0.
[75] J. L. Montaño-Priede, M. Zapata-Herrera, R. Esteban, N. Zabala, and J. Aizpurua, “An overview on plasmon-enhanced photoluminescence via metallic nanoantennas,” *Nanophotonics*, vol. 13, no. 26, pp. 4771–4794, Dec. 2024, doi: 10.1515/NANOPH-2024-0463/XML.
[76] G. M. Akselrod *et al.*, “Probing the mechanisms of large Purcell enhancement in plasmonic nanoantennas,” 2014, doi: 10.1038/NPHOTON.2014.228.
[77] Y. Jeong, Y. M. Kook, K. Lee, and W. G. Koh, “Metal enhanced fluorescence (MEF) for biosensors: General approaches and a review of recent developments,” *Biosens. Bioelectron.*, vol. 111, pp. 102–116, Jul. 2018, doi: 10.1016/J.BIOS.2018.04.007.
[78] T. S. Ogundeji *et al.*, “Recent advances in plasmonic quantum dot solar cells: Engineering strategies, charge dynamics, and future prospects,” *Nano Trends*, vol. 13, p. 100185, Mar. 2026, doi: 10.1016/j.nwnano.2026.100185.
[79] K.-Y. Lai and B.-H. Lim, “Comparative Study for Time-specific Ross Coefficient and Overall Ross Coefficient for Estimation of Photovoltaic Module Temperature,” in *2019 IEEE Conference on Sustainable Utilization and Development in Engineering and Technologies (CSUDET)*, Nov. 2019, pp. 251–256. doi: 10.1109/CSUDET47057.2019.9214602.

[80] O. Dupré, “Physics of the thermal behavior of photovoltaic devices”.
[81] M. Nicola and M. Berwind, “Improving Module Temperature Prediction Models for Floating Photovoltaic Systems: Analytical Insights from Operational Data,” *Energies*, vol. 17, no. 17, p. 4289, Jan. 2024, doi: 10.3390/en17174289.
[82] J. Kratochvil, W. Boyson, and D. King, “Photovoltaic array performance model.,” SAND2004-3535, 919131, Aug. 2004. doi: 10.2172/919131.
[83] M. K. Fuentes, “A simplified thermal model for Flat-Plate photovoltaic arrays,” Sandia National Labs., Albuquerque, NM (USA), SAND-85-0330, May 1987. Accessed: Apr. 19, 2026. [Online]. Available: https://www.osti.gov/biblio/6802914
[84] M. Theristis *et al.*, “Blind photovoltaic modeling intercomparison: A multidimensional data analysis and lessons learned,” *Prog. Photovolt. Res. Appl.*, vol. 31, no. 11, pp. 1144–1157, Nov. 2023, doi: 10.1002/pip.3729.
[85] A. Driesse, M. Theristis, and J. Stein, “PV module operating conditions and temperature measurements: an open dataset for PV research,” SAND--2023-01949, 2293574, Apr. 2023. doi: 10.2172/2293574.
[86] “Development of a Predictive Model for a Photovoltaic Module’s Surface Temperature.” Accessed: Apr. 19, 2026. [Online]. Available: https://www.mdpi.com/1996-1073/13/15/4005
[87] R. C. Staudemeyer and E. R. Morris, “Understanding LSTM -- a tutorial into Long Short-Term Memory Recurrent Neural Networks,” Sep. 12, 2019, *arXiv*: arXiv:1909.09586. doi: 10.48550/arXiv.1909.09586.
[88] M. Ezzini, M. Ennejjar, A. El Gourari, R. Mouachi, M. Raoufi, and M. Boukendil, “Comparative analysis of photovoltaic system technologies using advanced Machine Learning algorithms,” *Phys. Scr.*, vol. 101, no. 12, p. 126003, Mar. 2026, doi: 10.1088/1402-4896/ae5359.
[89] M. Mehdi, N. Hmidi, and A. Alami Merrouni, “Machine learning-based approach for predicting the PV modules temperature: A multi-technological assessment including soiling impact, toward a better solar plants’ operation under desert conditions,” *Case Stud. Therm. Eng.*, vol. 78, p. 107640, Feb. 2026, doi: 10.1016/j.csite.2026.107640.
[90] Y. Gal and Z. Ghahramani, “Dropout as a Bayesian Approximation: Representing Model Uncertainty in Deep Learning”.
[91] S. M. Lundberg and S.-I. Lee, “A Unified Approach to Interpreting Model Predictions,” in *Advances in Neural Information Processing Systems*, Curran Associates, Inc., 2017. Accessed: Apr. 19, 2026. [Online]. Available: https://proceedings.neurips.cc/paper_files/paper/2017/hash/8a20a8621978632d76c43dfd28b67767-Abstract.html
[92] D. E. Jung, C. Lee, K. H. Kim, and S. L. Do, “Development of a Predictive Model for a Photovoltaic Module’s Surface Temperature,” *Energies*, vol. 13, no. 15, p. 4005, Jan. 2020, doi: 10.3390/en13154005.
[93] P. Li *et al.*, “Advancing photovoltaic panel temperature forecasting: A comparative study of numerical simulation and machine learning in two types of PV power plant,” *Renew. Energy*, vol. 237, p. 121602, Dec. 2024, doi: 10.1016/j.renene.2024.121602.
[94] B. Ren, Q. Wang, N. Zhou, and S. Mekhilef, “Development and validation of interpretable machine learning models for photovoltaic panel temperature prediction,” *Expert Syst. Appl.*, vol. 296, p. 128952, Jan. 2026, doi: 10.1016/j.eswa.2025.128952.
[95] A. Keddouda *et al.*, “Photovoltaic module temperature prediction using various machine learning algorithms: Performance evaluation,” *Appl. Energy*, vol. 363, p. 123064, Jun. 2024, doi: 10.1016/j.apenergy.2024.123064.
[96] M. A. Cardoso *et al.*, “Solar spectral conversion based on plastic films of lanthanide-doped ionosilicas for photovoltaics: Down-shifting layers and luminescent solar concentrators,” *J. Rare Earths*, vol. 38, no. 5, pp. 531–538, May 2020, doi: 10.1016/j.jre.2020.01.007.

[97] M. Ali, S. Ali, H. ur Rashid, and Y. Iqbal, “Improvement in solar cells efficiency with luminescent downshifting nanocomposite lamination: A green alternative for ethylene–vinyl acetate,” *Sol. Energy*, vol. 282, p. 112986, Nov. 2024, doi: 10.1016/j.solener.2024.112986.
[98] W.-J. ; Ho, J.-J. ; Liu, B.-X. Ke, W.-J. Ho, J.-J. Liu, and B.-X. Ke, “Characterization of Luminescent Down-Shifting Spectral Conversion Effects on Silicon Solar Cells with Various Combinations of Eu-Doped Phosphors,” *Mater. 2022 Vol 15 Page 452*, vol. 15, no. 2, p. 452, Jan. 2022, doi: 10.3390/ma15020452.
[99] N. Varnakavi *et al.*, “Defect Passivation via Dual-Ligand Surface Modification for Bright and Stable Blue Emission in CsPbBr3 Nanoplatelets,” *Adv. Opt. Mater.*, vol. 13, no. 27, p. e01375, Sep. 2025, doi: 10.1002/adom.202501375.
[100] T. Liu *et al.*, “Drop-casting CsPbBr3perovskite quantum dots as down-shifting layer enhancing the ultraviolet response of silicon avalanche photodiode,” *Appl. Phys. Lett.*, vol. 119, no. 15, Oct. 2021, doi: 10.1063/5.0067710.
[101] X. Gu *et al.*, “Enhanced stability of perovskite CsPbBr3 QDs via Synergetic encapsulation with ZnO nanocrystals and commercial polymer,” *J. Lumin.*, vol. 275, p. 120780, Nov. 2024, doi: 10.1016/j.jlumin.2024.120780.
[102] Y. Wu *et al.*, “Dual-functional interface engineering of CsPbBr3 quantum dots for photon downshifting composite films in crystalline silicon solar cells,” *J. Mater. Sci. 2025 6045*, vol. 60, no. 45, pp. 22850–22864, Nov. 2025, doi: 10.1007/s10853-025-11781-x.
[103] Y. Bai, M. Hao, S. Ding, P. Chen, and L. Wang, “Surface Chemistry Engineering of Perovskite Quantum Dots: Strategies, Applications, and Perspectives,” *Adv. Mater.*, vol. 34, no. 4, p. 2105958, Jan. 2022, doi: 10.1002/adma.202105958.
[104] J. Chen *et al.*, “Organosilicon-Based Ligand Design for High-Performance Perovskite Nanocrystal Films for Color Conversion and X-ray Imaging,” *ACS Nano*, vol. 18, no. 14, pp. 10054–10062, Apr. 2024, doi: 10.1021/acsnano.3c11991.
[105] A. Jana *et al.*, “Stabilization of halide perovskites with silicon compounds for optoelectronic, catalytic, and bioimaging applications,” *InfoMat*, vol. 6, no. 12, p. e12559, Dec. 2024, doi: 10.1002/inf2.12559.
[106] P. Cao, B. Yang, F. Zheng, L. Wang, and J. Zou, “High stability of silica-wrapped CsPbBr3 perovskite quantum dots for light emitting application,” *Ceram. Int.*, vol. 46, no. 3, pp. 3882–3888, Feb. 2020, doi: 10.1016/j.ceramint.2019.10.114.
[107] F. Ma *et al.*, “Mesoporous silica-encapsulated CsPbBr3 quantum dots for the preparation of green fiber by electrospinning,” *Opt. Mater.*, vol. 160, p. 116744, Mar. 2025, doi: 10.1016/j.optmat.2025.116744.
[108] S. M. H. Qaid, H. M. Ghaithan, K. K. Alharbi, B. A. Al-Asbahi, and A. S. Aldwayyan, “Enhancement of Light Amplification of CsPbBr3 Perovskite Quantum Dot Films via Surface Encapsulation by PMMA Polymer,” *Polym. 2021 Vol 13 Page 2574*, vol. 13, no. 15, p. 2574, Aug. 2021, doi: 10.3390/polym13152574.
[109] Y. Xu, C. Yan, H. Liang, S. Huang, P. Feng, and J. Song, “Large-scale preparation of CsPbBr3 perovskite quantum dot/EVA composite adhesive film by melting for crystal silicon solar cell,” *Nanotechnology*, vol. 35, no. 17, p. 175404, Feb. 2024, doi: 10.1088/1361-6528/ad2157.
[110] C. Kim *et al.*, “Quantum Dot-Siloxane Anchoring on Colloidal Quantum Dot Film for Flexible Photovoltaic Cell,” *Small*, vol. 19, no. 41, p. 2302195, Oct. 2023, doi: 10.1002/smll.202302195.
[111] Y. Cao *et al.*, “Nonradiative Energy Transfer Enables a hv < Eg Response of Perovskite Quantum Dots in Si-Based Inorganic–Organic Hybrid Solar Cells,” *J. Phys. Chem. Lett.*, vol. 15, no. 31, p. 7870, Aug. 2024, doi: 10.1021/acs.jpclett.4c01773.
[112] R. Liu, R. Yu, and Z. Tan, “Photostability of Perovskite Solar Cells: Challenges and Strategies,” *Nanomater. 2025 Vol 15 Page 786*, vol. 15, no. 11, p. 786, May 2025, doi: 10.3390/nano15110786.

[113] S. Qu, J. Wu, J. Xu, P. Wang, and J. Song, “Carrier selection in downshifting perovskite quantum dot films for crystalline silicon solar cells,” *Opt. Mater.*, vol. 164, p. 117100, Jul. 2025, doi: 10.1016/j.optmat.2025.117100.
[114] C. H. Kang *et al.*, “High-speed colour-converting photodetector with all-inorganic CsPbBr3 perovskite nanocrystals for ultraviolet light communication,” *Light Sci. Appl. 2019 81*, vol. 8, no. 1, pp. 94-, Oct. 2019, doi: 10.1038/s41377-019-0204-4.
[115] S. A. Novikova *et al.*, “A surface modification strategy for synthesizing highly water-stable CsPbBr 3 perovskite quantum dots,” *Nanosyst. Phys. Chem. Math.*, vol. 16, no. 4, pp. 521–527, Sep. 2025, doi: 10.17586/2220-8054-2025-16-4-521-527.
[116] W. Lv *et al.*, “Improving the Stability of Metal Halide Perovskite Quantum Dots by Encapsulation,” *Adv. Mater.*, vol. 31, no. 28, p. 1900682, Jul. 2019, doi: 10.1002/adma.201900682.
[117] Q. Mo *et al.*, “Room temperature synthesis of stable silica-coated $CsPbBr_3$ quantum dots for amplified spontaneous emission,” *Photonics Res.*, vol. 8, no. 10, pp. 1605–1612, Oct. 2020, doi: 10.1364/PRJ.399845.
[118] J. Maes *et al.*, “Light Absorption Coefficient of CsPbBr3 Perovskite Nanocrystals,” *J. Phys. Chem. Lett.*, vol. 9, no. 11, pp. 3093–3097, Jun. 2018, doi: 10.1021/acs.jpclett.8b01065.
[119] H. Liang *et al.*, “Suppressing thermal degradation of CsPbBr3 quantum dot/EVA films via APTES-mediated interface engineering: toward efficient and stable luminescence down-shifting for silicon solar cells,” *Mater. Horiz.*, vol. 12, no. 22, pp. 9630–9642, Nov. 2025, doi: 10.1039/D5MH00578G.
[120] Y. Wang, P. Gawryszewska-Wilczynsk, X. Zhang, J. Yin, Y. Wen, and H. Li, “Photovoltaic efficiency enhancement of polycrystalline silicon solar cells by a highly stable luminescent film,” *Sci. China Mater. 2020 634*, vol. 63, no. 4, pp. 544–551, Jan. 2020, doi: 10.1007/s40843-019-1246-5.
[121] P. Kumar, S. Dua, R. Kaur, M. Kumar, and G. Bhatt, “A review on advancements in carbon quantum dots and their application in photovoltaics,” *RSC Adv.*, vol. 12, no. 8, pp. 4714–4759, Feb. 2022, doi: 10.1039/d1ra08452f.
[122] C. Bi, S. Wang, Q. Li, S. V. Kershaw, J. Tian, and A. L. Rogach, “Thermally Stable Copper(II)-Doped Cesium Lead Halide Perovskite Quantum Dots with Strong Blue Emission,” *J. Phys. Chem. Lett.*, vol. 10, no. 5, pp. 943–952, Mar. 2019, doi: 10.1021/acs.jpclett.9b00290.
[123] H. Ahmed, J. Doran, and S. J. McCormack, “Increased short-circuit current density and external quantum efficiency of silicon and dye sensitised solar cells through plasmonic luminescent down-shifting layers,” *Sol. Energy*, vol. 126, pp. 146–155, Mar. 2016, doi: 10.1016/j.solener.2016.01.003.
[124] J. R. Montes-Bojorquez, M. F. Villa-Bracamonte, O. J. Castillo, and A. A. Ayon, “Silicon solar cell efficiency improvement employing electrostatically assembled polyelectrolyte–quantum dot multilayers,” *Results Opt.*, vol. 15, p. 100655, May 2024, doi: 10.1016/j.rio.2024.100655.
[125] M. Chen, L. Lu, H. Yu, C. Li, and N. Zhao, “Integration of Colloidal Quantum Dots with Photonic Structures for Optoelectronic and Optical Devices,” *Adv. Sci.*, vol. 8, no. 18, p. 2101560, 2021, doi: 10.1002/advs.202101560.
[126] F. Werschler *et al.*, “Efficient Emission Enhancement of Single CdSe/CdS/PMMA Quantum Dots through Controlled Near-Field Coupling to Plasmonic Bullseye Resonators,” *Nano Lett.*, vol. 18, no. 9, pp. 5396–5400, Sep. 2018, doi: 10.1021/acs.nanolett.8b01533.
[127] W.-F. Fu *et al.*, “Optical and electrical effects of plasmonic nanoparticles in high-efficiency hybrid solar cells,” *Phys. Chem. Chem. Phys.*, vol. 15, no. 40, pp. 17105–17111, Sep. 2013, doi: 10.1039/C3CP52723A.
[128] I. Kim, J.-S. Moon, K. Kyhm, and J.-W. Oh, “Surface plasmon-assisted photoluminescence enhancement of Au-hybrid CdSe/ZnS nanocrystal quantum dots,” *Mol. Cryst. Liq. Cryst.*, vol. 654, no. 1, pp. 1–5, Sep. 2017, doi: 10.1080/15421406.2017.1348202.

[129] W.-F. Fu *et al.*, "Optical and electrical effects of plasmonic nanoparticles in high-efficiency hybrid solar cells," *Phys. Chem. Chem. Phys.*, vol. 15, no. 40, pp. 17105–17111, Sep. 2013, doi: 10.1039/C3CP52723A.
[130] A. Subhan and A.-Hamid. I. Mourad, "Plasmonic metal nanostructures as performance enhancers in emerging solar cells: A review," *Mater.*, vol. 6, p. 100509, Jan. 2025, doi: 10.1016/j.nxmate.2025.100509.
[131] V. Kumar, N. Nisika, and M. Kumar, "Modified Absorption and Emission Properties Leading to Intriguing Applications in Plasmonic–Excitonic Nanostructures," *Adv. Opt. Mater.*, vol. 9, no. 2, p. 2001150, 2021, doi: 10.1002/adom.202001150.
[132] A. J. Meixner *et al.*, "Coupling single quantum dots to plasmonic nanocones: optical properties," *Faraday Discuss.*, vol. 184, no. 0, pp. 321–337, Dec. 2015, doi: 10.1039/C5FD00074B.
[133] O. Chen *et al.*, "Compact high-quality CdSe–CdS core–shell nanocrystals with narrow emission linewidths and suppressed blinking," *Nat. Mater.*, vol. 12, no. 5, pp. 445–451, May 2013, doi: 10.1038/nmat3539.
[134] M. M. Abdullah and O. A. Ibrahim, "CdSe/CdS Quantum Dot Core-Shell for Silicon Solar Cell Efficiency Enhancement," *Nano Hybrids Compos.*, vol. 29, pp. 8–14, 2020, doi: 10.4028/www.scientific.net/NHC.29.8.
[135] R. Lopez-Delgado *et al.*, "Enhanced conversion efficiency in Si solar cells employing photoluminescent down-shifting CdSe/CdS core/shell quantum dots," *Sci. Rep.*, vol. 7, no. 1, p. 14104, Oct. 2017, doi: 10.1038/s41598-017-14269-0.
[136] A. Samanta, Y. Zhou, S. Zou, H. Yan, and Y. Liu, "Fluorescence Quenching of Quantum Dots by Gold Nanoparticles: A Potential Long Range Spectroscopic Ruler," *Nano Lett.*, vol. 14, no. 9, pp. 5052–5057, Sep. 2014, doi: 10.1021/nl501709s.
[137] M. Song *et al.*, "Photoluminescence Plasmonic Enhancement of Single Quantum Dots Coupled to Gold Microplates," *J. Phys. Chem. C*, vol. 118, no. 16, pp. 8514–8520, Apr. 2014, doi: 10.1021/jp408305x.
[138] S. Liu, X. Li, Y. Hao, X. Li, and F. Liu, "Effect of magnetron sputtering process parameters on the conductivity of thin metal film," *AIP Adv.*, vol. 13, no. 9, Sep. 2023, doi: 10.1063/5.0170746.
[139] T. Okamoto *et al.*, "Distance-Dependent Energy Transfer under Modal Strong Coupling from CdSe/ZnS Quantum Dots to a Plasmonic Fabry–Pérot Cavity," *J. Phys. Chem. C*, vol. 128, no. 10, pp. 4208–4214, Mar. 2024, doi: 10.1021/acs.jpcc.3c08503.
[140] J. Depciuch, M. Stec, A. Maximienko, J. Baran, and M. Parlinska-Wojtan, "Size-dependent theoretical and experimental photothermal conversion efficiency of spherical gold nanoparticles," *Photodiagnosis Photodyn. Ther.*, vol. 39, p. 102979, Sep. 2022, doi: 10.1016/j.pdpdt.2022.102979.
[141] N. Bhardwaj, B. Satpati, and S. Mohapatra, "Plasmon-enhanced photoluminescence from SnO2 nanostructures decorated with Au nanoparticles," *Appl. Surf. Sci.*, vol. 504, p. 144381, Feb. 2020, doi: 10.1016/j.apsusc.2019.144381.
[142] S. Liu, X. Li, Y. Hao, X. Li, and F. Liu, "Effect of magnetron sputtering process parameters on the conductivity of thin metal film," *AIP Adv.*, vol. 13, no. 9, p. 095326, Sep. 2023, doi: 10.1063/5.0170746.
[143] D. Mukherjee *et al.*, "Optimized sensing on gold nanoparticles created by graded-layer magnetron sputtering and annealing," *Sens. Actuators B Chem.*, vol. 425, p. 136875, Feb. 2025, doi: 10.1016/j.snb.2024.136875.
[144] R. G. West and S. M. Sadeghi, "Enhancement of Energy Transfer between Quantum Dots: The Impact of Metallic Nanoparticle Sizes," *J. Phys. Chem. C*, vol. 116, no. 38, pp. 20496–20503, Sep. 2012, doi: 10.1021/jp305910j.
[145] W. W. Yu, L. Qu, W. Guo, and X. Peng, "Experimental Determination of the Extinction Coefficient of CdTe, CdSe, and CdS Nanocrystals," *Chem. Mater.*, vol. 15, no. 14, pp. 2854–2860, Jul. 2003, doi: 10.1021/cm034081k.

[146] N.-Y. Kim *et al.*, "Localized surface plasmon-enhanced green quantum dot light-emitting diodes using gold nanoparticles," *RSC Adv.*, vol. 5, no. 25, pp. 19624–19629, Feb. 2015, doi: 10.1039/C4RA15585H.
[147] I. A. Milekhin *et al.*, "Resonant plasmon enhancement of light emission from CdSe/CdS nanoplatelets on Au nanodisk arrays," *J. Chem. Phys.*, vol. 153, no. 16, p. 164708, Oct. 2020, doi: 10.1063/5.0025572.
[148] J.-Y. Li *et al.*, "Room-Temperature Strong Coupling Between a Single Quantum Dot and a Single Plasmonic Nanoparticle," *Nano Lett.*, vol. 22, no. 12, pp. 4686–4693, Jun. 2022, doi: 10.1021/acs.nanolett.2c00606.
[149] Z. Dikmen, "Gold-tipped CdSe/CdZnS colloidal quantum wells as non-quenching plasmonic particles for optical applications," *Opt. Mater.*, vol. 147, p. 114761, Jan. 2024, doi: 10.1016/j.optmat.2023.114761.
[150] Y. Xiong and X. Zhang, "InAs/InP quantum dots stacking: Impact of spacer layer on optical properties," *J. Appl. Phys.*, vol. 125, no. 9, p. 093103, Mar. 2019, doi: 10.1063/1.5082722.
[151] J. Pan *et al.*, "Surface plasmon-enhanced quantum dot light-emitting diodes by incorporating gold nanoparticles," *Opt. Express*, vol. 24, no. 2, pp. A33–A43, Jan. 2016, doi: 10.1364/OE.24.000A33.
[152] N. Hildebrandt, M. Lim, N. Kim, D. Y. Choi, and J.-M. Nam, "Plasmonic quenching and enhancement: metal–quantum dot nanohybrids for fluorescence biosensing," *Chem. Commun.*, vol. 59, no. 17, pp. 2352–2380, Feb. 2023, doi: 10.1039/D2CC06178C.
[153] F. Bayrak, "Prediction of photovoltaic panel cell temperatures: Application of empirical and machine learning models," *Energy*, vol. 323, p. 135764, May 2025, doi: 10.1016/j.energy.2025.135764.
[154] S. M. Rezaul Karim, D. Sarker, and Md. Monirul Kabir, "Analyzing the impact of temperature on PV module surface during electricity generation using machine learning models," *Clean. Energy Syst.*, vol. 9, p. 100135, Dec. 2024, doi: 10.1016/j.cles.2024.100135.
[155] M. Abdelsattar, A. AbdelMoety, and A. Emad-Eldeen, "Comparative analysis of machine learning techniques for temperature and humidity prediction in photovoltaic environments," *Sci. Rep.*, vol. 15, no. 1, p. 15650, May 2025, doi: 10.1038/s41598-025-98607-7.
[156] J. Depoortere, J. Driesen, J. Suykens, and H. S. Kazmi, "SolNet: Open-source deep learning models for photovoltaic power forecasting across the globe," *Int. J. Forecast.*, vol. 41, no. 3, pp. 1223–1236, Jul. 2025, doi: 10.1016/j.ijforecast.2024.12.003.
[157] J. Gao, Q. Cao, Y. Chen, and D. Zhang, "Cross-variable Linear Integrated ENhanced Transformer for Photovoltaic power forecasting," Jun. 06, 2024, *arXiv*: arXiv:2406.03808. doi: 10.48550/arXiv.2406.03808.
[158] S. A. Hamad, M. A. Ghalib, A. Munshi, M. Alotaibi, and M. A. Ebied, "Evaluating machine learning models comprehensively for predicting maximum power from photovoltaic systems," *Sci. Rep.*, vol. 15, no. 1, p. 10750, Mar. 2025, doi: 10.1038/s41598-025-91044-6.
[159] C. Serpell, I. A. Araya, C. Valle, and H. Allende, "Addressing model uncertainty in probabilistic forecasting using Monte Carlo dropout," *Intell. Data Anal.*, vol. 24, no. 1_suppl, pp. 185–205, Jan. 2020, doi: 10.3233/IDA-200015.
[160] D. Wang, Z. Liang, Z. Zhang, and M. Li, "Efficient Estimation of the Convective Cooling Rate of Photovoltaic Arrays with Various Geometric Configurations: a Physics-Informed Machine Learning Approach," Mar. 25, 2024, *arXiv*: arXiv:2403.06418. doi: 10.48550/arXiv.2403.06418.
[161] D. Kurz and R. Nawrowski, "Thermal Time Constant of PV Roof Tiles Working under Different Conditions," *Appl. Sci.*, vol. 9, no. 8, p. 1626, Jan. 2019, doi: 10.3390/app9081626.
[162] T. Villemin, R. Claverie, J.-P. Sawicki, and G. Parent, "Thermal characterization of a photovoltaic panel under controlled conditions," *Renew. Energy*, vol. 198, pp. 28–40, Oct. 2022, doi: 10.1016/j.renene.2022.08.036.